University of Tennessee, Knoxville
TRACE: Tennessee Research and Creative Exchange

Doctoral Dissertations | Graduate School

5-2016

Magnetic, Optical and Electrical Properties of Electron-Hole Pairs in Polymer and Organo-Metal Halide Perovskite Photovoltaic cells

Yu-Che Hsiao
University of Tennessee - Knoxville, yhsiao2@vols.utk.edu

Follow this and additional works at: https://trace.tennessee.edu/utk_graddiss

 Part of the Polymer and Organic Materials Commons, and the Semiconductor and Optical Materials Commons

Recommended Citation

Hsiao, Yu-Che, "Magnetic, Optical and Electrical Properties of Electron-Hole Pairs in Polymer and Organo-Metal Halide Perovskite Photovoltaic cells. " PhD diss., University of Tennessee, 2016.
https://trace.tennessee.edu/utk_graddiss/3706

This Dissertation is brought to you for free and open access by the Graduate School at TRACE: Tennessee Research and Creative Exchange. It has been accepted for inclusion in Doctoral Dissertations by an authorized administrator of TRACE: Tennessee Research and Creative Exchange. For more information, please contact trace@utk.edu.

To the Graduate Council:

I am submitting herewith a dissertation written by Yu-Che Hsiao entitled "Magnetic, Optical and Electrical Properties of Electron-Hole Pairs in Polymer and Organo-Metal Halide Perovskite Photovoltaic cells." I have examined the final electronic copy of this dissertation for form and content and recommend that it be accepted in partial fulfillment of the requirements for the degree of Doctor of Philosophy, with a major in Materials Science and Engineering.

Bin Hu, Major Professor

We have read this dissertation and recommend its acceptance:

Roberto S. Benson, David Mandrus, Brian Long

Accepted for the Council:

Carolyn R. Hodges

Vice Provost and Dean of the Graduate School

(Original signatures are on file with official student records.)

Magnetic, Optical and Electrical Properties of Electron-Hole Pairs in Polymer and Organo-Metal Halide Perovskite Photovoltaic cells

A Dissertation Presented for the
Doctor of Philosophy
Degree
The University of Tennessee, Knoxville

Yu-Che Hsiao
May 2016

Copyright © 2016 by Yu-Che Hsiao
All rights reserved.

Dedication

I dedicate this dissertation to my parents.

Acknowledgements

I would like to express my sincere gratitude to my PhD dissertation advisor Dr. Bin Hu. I could not finish the dissertation without his dedication. In the past five years, I learned a lot from Dr. Bin Hu, like the capability to solve problems and spin physics theory. Most importantly, he had thought me what is a right attitude to do academic research. In addition to Dr. Bin Hu, I would like to thank my graduate committee members, Dr. Roberto S. Benson, Dr. David Mandrus, and Dr. Brian K. Long for their insightful and constructive comments on my dissertation.

I also would like to show my gratitude to my collaborators at Oak Ridge National Laboratory (ORNL) for their significant help in providing facilities and valuable discussion. They are Dr. Ilia Ivanov, Dr. Kai Xiao, and Dr. Yun Liu.

I owe sincere and earnest thankfulness to my former lab's members, Dr. Ming Shao, Dr. Liang Yan, Dr. Lei He, Dr. Dehua Hu, Dr. Hongfeng Wang, Dr. Huidong Zang, Dr. Wei Qin, and my current lab's members Dr. Shengbo Ma, Dr. Mahshid Ahmadi, Mingxing Li, Qing Liu, Hengxing Xu, Ting Wu, Jeremy Tisdale, and Miaosheng Wang. I would like to thank them for their numerous discussions and great support.

Last but not least, I would like to thank my parents Min-Da Hsiao and Shu-Cheng Tsai, and my young brother Yu-Chih Hsiao for their unconditional support and encouragement. I would also like to thank my intimate partner Pi-En Tsai, and my good friends Chien-Hung Chen, Cheng-En Yang, Shao-Yu Wang, Chih-Hsiang Kuo, and Hui-Chen Wang.

Abstract

Organic polymer and organo-metal halide perovskite (OMHP) materials have attracted extensive attention during the past decade due to their various applications, like solar cells, light emitting diode, even lasing action (OMHP). Especially, the organo-metal halide perovskite solar cell shows a remarkable power conversion efficiency of about 20%, which is comparable to the amorphous silicon solar cell. Therefore, OMHP solar cell had been considered as a promising substitution for the next generation of renewable energy source. The OMHP materials contain both advantages of organic and inorganic semiconductors, like solution processable thin film fabrication, long-range ambipolar transport characteristics, high dielectric constants, low exciton binding energies, and direct bandgap. In this dissertation, Chapter 1 has been separated into two parts. First part presents an introduction for different types of photovoltaic materials, including inorganic, organic, and OMHPs semiconductors. Second part introduces the device fabrication of organic solar cells, OMHP solar cells, and OMHP light emitting diodes. Chapter 2 shows the effect of dipole-dipole interaction between electron donor (PTB7) and electron acceptor (PCBM) in polymer based organic bulk heterojunction solar cell. Here, optically induced dipole-dipole interaction can largely decrease the electron-hole binding energy at donor:acceptor (D:A) based on the PTB7:PCBM bulk-heterojunctions. Chapter 3 demonstrates a systematically study of spin dependent photo-generated e-h pairs recombination and dissociation processes in OMHP solar cells by using external magnetic field combining with photocurrent (PC) and photoluminescence (PL). In Chapter 4, the effect of interfacial layer on photovoltaic performance in OMHP solar cells will be demonstrated. Meanwhile, impedance measurement and e-h binding energy measurement will be used to demonstrate how the interfacial dipole to affect the interfacial and bulk properties in OMHP solar cells. Chapter 5 presents the study of pure free charge recombination processes as a function of different densities of injection current by utilizing OMHP light emitting diodes. Chapter 6 study the current amplification and luminescence curve shape narrowing phenomenon from OMHP devices under a simultaneously applied electrical excitation and photoexcitation. Finally, Chapter 7 summarizes a conclusion for the entire dissertation.

Table of Contents

Chapter 1 Introduction 1

1.1 Different types of photovoltaic cells 1

1.1.1 Inorganic photovoltaics 1

1.1.2 Organic photovoltaics 1

1.1.3 Organo-metal halide perovskites photovoltaics 4

1.1.4 Working principle of organo-metal halide perovskite solar cells 8

1.2 Device fabrication of organo-metal halide perovskite photovoltaic and light emitting cells 9

1.2.1 Organo-metal halide perovskite photovoltaic cells 9

1.2.2 Organo-metal halide perovskite light emitting diode 11

1.2.3 Organic bulk-heterojunction solar cell 12

1.3 Magnetic Field Effect on Organic Semiconductors 13

1.3.1 Spin-orbit coupling 13

1.3.2 Hyperfine interaction 14

1.3.3 Spin exchange interaction 15

1.3.4 Zeeman effect 15

1.3.5 Magnetic field effect on intersystem crossing in organic semiconductors 16

Chapter 2 The Optically Induced Dipole-Dipole Interaction Effects on Charge Dissociation at Donor:Acceptor Interfaces in Organic Solar cells under Device-Operating Condition 18

2.1 Introduction 18

2.2 Experiment 20

2.4 The effects of intermolecular dipole-dipole interaction on e-h binding energy at D:A interfaces and photovoltaic responses in PTB7:PCBM organic solar cells. 26

2.5 Conclusion 34

Chapter 3 Magneto-Optical Studies on Electron-Hole Pairs Dissociation and Recombination in Perovskite Solar Cells 35

3.1 Introduction 35

3.2 Experiment 36

3.3 Spin dependent charge dissociation and recombination process under different photoexcitation intensities 37

3.4 The modulation of spin-exchange energy in electron-hole pairs under different photoexcitation intensities 42

3.5 Density dependent electron-hole binding energy in organo-metal halide perovskite solar cells. 42

3.6 Conclusion 47

Chapter 4 The Dipole Effect of Interfacial Layer on Photovoltaic Responses in Organo-Metal Halide Perovskite Photovoltaic Cells 50

4.1 Introduction 50

4.2 Experimental section 51

4.3 The comparison of intrinsic properties between PTB7 and P3HT 51

4.5 Conclusion 63

Chapter 5 Revealing Free Charge Recombination Mechanism in Organo-Metal Halide Perovskite 64

5.1 Introduction 64

5.2 Experimental section 65

5.3 High and low electroluminescence regimes from respective bimolecular recombination and mono-molecular recombination processes 66

5.4 Exploring spin mixing at low and high-efficiency EL regimes by using magneto-EL measurements. 69

5.5 Conclusion 75

Chapter 6 Spectral Narrowing Phenomenon in Perovskite Light Emitting Devices Induced by Linearly Polarized Photoexcitation 78

6.1 Introduction 78

6.2 Experimental Section 79

6.3 Results and discussion **81**

6.4 Conclusion **88**

Chapter 7 Conclusion **90**

List of Reference **92**

VITA……..……**103**

List of Figures

Figure 1-1. (a) Chemical structure of Polyacetylene showing alternative single and double bonds; (b) The schematic diagram of p_z orbitals showing the overlap of π electron wavefunction. 2
Figure 1-2. Ultra-fast charge transfer process in organic bulk-hetero junction active layer 4
Figure 1-3. Schematic crystal structure of organo-metal halide perovskites 5
Figure 1-4. General schematic diagram for perovskite solar cell operation [] 9
Figure 1-5. Working principle for the organo-metal halide perovskite and bulk heterojunction solar cells. 9
Figure 1-6. The picture of organo-metal halide perovskite thin film before (a) and after (b) thermal annealing. (c) Atomic force microscope (AFM) image for the morphology of organo-metal halide perovskite. 12
Figure 1-7. Schematic diagram for the magnetic field effect on resistance, photocurrent, photoluminescence and electroluminescence……17
Figure 2-1. (a) Magneto-photocurrent in ITO/PFN/PTB7:$PC_{60}BM$/MoO_3/Ag device by separately using by 532nm CW laser light (100mW/cm^2 and 24mW/cm^2) and simulated sun light (1 sun, 2 sun, and 3 sun). (b) The diagram to show intra-chain dipoles (blue arrow) in donor-PTB7 and optically induced polarization (red arrow) in acceptor-PCBM. (c) The diagram to show optically generated dipole-dipole interaction formed between donor and acceptor components to dissociate electron-hole pairs at D:A interfaces in PTB7:PCBM bulk-heterojunctions. Two arrows represent dipole and polarization in donor and acceptor with dipole-dipole interaction. 23
Figure 2-2. (a) Capacitance-frequency characteristics under various reverse biases at one sun condition for PTB7 single layer device. (b) Capacitance-frequency characteristics under various reverse biases at one sun condition for P3HT single layer device. (c) Capacitance-frequency characteristics under various simulated sunlight intensities at -0.9V reverse bias for PTB7 single layer device. (d) Capacitance-frequency characteristics under various simulated sunlight intensities at -0.9V reverse bias for P3HT single layer device. 25
Figure 2-3. Magneto-photocurrents measured by separately exciting donor-PTB7 and acceptor- $PC_{60}BM$. (a) Changing 325 nm intensity of exciting acceptor-$PC_{60}BM$ at constant 532 nm intensity (24mW/cm^2) of exciting donor-PTB7. (b) Changing 532 nm intensity of exciting donor-PTB7 at constant 325 nm intensity (14mW/cm^2) of exciting acceptor-$PC_{60}BM$. The critical bias (*Vc*) is given by the reverse bias required to completely quench magneto-photocurrent signal at each condition. 28
Figure 2-4. Magneto-photocurrents measured at different excitation intensities under simulated sunlight in ITO/PEDOT:PSS/P3HT:$PC_{60}BM$/Ca/Al device. The critical bias (*Vc*) is determined by the reverse bias required to completely quench magneto-photocurrent signal at each excitation intensity. 30
Figure 2-5. (a) The *I-V* characteristics measured by double-beam 325 nm (14mW/cm^2) and 532nm (24mW/cm^2) and simulated sunlight excitation for

ITO/PFN/PTB7:$PC_{60}BM$/MoO_3/Ag device. (b) Absorption spectra for donor-PTB7 and acceptor-$PC_{60}BM$. 33
Figure 3-1. Experimental setups for (a) magneto-photocurrent and (b) magneto-photoluminescence. 36
Figure 3-2. Magneto-photocurrents and current-voltage characteristics at different excitation intensities from 532nm CW laser in the ITO/PEDOT:PSS/$CH_3NH_3PbI_{3-x}Cl_x$/$PC_{71}BM$/TiOx/Al solar cell. (a) Positive magneto-photocurrent signals at room temperature. (b) Current-voltage characteristics. The dashed *I-V* curve is for 1 sun condition under AM1.5G solar simulated sun light. (c) Magneto-photocurrents for perovskite-only device (ITO/$CH_3NH_3PbI_{3-x}Cl_x$/Al) at different excitation intensities. (d) Short-circuit current (J_{sc}) as a function of excitation intensity (Squares: experimental data. Curve fitting by using geminate and non-geminate recombination). 38
Figure 3-3. Magneto-photoluminescence at room temperature in perovskite film. The photoexcitation source is from 532nm CW laser. (a) Negative magneto-photoluminescence signals at different excitation intensities. (b) The photoluminescence intensity as a function of excitation intensity. The inset shows photoluminescence spectra at different excitation intensities below and above the threshold intensity of 120mW/cm^2. 40
Figure 3-4. (a) Line-shape characteristics for positive magneto-photocurrent and negative magneto-photoluminescence. (b) Diagram to schematically show magnetic field-dependent antiparallel/parallel ratio in electron-hole pairs to generate positive magneto-photocurrent and negative magneto-photoluminescence in OMHPs. 41
Figure 3-5. (a) Normalized magneto-photocurrent characteristics at 140mW/cm^2 and 17mW/cm^2. (b) Normalized magneto-photoluminescence characteristics at 850mW/cm^2 and 170mW/cm^2. The photoexcitation source is 532nm CW laser 43
Figure 3-6. (a) Experimental setup for e-h binding energy measurement. (b) Typical curve evolution for binding energy measurement. 45
Figure 3-7. Magneto-photocurrent quenching caused by reverse bias at different excitation intensities to show dissociation effects at different charge densities in ITO/PEDOT:PSS/$CH_3NH_3PbI_{3-x}Cl_x$/$PC_{71}BM$/TiOx/Al device. The photoexcitation is from 532nm CW laser. (a) Critical bias=105mV at 140mW/cm^2. (b) Critical bias=65mV at 52mW/cm^2. (c) Critical bias=37mV at 17mW/cm^2. 46
Figure 3-8. Electric field-induced photoluminescence quenching at different excitation intensities (532nm laser). The excitation intensities of 17mW/cm^2, 52mW/cm^2, and 140mW/cm^2 require the critical biases of 1.2V, 3.3V, and 7.4V, respectively, to quench the photoluminescence by the same percent (80 %). 48
Figure 4-1. The molecular structure for (a) PTB7 and (b) P3HT. The red arrow in PTB7 is to indicate the photoexcited dipole direction. 4.4 Dipole effect of charge transport layer on interfacial and bulk properties in organo-metal halide perovskite solar cells 52
Figure 4-2. (a) *I-V* characteristics of mixed lead halide perovskite solar cell with respective PTB7 (red line) and P3HT (blue line) as hole transport layer under one sun illumination. (b) Energy level diagram and device structure of mixed halide perovskite solar cells. 54

Figure 4-3. Electric field induced Photoluminescence spectroscopy of (a) perovskite/PTB7 structur and (b) perovskite/P3HT structure under illumination of continuous laser beam at 632 nm with light intensity of 500 mW/cm^2 and electrical biases. The insets show the I-V curve of the related structure and indicates that applied electric filed are before the threshold point for current injection..... 55
Figure 4-4. (a) The picture for the LCR meter (Agilent E4980A) and (b) capacitance measurement setup..... 57
Figure 4-5. (a) and (b) Capacitance-frequency (*C-f*) measurement for P3HT and PTB7 single layer devices. (c) and (d) Capacitance-Voltage (*C-V*) measurement for double layers' devices of perovskite/P3HT and perovskite/PTB7, respectively..... 58
Figure 4-6. Magnetic field effect on photocurrent and electric field measurement under different photoexcitation intensities of 532nm laser beam based on mixed lead halide perovskite solar cells with respective PTB7 (red line) and P3HT (blue line) as the hole transport layer. (a) 100mW/cm^2, (b) 80mW/cm^2, (c) 30mW/cm^2, and (d) 2mW/cm^2. The insets are the normalized MFE- Photocurrent curves..... 62
Figure 5-1. Forward bias: Ag-positive and ITO-negative. Reverse bias: Ag-negative and ITO-positive. (a) Current-voltage-EL characteristics at both forward and reverse biases in Ag/MoO_3/$CH_3NH_3PbI_3$/TiO_x/ITO device. (b) Absorption, photoluminescence, and electroluminescence spectra for organo-metal halide halide perovskite thin film. (c) X-ray diffraction (XRD) spectra for organo-metal halide perovskite thin film. (d) Atomic force microscope (AFM) image to show the morphology for organo-metal halide halide perovskite thin film..... 67
Figure 5-2. (a) EL intensity is shown as a function of current density in Ag/MoO_3/$CH_3NH_3PbI_3$/TiO_x/ITO device at forward bias (Ag-positive and ITO-negative). (b) PL intensity is shown as a function of photoexcitation intensity in $CH_3NH_3PbI_3$ thin film under 532 nm CW laser illumination..... 68
Figure 5-3. (a) Magneto-EL measured at different injection currents from Ag/MoO_3/$CH_3NH_3PbI_3$/TiO_x/ITO device at forward bias (Ag-positive and ITO-negative). (b) Magneto-PL measured at different excitation intensities..... 72
Figure 5-4. Magneto-EL measured under high injection current (above 750 Ma/cm^2) from Ag/MoO_3/$CH_3NH_3PbI_3$/TiO_x/ITO device at forward bias (Ag-positive and ITO-negative)..... 73
Figure 5-5. The in-operative spin-mixing does not provide a mechanism to operate the parallel-to-antiparallel transition in short distance light emitting states formed through field-independent pairing process (a). The operative spin-mixing facilitates the parallel-to-antiparallel transition in electron-hole pairs formed through field-dependent pairing process and consequently increases light-emitting states: higher EL efficiency (b)..... 76
Figure 6-1. (a) Experimental setup and (b) device structure for the linear polarized light detection for bromine based light emitting diode..... 80
Figure 6-2. (a) Curve narrowing phenomenon from the bromine perovskite LED under dual excitations. (b) The relationship between FWHM and excitation intensity. (c) The detection of the linearly electrical polarization from emission light of bromine perovskite LEDs..... 82

Figure 6-3. (a) Current density-voltage (*J-V*) curves measured from respective simultaneously applied electrical excitation and photoexcitation, solely electrical excitation, and photocurrent. (b) Luminescence intensity as a function of excitation inteisity under different types of excitation source. 84
Figure 6-4. (a) Spectral comparison between photoluminescence, electroluminescence, and luminescence generated by simultaneously applied electrical excitation and photoexcitation. (b) *C-f* measurement under circularly polarized photoexcitation and linearly polarized photoexcitation..... 85
Figure 6-5. (a) Photoluminescence spectra narrowing phenomenon under different magnitudes of external electrical field without any injection current. (b) the detection of the linearly polarized photoluminescence under different magnitudes of external electrical field..... 89

Chapter 1 Introduction

1.1 Different types of photovoltaic cells

1.1.1 Inorganic photovoltaics

The first silicon solar cell with over 6% efficiency had been developed in 1954 from Bell Laboratory [1]. Recently, Gallium arsenide (GaAs) and Silicon (Si) based inorganic solar cells have shown decent efficiencies about respective 29.1% and 25.6% [2]. These efficiencies are close to the theoretical limitation of 30% in single junction cells [3]. Nowadays, inorganic solar cells have been commercial available and widely utilized around the world for the past two decades. At the end of 2014, the cumulative photovoltaic capacity reached about 178,000 megawatts (Mw), which shows almost a 265% growth as compared to the accumulative photovoltaic capacity till the end of 2011 (67,400 Mw). However, the number of the photovoltaic capacity is only to supply 1 percent (%) of global electricity demands. Therefore, to further increase the capacity of the solar photovoltaics, and meanwhile, reduce the cost are a very emergent mission to push the development of photovoltaic energy in the world.

1.1.2 Organic photovoltaics

As compared to inorganic semiconductors, in which the atoms or ions are covalent-bonded to for lattice structure, organic semiconductors are conjugated molecules [4]. In organic semiconductor, the π conjugation molecular orbitals are formed by the overlap of *Pz* orbitals of the carbon atoms in the molecules, which provides a pathway for the π electron to delocalize within the conjugated backbone, which is the origin of the electric conductivity in organic conductive polymers (as shown in Figure 1-1, here we use Polyacetylene as an example). On one hand, the bandgap of organic semiconductors is defined as the energy difference between the highest occupied molecular orbital (HOMO) and lowest unoccupied molecular orbital (LUMO). In general, the organic semiconductors with high energy level of HOMO are thought as p-type materials due to their relatively easily p-doped and hole transport characteristics. On the other hand, the organic

semiconductors with low energy level of LUMO can act as n-type materials due to the relatively easily n-doped and electron transport characteristics.

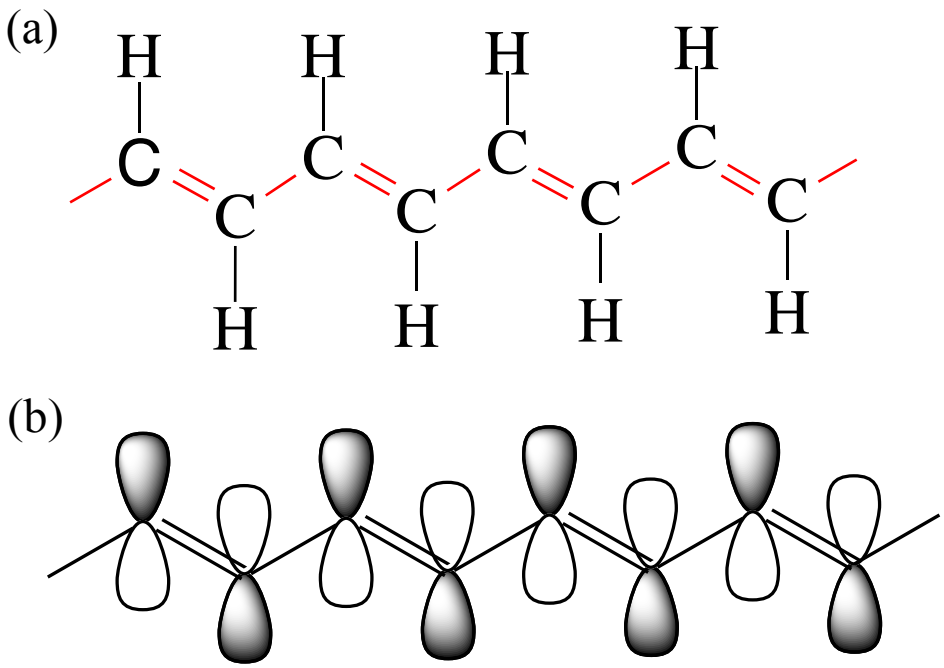

Figure 1-1. (a) Chemical structure of Polyacetylene showing alternative single and double bonds; (b) The schematic diagram of p_z orbitals showing the overlap of π electron wavefunction.

As mentioned above, due to the overlap of *Pz* orbitals within the organic semiconductors backbone that the organic semiconductors can demonstrate high intra-molecular electric conductivity. However, due to the weak inter-molecular interaction between two adjacent organic semiconductors (by Van der Waals force or hydrogen bond) that the mobility of inter-molecular charge transport across two neighbor organic molecules is more difficult than intra-molecular charge transport. As a result, the free charge carrier mobility in organic semiconductors ($\sim 10^{-3}$ $cm^2V^{-1}s^{-1}$) is much lower than inorganic semiconductors ($\sim 10^{3}$ $cm^2V^{-1}s^{-1}$). Nevertheless, the higher absorption coefficient in the

organic semiconductors than that of inorganic semiconductors makes organic semiconductors to absorb more photons to generate photocurrent.

For the past two decades, the power conversion efficiency of organic photovoltaic cells shows a significant improvement[2]. Up to now, the highest published power conversion efficiency (PCE) in organic solar cells is 11.5%. Even though the efficiency of organic photovoltaic is just about half of the inorganic photovoltaic, however, the organic photovoltaic show its own unique advantages, such as high flexibility, low cost, and easy process for large scale application, which are not exhibited in inorganic photovoltaic devices.

In addition to the low mobility in organic semiconductor, the higher binding energy (E_b) of photoexcited exciton is also a crucial parameter leading to a lower efficiency in organic solar cells than inorganic solar cells. Basically, the tight bond photoexcited exciton, namely Frenkel exciton, in organic solar cells is originated from the low dielectric constant of the organic semiconductors (ε_r, which is usually within the range of 2~4). Usually, the binding energy of Frenkel exciton is in the range of 0.3 eV to 1 eV, which is much higher than the loosely bond exciton, namely Wannier exciton ($E_b \approx 10$meV), in inorganic solar cells. As a result, the photo-generated exciton in organic solar cells is much harder to be dissociated than in inorganic solar cells. In order to effectively dissociate the photo-generated exciton in organic solar cells, the bulk heterojunction type organic active layer has been used in organic solar cells. The first bulk heterojunction type organic solar cell was developed in 1992 from A. J. Hegger's group [5,6]. They mixed one p-type organic electron donate material and one n-type electron accept fullerene derivative to form the bulk heterojunction donor:acceptor (D:A) interfaces in organic active layer. Moreover, they found the ultra fast electron transfer happens within the D:A interface, which is due to the sufficient energy band offset by mixing the electron donor and electron acceptor (as shown in Figure 1-2). This important breakthrough in organic solar cells had brought the development of organic photovoltaic into a new era.

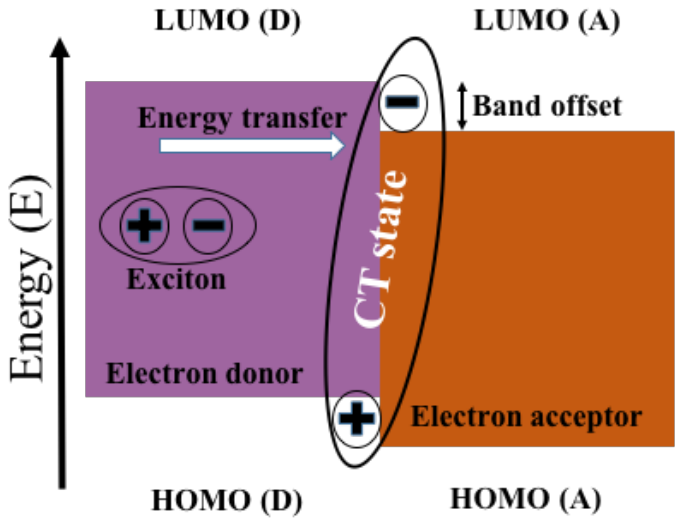

Figure 1-2. Ultra-fast charge transfer process in organic bulk-hetero junction active layer

1.1.3 Organo-metal halide perovskites photovoltaics

Beside pure inorganic and organic solar cell, an organic-inorganic hybrid photovoltaic material, namely organo-metal halide perovskite, has been a rising star in the field of renewable energy. In general, organo-metal halide perovskites can be described by a chemical formula of ABX_3 (as shown in Figure 1-3), where the A, B, and X sites are occupied by organic cation, metal cation and halide anion, respectively. We should note that organo-metal halide perovskites ($CH_3NH_3PbX_3$, X=Cl, Br or I) have shown great potential for PV application among other members in perovskites family [7-11]. In addition, the diverse choices of either organic cation or halide anion enable to develop a series of perovskites for enhancing PV actions [12-14], light emission [15-18], lasing actions [19-21], and Rashba effect [22]. However, with the concern of the toxicity of lead component, the lead-free perovskites have been developed, such as tin halide perovskites [23-28].

In 2009, the first perovskite solar cell with a PCE of 3.81% has been reported by Miyasaka *et al*. [29]. Two years later, Park *et al.* have further enhanced the PCE to 6.5% [30]. Till 2012, the high-efficiency perovskite solar cells have been demonstrated by Snaith

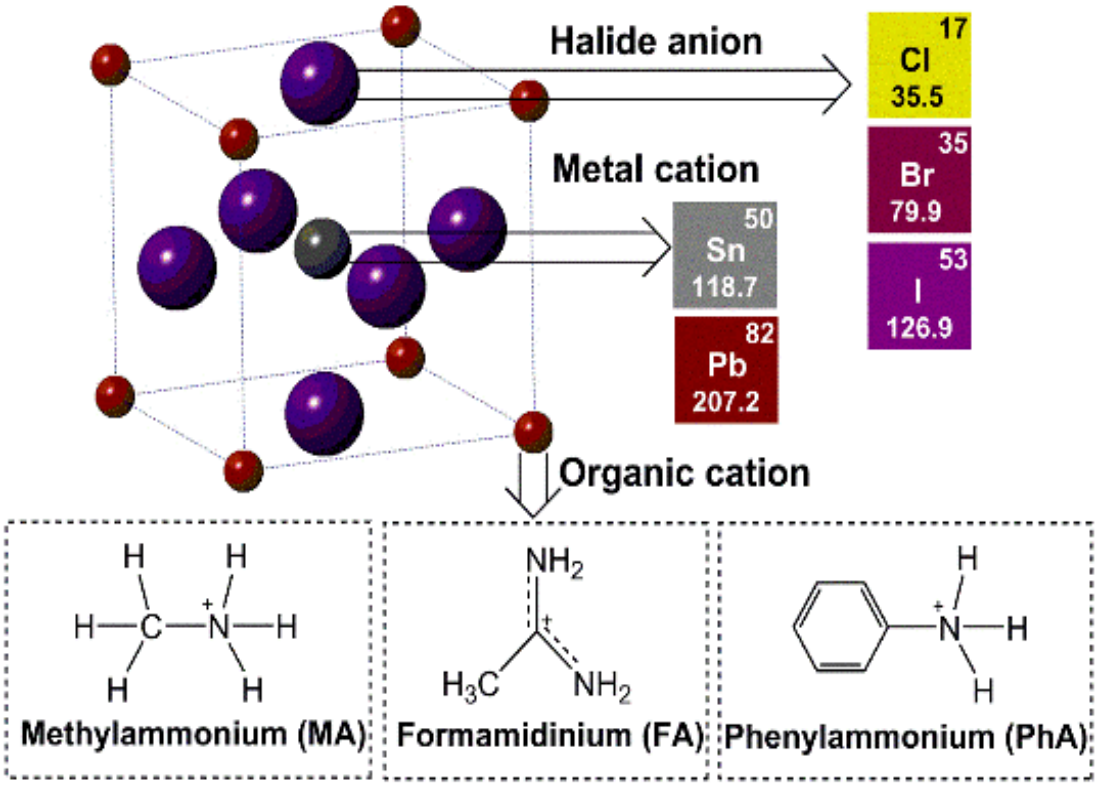

Figure 1-3. Schematic crystal structure of organo-metal halide perovskites

et al. with the PCE reaching 10.9% [31]. During the past three years, the PCEs of perovskite solar cells have shown an amazing growth from 10.9% to 20.1% [32]. In the application of photovoltaic field, the organo-metal halide perovskites have demonstrate remarkable long-range ambipolar charge transport characteristics [33], high dielectric constants [34,35], low exciton binding energies [36,37], intrinsic ferroelectric polarizations [38,39], and spin-dependent responses [40,41]. Clearly, these intrinsic photo-physics and spin-physics properties indicate that the perovskites are the most promising candidates for developing the next-generation PV cells.

First of all, long carrier diffusion lengths have been demonstrated by using temperature dependent photoluminescence in solution processed polycrystalline organo-metal halide perovskites, like $CH_3NH_3PbI_3$ (~ 100 nm) and $CH_3NH_3PbI_{3-x}Cl_x$ (~ 1 μm) [42,43]. These values are amazingly much higher than the diffusion lengths in polymer photovoltaic semiconductors (~ 10 nm) [43]. Normally, longer diffusion length means lower charge recombination and more efficient charge collection, and then, no doubt, leading to better photovoltaic actions. Meanwhile, the respective electron and hole mobility are similar with each other, so-called ambipolar charge transport. As a result, space charge limited current will be dismissed significantly due to the balanced charge transfer.

Secondly, Hu *et al*. [34] have observed a high dielectric constant (~32) in perovskites under dark condition. Furthermore, Juarez-Perez *et al*. [35] have shown that the dielectric constant can be largely enhanced (~1000) under photoexcitation. More recently, Lin *et al.* [44] have estimated that high dielectric constant can lead to an ultralow binding energy (<10 meV) in under light illumination in organo-metal halide perovskites. It's known that higher dielectric constant can lead to stronger dielectric screening effect, and hence leads to lower exciton binding energy. Clearly, the dielectric constant plays a crucial parameter in controlling the binding energy towards the generation of photocurrent in solar cells.

Thirdly, ferroelectric properties in organo-metal halide perovskites can be theoretically observed due to the distortion of crystal, especially the moving of center heavy metal, which is lead (Pb) in organo-metal halide perovskites, caused structural transition from orthorhombic phase to tetragonal phase [45]. Here, the intrinsic

ferroelectric polarizations provide additional mechanisms, like enhancing the charge transport and reducing charge recombination etc. [38,46], to control the key photovoltaic parameters, including photocurrent (J_{sc}), open circuit current (V_{oc}), and fill factor (*FF*) in perovskite solar cells.

In addition to the solar cells, organo-metal halide perovskites can also be introduced to make spintronics device and light emitting devices. Two decades ago, Hirasawa *et al.* [36] have reported the first magnetic field effects at low temperature (4.2 K) and high field (> 20 Tesla) in the $CH_3NH_3PbI_3$. However, at room temperature and low field it has been a challenge to develop magnetic field effects in perovskites. Recently, magnetic field effects have been shown at room temperature and low field (< 200 mT) in photoluminescence and photocurrent in perovskites, leading to magneto-photoluminescence and magneto-photocurrent [40,41]. Clearly, the results of magneto-photoluminescence and magneto-photocurrent provide us a good start to study the spin-physics in organo-metal halide perovskites.

On one hand, perovskites light emitting diode (LED) also attracts a lot of attention recently. First perovskites LED had been published by Tan *et al*. [15]. After that, several papers have reported the application of perovskites light emitting diode [15,18,17]. Especially, the emitting color of perovskites LED can be tuned from visible light to infrared light by changing the type or ratio of halide components (I^-, Cl^-, and Br^-). This result gives us a good opportunity to investigate the white light perovskites LED. Furthermore, the lasing action from OMHP thin film and single crystals has been significantly investigated. The color of OMHP laser can also be tuned by change the components within OMHP crystal structure. In addition to the LED application and lasing action, the property of two photons absorption has also demonstrated by G. Walters *et al*. [47]. They found that the absorption coefficient of the perovskite single crystal shows a non-linear response ($CH_3NH_3PbBr_3$) to be 8.6 cm/GW at 800 nm, which is comparable to epitaxial single crystal semiconductors with similar bandgap. Based on the fact that the OMHP is a good photovoltaic material for the solar cell application with an extremely low e-h pair binding energy. Therefore, the significant light emission property from OMHP is a surprising phenomenon because of that the low binding energy usually leads to a less recombination.

However, the OMHP can still shows high recombination rate from respective electrical excitation or photoexcitation, and consequence, lead to a strong light emission.

1.1.4 Working principle of organo-metal halide perovskite solar cells

The working principle of organo-metal halide perovskites solar cells is quite similar to organic solar cells (as shown in Figure 1-4, 1-5). First of all, the photon from light source has been absorbed by the OMHP material active layer, and, secondly, a photoexcited electro-hole (e-h) pair have been generated by exciting an electron to the LUMO of OMHP material and leave a hole in the HOMO. Thirdly, if the diffusion length of e-h pair is larger than the domain size of electron donor OMHP material that the e-h pair can diffuse to the D:A interface. Fourthly, the photoinduced electron transfer happens at D:A interface within the time scale of femtosecond due to the strong electron affinity of electron acceptor material. Finally, due to the built-in potential of the OMHP photovoltaic cells that the separated electron and hole can diffuse to respective cathode and anode, and then generate photocurrent. However, there are two major differences in the generation of photovoltaic response as compared to the organic solar cells. First, due to the extreme low electron-hole binding energy that the photo-generated electron-hole pairs can be dissociated spontaneously without bulk-heterojunction structure, and the charge dissociation can be happened in the time period of picoseconds [19]. Second, as mentioned in the previous section that the organo-metal halide perovskites can show ambipolar charge transfer characteristics, which means the electron and hole has similar charge mobility. Therefore, the “acceptor” layer of organo-metal halide perovskites solar cell can use either electron acceptor materials or hole acceptor materials, which is different as compared to organic solar cells (organic solar cells can only use electron acceptor materials to form bulk heterojunction structure, which is due to the unbalanced charge mobility between free electron and free hole in donor materials). Therefore, we do have a more flexible device making engineering of organo-metal halide perovskite solar cells than the polymer based organic solar cells, which can give us more room to further advance the device making engineering and leading to a higher device power conversion efficiency.

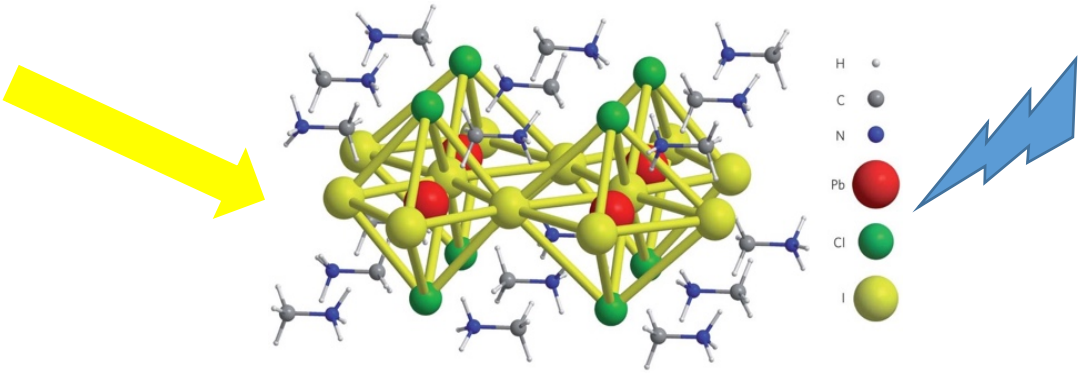

Figure 1-4. General schematic diagram for perovskite solar cell operation [48]

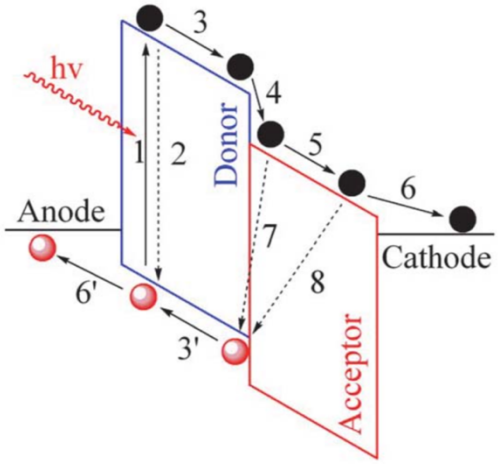

Figure 1-5. Working principle for the organo-metal halide perovskite and bulk heterojunction solar cells.

1.2 Device fabrication of organo-metal halide perovskite photovoltaic and light emitting cells

1.2.1 Organo-metal halide perovskite photovoltaic cells

In this part, two different types of OMHP photovoltaic cells will be introduced. First one is p-i-n type, the other one is n-i-p. In both device structures, the OMHP active layer is sandwiched between one n-type electron transfer layer and one p-type hole transfer layer. The difference of these two device structure is the order of layers stacking.

p-i-n type of OMHP photovoltaic cells: The OMHP precursor was prepared by mixing Methylammonium iodide (MAI) and lead chloride ($PbCl_2$) in anhydrous

dimethylformamide (DMF, Aldrich) with a mole ration of 1:1. The overall solution concentration was 40 wt%. The perovskite precursor was then stirred for 12 hours at 60℃ and followed by filtration with a 0.45μm PVDF filter. The OMHP ($CH_3NH_3PbI_{3-x}Cl_x$) solution was spin-cast with the film thickness of 300 nm on the ITO/PEDOT:PSS substrates, followed by thermal annealing at 90℃ for 2h. After the thermal annealing the color of the OMHP thin film will be transferred from green color to black color (as shown in Figure 1-6). The Phenyl-C_{71}-butyric acid methyl ester ($PC_{71}BM$) was spin-coated with the thickness of 100nm (from the 1,2-Dichlorobenzene solution with the concentration of 15mg/ml) as an electron transfer layer on the thermally annealed perovskite films. The TiOx was prepared by adding a 0.026M HCl (diluted in isopropanol alcohol) into a 0.46M titanium isopropoxide solution (diluted in isopropanol alcohol) with stirring for 12 hours and then filtered with a 0.2 μm PTFE filter. The TiOx thin films were spin-cast with the thickness of about 35 nm on the $PC_{71}BM$/perovskite/PEDOT:PSS/ITO substrates and then thermally heated at 130℃ for 10minutes. The aluminum (Al) electrodes were thermally deposited with film thicknesses of 150 nm under the vacuum of 7×10^{-7} torr. The perovskite solar cells were finally fabricated with the device structure of ITO/PEDOT:PSS/$CH_3NH_3PbI_{3-x}Cl_x$/$PC_{71}BM$/TiOx/Al.

n-i-p type of OMHP photovoltaic cells: The perovskite was prepared by mixing methylammonium iodide (MAI) and lead chloride ($PbCl_2$) in anhydrousdimethylformamide (DMF) (Aldrich) with a ratio of 3:1. The total solution concentration was 40 wt%. The precursor was then heated at 60°C for 12 hours while stirring and then was filtered by a 0.45 μm PVDF filter. The TiOx was prepared by adding a 0.026M HCl (diluted in isopropanol alcohol) into a 0.46M titanium isopropoxide solution (diluted in isopropanol alcohol) with stirring for 12 hours and then filtered with a 0.2 μm PTFE filter. The TiOx thin films were spin-cast with the thickness of about 45 nm on the $PC_{71}BM$/perovskite/PEDOT:PSS/ITO substrates and then thermally heated at 450℃ for 30 minutes. Then the as prepared mixture of MAI and $PbCl_2$ solution was spin-cast onto the TiO_X layer with the thickness of around 300 nm and annealed at 90 °C for 2 hours. Afterwards, hole transport materials (P3HT or PTB7) was dissolved in chlorobenzene (Aldrich) with a concentration of 2 wt%, and then deposited with the thickness of 60 nm

on top of the perovskite active layer. Finally, the gold (Au) electrode were thermally deposited with film thicknesses of 60 nm under the vacuum of 7×10^{-7} torr. The perovskite solar cells were finally fabricated with the device structure of ITO/TiO_x/$CH_3NH_3PbI_{3-x}Cl_x$/P3HT(PTB7)/Au.

1.2.2 Organo-metal halide perovskite light emitting diode

The TiO_x was prepared from the $Ti(OC_3H_7)_4$ precursor and used as an electron-injecting layer with the thickness of 35 nm on the pre-cleaned ITO substrates. The TiOx films on ITO substrates were then thermally annealed at 450℃ for 30 minute, and then gradually cooled down to room temperature. Here, we use two types pf OMHPs as our light wmitting layers, the first one is $CH_3NH_3PbI_3$, the second one is $CH_3NH_3PbBr_3$. The organo-metal halide perovskite precursors were prepared by mixing Methylammonium iodide (MAI) separately with lead iodide (PbI_2) or lead bromine ($PbBr_2$) in anhydrous dimethylformamide. Specifically, the precursor of organo-metal halide perovskites were prepared by mixing MAI and PbI_2 ($PbBr_2$) with the molar ratio of 1:1. The $CH_3NH_3PbI_3$ perovskite precursor was then stirred for 12 hours at 60℃ and followed by filtration (0.45μm PVDF filters). The $CH_3NH_3PbI_3$ perovskite thin film was fabricated by first spin coating organo-metal halide perovskite ($CH_3NH_3PbI_3$) film followed by thermal annealing of 90℃ for 120 mins. The overall thickness of the $CH_3NH_3PbI_3$ perovskite films are around 50 nm. The $CH_3NH_3PbBr_3$. perovskite precursor was then stirred for 30 minutes at 60℃ and followed by filtration (0.45μm PVDF filters). The $CH_3NH_3PbBr_3$ perovskite thin film was fabricated by first spin coating $CH_3NH_3PbBr_3$ solution followed by thermal annealing of 100 ℃ for 10 minutes. The overall thickness of the $CH_3NH_3PbBr_3$ perovskite films are around 50 nm. The MoO_3 was vacuum deposited with the thickness of 10 nm on top of the perovskite interfa ce to serve as a hole-injecting layer. The silver (Ag) electrodes were then vacuum deposited with the thickness of 100 nm on the hole-injecting MoO_3 layer. The vacuum depositions were done under the pressure of 7×10^{-7} torr. The perovskite light-emitting devices were finally fabricated with inverted architecture: Ag/MoO_3/$CH_3NH_3PbI_3$ ($CH_3NH_3PbBr_3$)/TiO_x/ITO (Forward: Ag-positive and ITO-negative. Reverse: ITO-positive and Ag-negative).

1.2.3 Organic bulk-heterojunction solar cell

The experimental studies were performed based on the typical solar cell: PTB7:PCBM bulk-heterojunctions. The photovoltaic materials (PTB7 and PCBM) together with electrolyte PFN were purchased from 1-material Chemscitech and used to fabricate the ITO/PFN/PTB7:PCBM/MoO_3/Ag devices. The PFN was spin-coated on pre-cleaned ITO glass substrates from a solution of 2mg/ml in methanol with a small volume of acetic acid (2μl/ml). The PTB7:PCBM composite was prepared with the weight ratio of 1:1.5 in chlorobenzene/1,8-diiodoctane mixture solvent (97ml:3ml). The concentration of PTB7:PCBM composite solution was set at 25mg/ml. The PTB7:PCBM films were spin cast with the thickness of 100nm on the charge-transporting PFN layers. The charge-transporting MoO_3 layers and Ag electrodes were thermally deposited under the vacuum of 7×10^{-7} torr with film thicknesses of 10nm and 40nm, respectively.

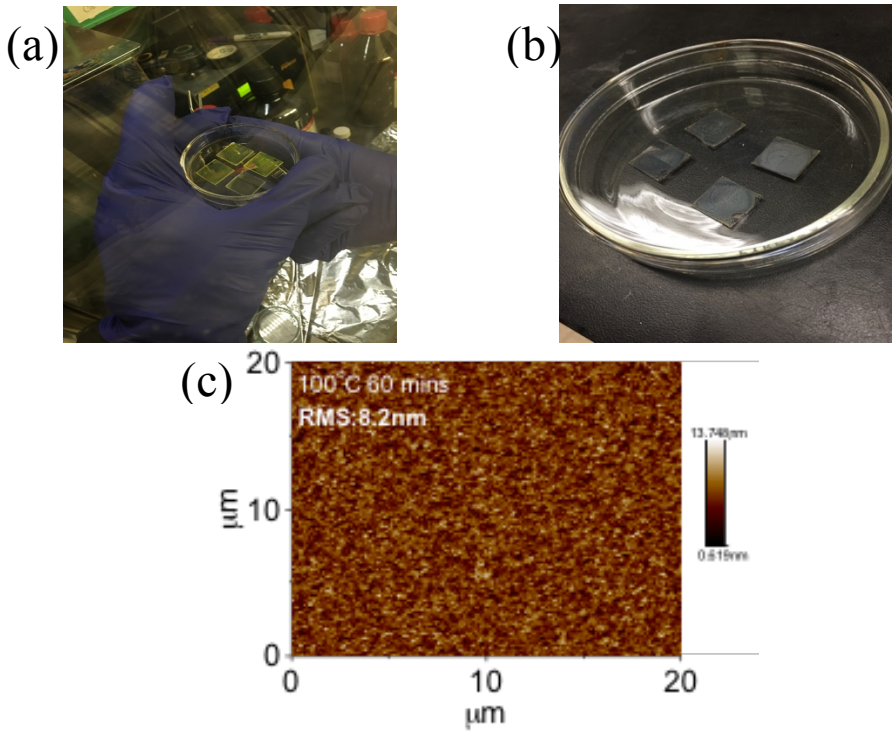

Figure 1-6. The picture of organo-metal halide perovskite thin film before (a) and after (b) thermal annealing. (c) Atomic force microscope (AFM) image for the morphology of organo-metal halide perovskite.

1.3 Magnetic Field Effect on Organic Semiconductors

The excited states in organic semiconductors could be separated into two different species, which are exciton (short separation distance between electron and hole) and polaron pairs (long separation distance between electron and hole). Here, the lifetime for both singlet exciton and triplet exciton are 10^{-9} seconds and 10^{-6} second, respectively [49,50]. On the other hand, the lifetimes for singlet polaron pair and triplet polaron pair are respective 10^{-10} second and 10^{-8}~10^{-9} second [51]. The spin exchange energy of excited pair state can be described by

$$J=J_0 \exp(-\beta(r_e-r_h)) \quad (1)$$

Here, β and J_0 are constant of exchange interaction and radius constant, which are directly related to the intrinsic property of materials. Here, we can see it clear that the spin exchange of excited pairs is related to the separation distance between electron and hole (r_e-r_h).

In π-conjugated polymer, the energy difference between singlet exciton and triplet exciton (ΔEst) is about 1 *eV* [52,53], which is related to the spin exchange interaction. However, the ΔEst in singlet polaron pair and triplet polaron pair is not just from spin exchange interaction, the hyperfine interaction is also getting involved [54]. In general, the energy of 1 Oersted of external magnetic field is about 10^{-8} *eV*, which implies that disturbing the intersystem crossing (ISC) of exciton is hard due to the large spin exchange energy of exciton state. Nevertheless, the ΔEst of polaron pair is twice larger than the spin exchange energy of polaron pair (*J*), in which *J* is directly related to the separation distance of electron-hole. Therefore, the external magnetic filed can then disturb the ISC of polaron pair due to the longer electron-hole separation distance than exciton. By using the Coulombic attraction to calculate the spin exchange energy that we can get a calculated spin exchange energy at the range between 10 *meV* to 100 *meV* [55]. Due to the lower spin exchange energy that the external magnetic field may can disturb the intersystem crossing rate of polaron pairs.

1.3.1 Spin-orbit coupling

From classical electro-magneto theory, the electron motions around nucleus. Here, the tangential velocity is *v,* and we can get a coulombic electric field between electron and proton, which can be described as

$$\vec{E} = \vec{\nabla}\phi(r) = \frac{1}{e}\vec{\nabla}\phi(r) = \frac{1}{e}\frac{\vec{r}}{r}\frac{dV}{dr} \quad (2)$$

Here, a magnetic field could be generating through the electrical field from the orbital motion of electron:

$$\vec{B} = -\frac{1}{c^2}\vec{v}\times\vec{E} \quad (3)$$

Therefore, the spin state of the electron could be affected by this magnetic field, namely spin-orbit coupling (SOC). Here, the Hamiltonian of the SOC could be described as:

$$\overrightarrow{\widehat{H_{so}}} = \frac{1}{2m_e^2c^2}\frac{1}{r}\frac{dV}{dr}\vec{S}\cdot\vec{L} \quad (4)$$

Here, the atom radius is $r = n^2a_0$, and the Coulombic potential is $V = -\frac{e^2}{4\pi\varepsilon_0 r}$. In which, the Bohr radius is $a_0 = \frac{4\pi\varepsilon_0\hbar^2}{m_e e^2}$, and therefore, we can then get the Spin-orbit Hamiltonian:

$$\overrightarrow{\widehat{H_{so}}} = \frac{1}{4\pi\varepsilon_0}\frac{e^2}{2m_e^2c^2}\left(\frac{1}{n^2\frac{4\pi\varepsilon_0\hbar^2}{m_e e^2}}\right)^3\vec{S}\cdot\vec{L} \quad (5)$$

Under excited states, we set the wave function of electron as $|\phi>$, and therefore, we can calculate the energy of SOC:

$$E_{so} = <\phi\left|\overrightarrow{\widehat{H_{so}}}\right|\phi> \sim a^4 m_e c^2 \sim 10^{-3}\ eV \quad (6)$$

in which, $\alpha = \frac{1}{4\pi\varepsilon_0}\frac{e^2}{\hbar c} \backsim \frac{1}{137}$ is constant of fine structure.

1.3.2 Hyperfine interaction

Hyperfine interaction is the interaction between the spin momentum ($\vec{\hat{S}}$) of electron and the orbital momentum ($\vec{I}$) of proton, which can contribute different magnetic field effect as compared to SOC. Here, we can describe the hyperfine interaction as

$$\overrightarrow{B_I} = \frac{\mu_0}{4\pi r^3}[3(\overrightarrow{\mu_I}\cdot\vec{r})\hat{r} - \overrightarrow{\mu_I}] + \frac{2\mu_0}{3}\overrightarrow{\mu_I}\delta^3(\vec{r}) \quad (7)$$

and the Hamiltonian of hyperfine interaction can be described as

$$\widehat{H_{hf}} = -\overrightarrow{\mu_s}\cdot\overrightarrow{B_I} = \frac{\mu_0 g_p e^2}{8\pi m_p m_e}\frac{\left[3\left(\overrightarrow{s_p}\cdot\vec{r}\right)(\overrightarrow{s_e}\cdot\vec{r}) - \overrightarrow{s_p}\cdot\overrightarrow{s_e}\right]}{r^3} + \frac{\mu_0 g_p e^2}{3m_p m_e}\overrightarrow{s_p}\cdot\overrightarrow{s_e}\delta^3(\vec{r}) \quad (8)$$

in which, the magnetic momentum of nucleus is ($\overrightarrow{\mu_I} = \frac{g_p e}{2m_p}\overrightarrow{S_p}$) and electron magnetic momentum is $\overrightarrow{\mu_e} = -\frac{e}{m_e}\overrightarrow{S_e}$. Through the calculation of first order perturbation energy that we can then estimate the energy of hyperfine interaction:

$$E_{so} = < \phi \left| \overrightarrow{\widehat{H_{hf}}} \right| \phi > \sim 10^{-7}\ eV \qquad (9)$$

1.3.3 Spin exchange interaction

Polaron pairs and excitons can demonstrate different spin exchange energies due to the different separation distance of electron-hole and the wavefunction overlap between electron-hole. Here the spin exchange interaction can be described as

$$\vec{J}(r_e, r_h) = \int \varphi_e(r_e)\varphi_h(r_h)\frac{e^2}{r_e - r_h}\varphi_e(r_e)\varphi_h(r_h)dr_e dr_h = J_0 \exp[-\alpha(r_e - r_h)] \qquad (10)$$

in which, $\varphi_e$and $\varphi_h$are the wavefunctions of respective electron and hole, $r_e$and $r_h$are the spatial position of respective electron and hole.

In general, electrons and holes are considered as Fermion, and their total wavefunction are anti-symmetry with each other. Therefore, through Pauli principle we can know that the overlap of spatial wavefunction of triplet state is lower than singlet, leading to a longer lifetime of triplet than the lifetime of singlet. Here, the energy of spin exchange interaction can be described as

$$\mathrm{E} = E_0 - J(\vec{r})\left(\frac{1}{2} + \frac{2}{\hbar^2}\overrightarrow{S_1}\cdot\overrightarrow{S_2}\right) = E_0 + \begin{cases} J(\vec{r})(Singlet, S=0) \\ -J(\vec{r})(Triplet, S=1) \end{cases} \qquad (11)$$

In organic semiconductors, the spin exchange energy of electron-hole can be presented as

$$H_{eh} = -\vec{J}(r_e r_h)\overrightarrow{S_e}\cdot\overrightarrow{S_h} \qquad (12)$$

1.3.4 Zeeman effect

When an atom is placed under external magnetic field that the energy of triplet state can be change, which is called Zeeman effect. The total Hamiltonian of a single atom in a magnetic field is

$$H = H_0 + H_e \qquad (13)$$

H_0 is the unperturbed Hamiltonian and H_z is the perturbed Hamiltonian due to the

external magnetic field B, and H_Z can be determined by

$$H_z = -\vec{\mu} \cdot \vec{B} \tag{14}$$

Here, $\vec{\mu}$ is the magnetic momentum:

$$\vec{\mu} = -\mu_B \cdot g \cdot \frac{\vec{M}}{\hbar} \tag{15}$$

where, $\vec{M}$ is total electronic angular momentum including orbital angular momentum $\vec{L}$ and spin angular momentum $\vec{S}$. g is the g factor. Therefore, the magnetic momentum could be re-described as

$$\vec{\mu} = -\mu_B \cdot g \cdot \frac{g_l \cdot \vec{L} + g_s \cdot \vec{S}}{\hbar} \tag{16}$$

Where, μ_B is Bohr magneton ($\mu_B = \frac{e\hbar}{2m_e}$), and $g_l = 1$ and $g_S \approx 2.0023192$, which is the anomalous gyromagnetic ratio. As a result, the perturbation from the external magnetic field can be shown as:

$$H_z = \frac{e}{2m}\left(\vec{L} + 2\vec{S}\right) \cdot B_{ext} \tag{17}$$

Here, the competition between the internal field and the external field determines whether the Zeeman splitting can happen.

1.3.5 Magnetic field effect on intersystem crossing in organic semiconductors

As we had mentioned in the past four sections that the intersystem crossing rate of polaron pairs in organic semiconductors can be manipulate by four different mechanisms, which are spin-orbit coupling, hyperfine interaction, spin exchange energy, and Zeeman effect. Here, the external magnetic field we applied can compete with the above four mechanisms, leading to change the singlet/triplet ratio (magnetic field response) in organic semiconductors (as shown in Figure 1-7). When the life time of polaron pair is shorter than the spin relaxation time, the only factor to manipulate the spin can only be the external magnetic field. Thus, the thermal energy (which may exceed the exchange energy by external magnetic field) cannot affect the spin motion processes [56].

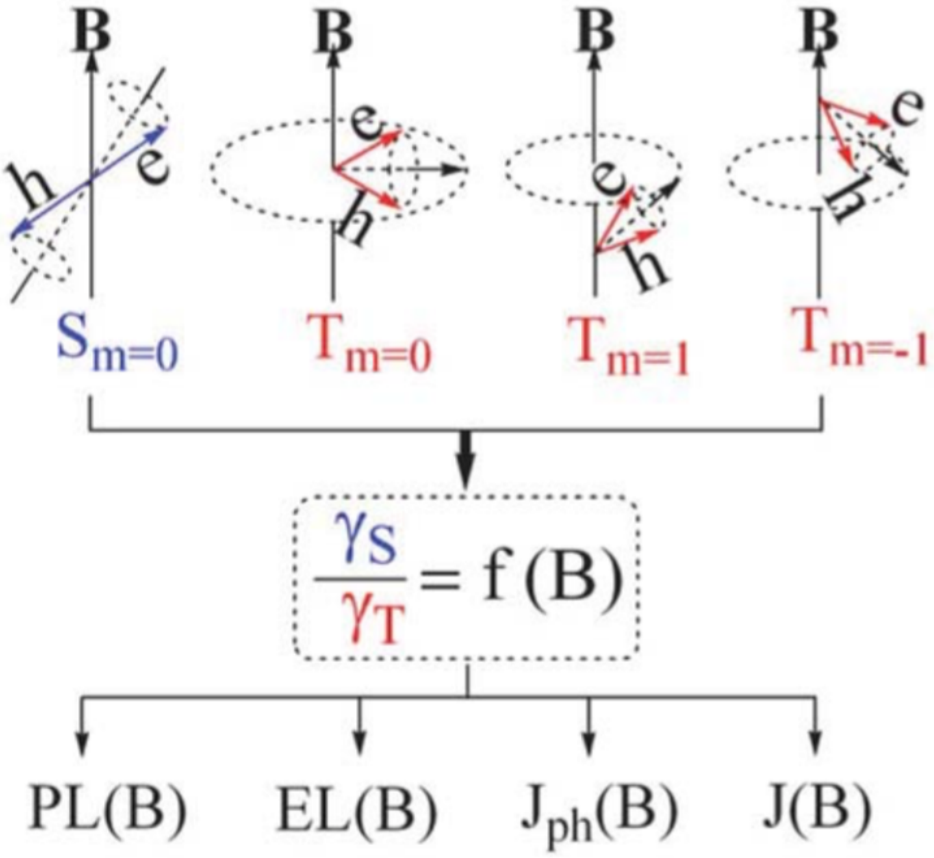

Figure 1-7. Schematic diagram for the magnetic field effect on resistance, photocurrent, photoluminescence and electroluminescence [57].

Chapter 2 The Optically Induced Dipole-Dipole Interaction Effects on Charge Dissociation at Donor:Acceptor Interfaces in Organic Solar cells under Device-Operating Condition

2.1 Introduction

Low bandgap polymers are critical components towards developing high-efficiency organic solar cells with facial materials processing and large-area properties [58-64]. Using coexisted electron-donating and electron-withdrawing units forms an important approach to design advanced photovoltaic polymers with low bandgaps for developing efficient solar cells [65-67]. The typical photovoltaic polymer, namely polythieno[3,4-b]-thiophene-co-benzodithiophene (PTB7), contains both the electron-donating Benzodith-iophene (BDT) and the electron-withdrawing thienothiophene (TT) moieties [60,68]. As a consequence, a photoexcitation can generate local electric dipoles between electron-donating and electron-withdrawing moieties, namely intra-chain dipoles, in the donor PTB7 chains [69-74]. The optically generated dipoles have been estimated by calculating the dipole-moment change from ground state to excited state [72-74]. It should be pointed out that the widely used acceptor molecules of fullerene derivatives possess very high polarizabilities in exposure to an electric field [75,76,77]. With the high polarizabilities a photoexcitation can largely polarize the fullerene molecules, leading to optically polarized acceptor molecules. In this situation the dipole-dipole interaction can be established between donor and acceptor components in bulk-heterojunction solar cells. In principle, the optically induced dipole-dipole interaction can influence the charge dissociation, transport, and collection through drifting field, and consequently changes the J_{sc}, V_{oc}, and FF in bulk-heterojunctions. In this chapter, we demonstrate optically induced dipole-dipole interaction effects on the e-h binding energy at D:A interfaces based on the typical PTB7:PCBM solar cells. Our experimental measurements combine two simultaneous procedures: (i) applying the double-beam 532 nm and 325 nm excitations to establish the dipole-dipole interaction between donor and acceptor components and (ii) using magneto-photocurrent to monitor

the charge dissociation at the D:A interfaces, in the PTB7:PCBM bulk-heterojunction solar cells. Specifically, adjusting the double-beam 532 nm and 325 nm excitations can generate three different excited situations: (i) the donor only, (ii) acceptor only, and (iii) both donor and acceptor components to control the dipole-dipole interaction. At the same time, we use magneto-photocurrent with an external electric field to measure the critical bias required to completely dissociate the electron-hole pairs at the D:A interfaces when the dipole-dipole interaction is established between donor and acceptor components. Therefore, combining double-beam excitation with magneto-photocurrent can reveal the dipole-dipole interaction effects on the electron-hole binding energy at the D:A interfaces in bulk-heterojunction solar cells.

The magneto-photocurrent phenomena were originally observed from the photoconduction in pristine organic materials in a low field (< 10 mT) in 1970s [78-80]. In recent a few years, the magneto-photocurrent studies have been extended to bulk-heterojunctions in organic solar cells [81-84]. In general, the magneto-photocurrent phenomena can be observed when a magnetic field disturbs the populations of different spin states during the generation of photocurrent. Before applying a magnetic field, different spin states can reach certain populations governed by the spin mixing, caused by hyperfine or spin-orbital coupling, and spin-conserving, generated by spin-exchange interaction. In most organic materials where hyperfine interaction is a primary factor responsible for spin mixing normally occurring below 10 mT due to negligible spin-orbital coupling, the spin-exchange interaction can essentially determine whether a magnetic field can disturb the populations of different spin states above the hyperfine regime by introducing in-phase or out-phase spin precessions [85]. In general, the different spin states can exist on both intramolecular and intermolecular states in organic solar cells. The intramolecular states are mainly Frenkel excitons while the intermolecular states present as polaron pairs and charge-transfer complexes. In general, the Frenkel excitons do not exhibit appreciable magneto-photocurrent due to strong spin-exchange interaction which tightly governs the spin populations [81,83]. However, the polaron pairs and charge-transfer states can generate appreciable magneto-photocurrent signals at room temperature [78,81,83]. The experimental studies have shown that a magnetic field can easily disturb

the spin-conserving or spin-mixing in polaron pairs and charge-transfer states due to weak spin-exchange interaction [81,83,84,86]. Specifically, in pristine organic materials the polaron pairs can generate a low-field magneto-photocurrent within hyperfine regime (< 10 mT) due to negligible spin-exchange interaction [83, 87]. However, in bulk-heterojunctions the low-field magneto-photocurrent from polaron pairs becomes un-detectable [81]. This indicates that the polaron pairs are completely dissociated by the D:A interfaces. Instead, a new magneto-photocurrent can be observed above the hyperfine regime (> 10 mT) due to appreciable spin-exchange interaction in organic solar cells [81]. These new magneto-photocurrent signals above hyperfine regime have been attributed to the electron-hole pairs at D:A interfaces. In this work, we select the PTB7 and $PC_{60}BM$ as donor and acceptor to fabricate the bulk-heterojunction PTB7:$PC_{60}BM$ solar cells. In particular, the separated absorption spectra between PTB7 and $PC_{60}BM$ allows that the donor and acceptor components can be separately excited by using double-beam 532 nm and 325 nm excitations in the PTB7:$PC_{60}BM$ solar cells. Based on the PTB7:$PC_{60}BM$ system with separated optical absorption spectra, combining the magneto-PC with an external bias provides an experimental method to explore the electron-hole binding energy at the D:A interfaces in the PTB7:$PC_{60}BM$ solar cells when the electrical interaction is optically changed by separately exciting the donor only, acceptor only, and both donor and acceptor components. Essentially, the electron-hole binding energy at the D:A interfaces can be evaluated by the critical bias required to completely quench the magneto-PC generated by electron-hole pairs in the PTB7:$PC_{60}BM$ solar cells.

2.2 Experiment

The device making procedure has been introduced in chapter 1. The effective device operating area is 6 mm^2 under simulated sunlight illumination and 3.14 mm^2 under CW laser light illumination. The current-voltage (*I-V*) characteristics were measured by using Keithley 2400 source meter under simulated sunlight (Thermal Oriel 96000 300 W from Newport) and continuous wave (CW) laser excitations (532nm and 325nm). The capacitance-frequency measurement were performed under different frequencies by using a dielectric spectrometer (Agilent E4980A LCR). The magneto-photocurrent signals were recorded by measuring the short-circuit current as a function of magnetic field. The control-

experiments indicate that the observed magneto-photocurrent is originated from the electron-hole pairs at the D:A interfaces in the PTB7:$PC_{60}BM$ solar cells by comparing pristine donor-PTB7 and the PTB7:$PC_{60}BM$ bulk-heterojunctions. The magneto-photocurrents were recorded by measuring the photocurrent (J_{sc}) as a function of magnetic field at room temperature. The magneto-photocurrent amplitude is defined as $\frac{I_B - I_0}{I_0}$, where the I_B and I_0 are the photocurrents with and without magnetic field at short-circuit condition. By combing the magneto-photocurrent measurements with a reversed external bias, the electron-hole binding energy at D:A interfaces was evaluated by the critical bias required to completely quench the magneto-photocurrent signal at different excitation intensities. The dipole-dipole interaction between donor and acceptor components were optically tuned by separately exciting (i) the donor-PTB7 only, (ii) the acceptor-$PC_{60}BM$ only, and (iii) both the donor-PTB7 and acceptor-$PC_{60}BM$, in the PTB7:$PC_{60}BM$ solar cells with using the double-beam excitation of 532 nm and 325 nm. All measurements were performed under nitrogen gas atmosphere at room temperature.

2.3 The observation of CT states formation and dissociation by magneto-photocurrent measurement

Figure 2-1 (a) shows the magneto-PC signals measured above the hyperfine regime from the ITO/PFN/PTB7:$PC_{60}BM$/MoO_3/Ag device under two different excitations by using (i) 532 nm beam of exciting the donor-PTB7 and (ii) simulated sunlight of exciting both donor and acceptor components. When the 532 nm beam of 100 mW/cm^2 is used to only excite the donor-PTB7, a magneto-PC signal can be clearly observed in the PTB7:$PC_{60}BM$ solar cell. The observed magneto-PC indicates that the electron-hole pairs are formed as charge-transfer states at the D:A interfaces during the generation of photocurrent. However, when the simulated sunlight at one-sun condition (100 mW/cm^2 white light) is used to excite both donor and acceptor, the magneto-PC becomes non-detectable in the PTB7:$PC_{60}BM$ solar cells. We note that the 532 nm laser beam of 100 mW/cm^2 is stronger than the simulated sun light at one-sun condition by a factor of 2.6. However, further increasing the simulated sun light to three-sun condition (300 mW/cm^2) does not generate any detectable magneto-PC signal. When the 532 nm laser beam intensity

decreases to 24 mW/cm^2 to only excite the donor-PTB7, slightly lower than sun light (one-sun condition), a magneto-PC signal can be still observed (Figure 2-1 (a)). Therefore, our experimental observation indicates that exciting both donor and acceptor by using simulated sunlight disables the formation of electron-hole pairs at D:A interfaces in the PTB7:$PC_{60}BM$ solar cells. This phenomenon opens an important question: how can the simulated sunlight completely dissociate the electron-hole pairs at the D:A interfaces? Here, we propose that the simulated sunlight generates an electrical interaction between donor and acceptor components by exciting both the donor-PTB7 and acceptor-$PC_{60}BM$, and consequently dissociates the electron-hole pairs at the D:A interfaces. Essentially, exciting both donor and acceptor generates an electrical dipole in the PTB7 through intramolecular charge transfer and the electrical polarization in the $PC_{60}BM$ through excited states, leading to a dipole-dipole interaction between the PTB7 and the $PC_{60}BM$ in the PTB7:$PC_{60}BM$ solar cells (Figure 2-1 (b)). Specifically, exciting the donor-PTB7 generates both excitons and electrical dipoles. Exciting the acceptor-$PC_{60}BM$ can lead to largely polarized acceptor molecules due to high polarizabilities. As a consequence, the dipoles in donor and the polarized acceptor can experience a dipole-dipole interaction between the PTB7 and $PC_{60}BM$ components. The photoluminescence quenching shows that the photoexcited excitons can predominately dissociate into free carriers in donor and acceptor components [88,89]. But, the free carriers can partially recombine into electron-hole pairs, namely charge-transfer states, at the D:A interfaces [90-92]. Obviously, the electron-hole pairs are exposed to the dipole-dipole interaction formed between the donor and acceptor components during the generation of photovoltaic actions (Figure 2-1 (c)). Here, we can see that the dipole-dipole interaction between donor and acceptor components provides a primary driving force to dissociate the electron-hole pairs at the D:A interfaces in bulk-heterojunction solar cells.

We should note that the optically generated dipoles in the donor-PTB7 are the necessary parameter in the dipole-dipole interaction between the PTB7 and $PC_{60}BM$ components. To confirm the optically generated dipoles in PTB7, we investigate the capacitance-frequency (*C-f*) characteristics upon simulated sunlight illumination. It is

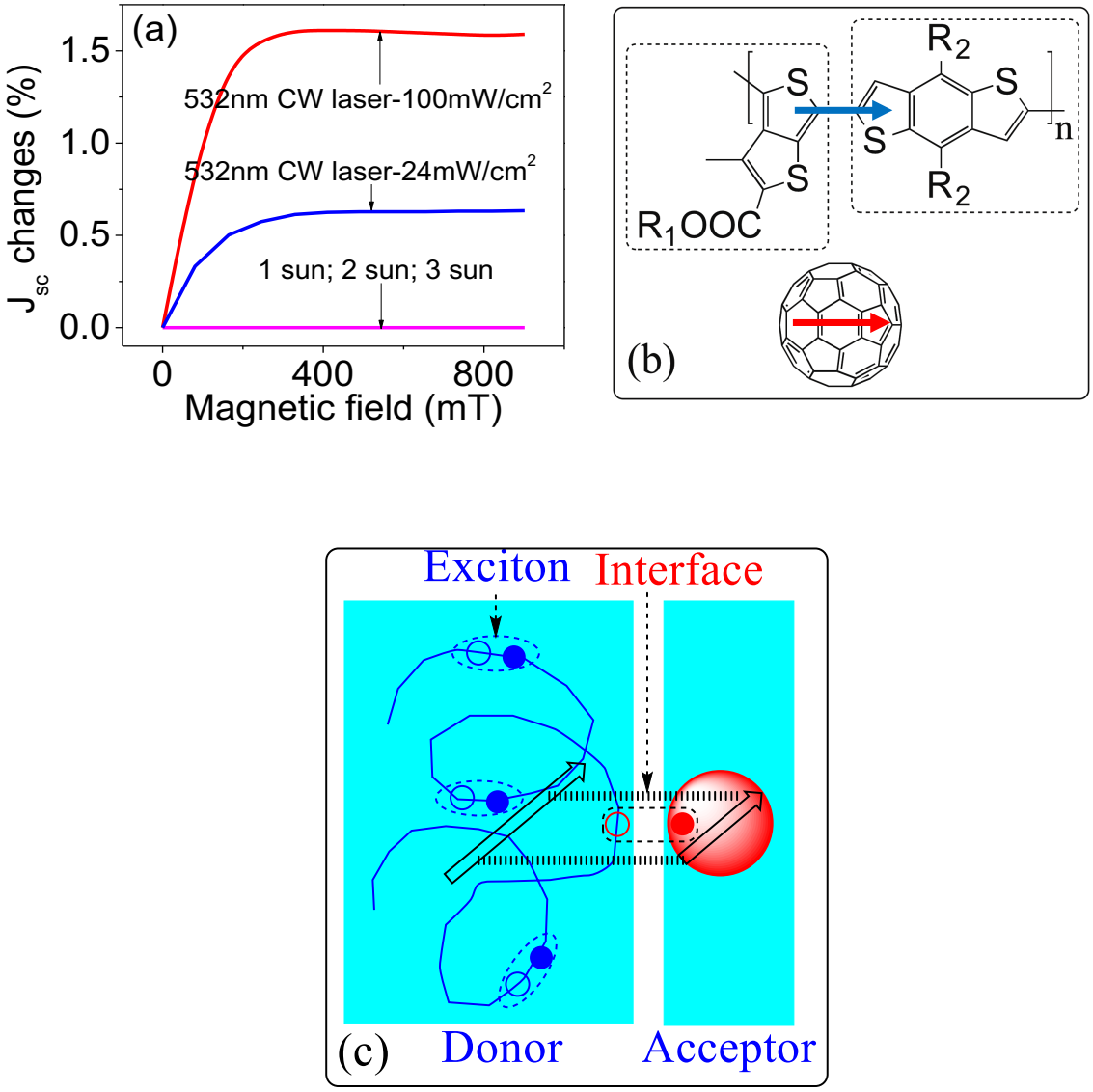

Figure 2-1. (a) Magneto-photocurrent in ITO/PFN/PTB7:$PC_{60}BM$/MoO_3/Ag device by separately using by 532nm CW laser light (100mW/cm^2 and 24mW/cm^2) and simulated sun light (1 sun, 2 sun, and 3 sun). (b) The diagram to show intra-chain dipoles (blue arrow) in donor-PTB7 and optically induced polarization (red arrow) in acceptor-PCBM. (c) The diagram to show optically generated dipole-dipole interaction formed between donor and acceptor components to dissociate electron-hole pairs at D:A interfaces in PTB7:PCBM bulk-heterojunctions. Two arrows represent dipole and polarization in donor and acceptor with dipole-dipole interaction.

known that the low and high-frequency *C-f* characteristics are generated by electrode interfaces and bulk in the electrode/semiconductor/electrode devices [93]. Essentially, the high-frequency *C-f* characteristics can reflect the bulk polarization upon applying light illumination. Figure 2-2 shows the high-frequency *C-f* characteristics based on single layer PTB7 and P3HT devices with the architecture of Ag/polymer/Ag. We can see that increasing simulated sun light intensity from 0.3 sun to 1 sun condition can cause a much larger change (19%) in the Ag/PTB7/Ag device as compared to a much smaller change (7.8%) in the Ag/P3HT/Ag device at high frequency regime (> $1.0x10^6$ *Hz*), as shown in Figure 2-2 (a) and (b). This indicates that the PTB7 exhibits stronger bulk polarization than the P3HT under optical excitation. The PTB7 chain possesses an intramolecular donor-acceptor structure between BDT and TT units, forming a mechanism to generate an electrical dipole upon optical excitation. However, the P3HT chain lacks the mechanism to generate an electrical dipole due to the absence of intramolecular donor-acceptor structure. Therefore, the observed stronger bulk polarization provides an evidence to confirm the formation of optically generated dipoles in the PTB7 upon light illumination. Now we consider whether optically generated dipoles can be partially aligned in the PTB7 by built-in field. We know that the PTB7 is formed amorphous structure in a spin-cast film. In principle, an amorphous structure can lead to random dipoles, causing negligible net dipole moment in the PTB7 film. In this situation the electrical interaction between the donor-PTB7 and the acceptor- $PC_{60}BM$ would be difficult to influence the charge dissociation at the D:A interfaces in the PTB7: $PC_{60}BM$ solar cells. However, the optically generated dipoles can be partially aligned through dipole migration within an amorphous PTB7 chain under the influence of built-in field in electrode/polymer/electrode devices. We can see in Figure 2-2 (c) and (d) that applying a reverse bias of -0.9 V can largely increase the high-frequency *C-f* signal by 11.9% in the Ag/PTB7/Ag device but only 3.3% in the Ag/P3HT/Ag device. This result shows that an external field can interact with the optically generated dipoles in the PTB7 and largely increases the bulk polarization. This provides an experimental information to support that optically generated dipoles can be partially aligned, leading to a net dipole moment in the amorphous PTB7 for generating an

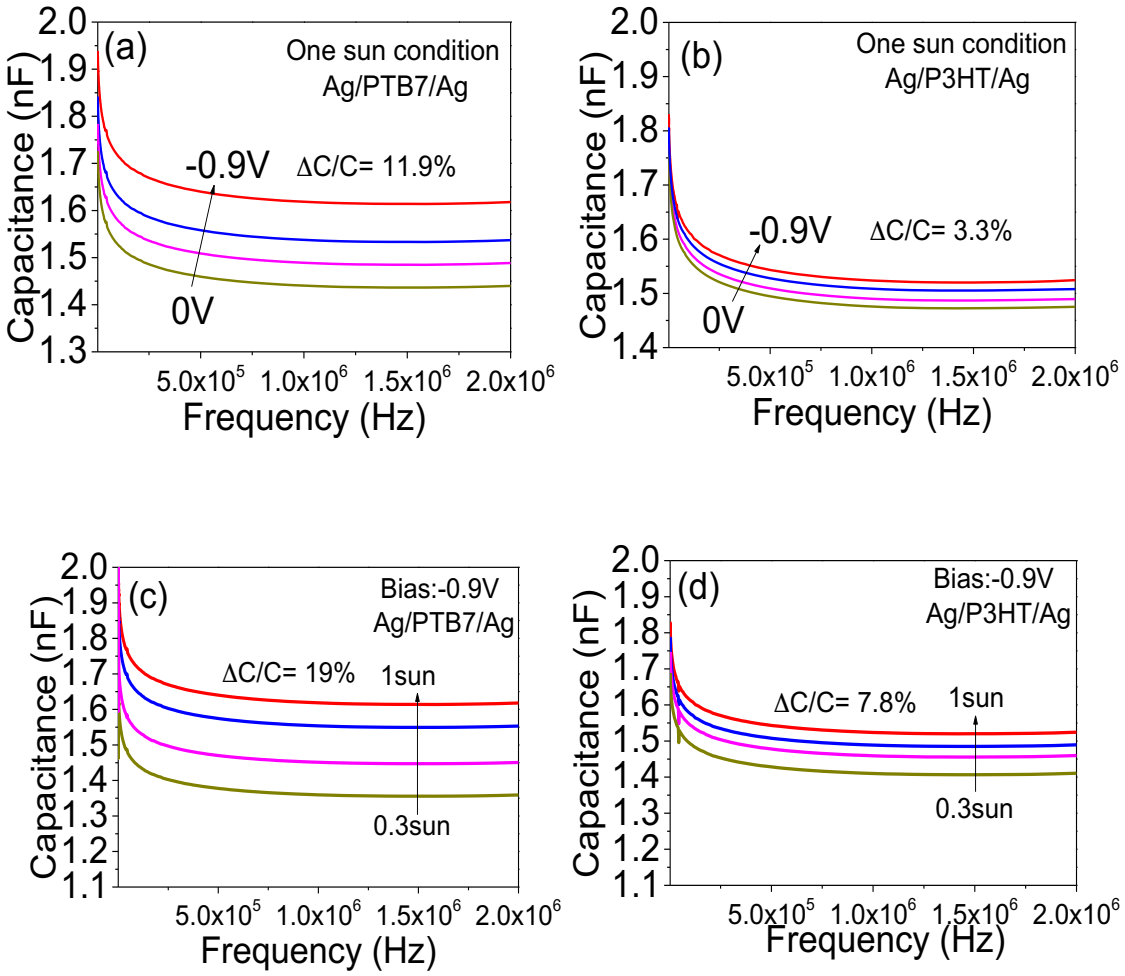

Figure 2-1. (a) Capacitance-frequency characteristics under various reverse biases at one sun condition for PTB7 single layer device. (b) Capacitance-frequency characteristics under various reverse biases at one sun condition for P3HT single layer device. (c) Capacitance-frequency characteristics under various simulated sunlight intensities at -0.9V reverse bias for PTB7 single layer device. (d) Capacitance-frequency characteristics under various simulated sunlight intensities at -0.9V reverse bias for P3HT single layer device.

electrical interaction between the PTB7 and $PC_{60}BM$ components in the PTB7:$PC_{60}BM$ solar cells.

To understand the electrical interaction effects on charge dissociation, we need to monitor the electron-hole pairs at D:A interfaces. It is known that the photoexcited excitons can be significantly dissociated in the bulk-heterojunction PTB7:$PC_{60}BM$ solar cells [94,95]. However, the magneto-PC signal (Figure 2-1 (a)) clearly indicates that the photogenerated charge carriers can inevitably form electron-hole pairs at the D:A interfaces [81]. Here, magneto-PC provides an experimental tool to monitor the e-h pairs at D:A interfaces in organic solar cells. Essentially, the electron-hole pairs are formed with both spin-antiparallel and spin-parallel states with the 1:3 ratio through randomly pairing process. A magnetic field can change the populations of spin-antiparallel and spin-parallel pairs by influencing spin precessions in electron-hole pairs, and consequently modifies the photocurrent due to different dissociation rates, generating a magneto-PC signal. Therefore, magneto-photocurrent can be used as an *in-situ* method to monitor the electron-hole pairs at D:A interfaces in organic solar cells under device-operating condition. Furthermore, we should note that applying an external bias can dissociate the e-h pairs formed at the D:A interfaces, decreasing magneto-PC signal. The electron-hole pairs can be completely dissociated when an external bias increases to a critical value, leading to un-detectable magneto-photocurrent. Essentially, this critical bias can give an estimate on the electron-hole binding energy. Therefore, combining an external critical bias and magneto-photocurrent can provide an experimental method, namely bias-dependent magneto-photocurrent, to estimate the electron-hole binding energy at the D:A interfaces in organic solar cells.

2.4 The effects of intermolecular dipole-dipole interaction on e-h binding energy at D:A interfaces and photovoltaic responses in PTB7:PCBM organic solar cells.

In this section we investigate the effects of dipole-dipole interaction on e-h binding energy at the D:A interfaces with bias-dependent magneto-PC by using the double-beam 532 nm and 325 nm excitations to separately excite the donor and acceptor components in the PTB7:$PC_{60}BM$ solar cells. At the constant intensity of 532 nm of exciting donor-PTB7,

adding the second excitation of 325 nm to excite the acceptor-$PC_{60}BM$ component can gradually quench the magneto-photocurrent signal (Figure 2-3 (a)). This result provides the experimental evidence to support our hypothesis that exciting both donor and acceptor can establish the dipole-dipole interaction between donor and acceptor components and consequently decreases the e-h pairs at the D:A interfaces. With the reduction of magneto-PC magnitude, we can make an argument that optically exciting the $PC_{60}BM$ mainly induce the electrical polarization in the acceptor and consequently enhances the dipole-dipole interaction between the donor and acceptor components with the consequence of dissociating the electron-hole pairs at the D:A interfaces. Furthermore, we can see in Figure 2-3 (b) that, at the constant intensity of 325 nm beam of exciting the acceptor-$PC_{60}BM$, increasing the 532 nm beam intensity of exciting the donor-PTB7 increases the magneto-photocurrent amplitude (Figure 2-3 (b)). The magneto-PC amplitude increases from 0.94 % to 1.73 % and 2.17 % when the 532 nm excitation is increased from 60 mW/cm^2 to 82 mW/cm^2 and 100 mW/cm^2 at the constant intensity of 325 nm beam intensity of 14 mW/cm^2. This increasement of magneto-PC indicates that increasing the 532 nm beam intensity of exciting the donor-PTB7 component can essentially increase the e-h pairs at the D:A interfaces, in addition to introducing the dipoles in the donor component. Nevertheless, simultaneously exciting the donor-PTB7 and the acceptor-$PC_{60}BM$ can establish dipole-dipole interaction between donor and acceptor components in the bulk-heterojunction PTB7:$PC_{60}BM$ solar cells.

Now we characterize the electron-hole binding energy at the D:A interfaces as a function of dipole-dipole interaction in the PTB7:$PC_{60}BM$ solar cells. Here we use the critical bias required to completely quench the magneto-PC signal to estimate the electron-hole binding energy at the D:A interfaces. The critical bias was measured in two different situations: (i) changing the 532 nm beam intensity of exciting the donor at the constant intensity of 325 nm of exciting the acceptor and (ii) changing the 325 nm beam intensity of exciting the acceptor at the constant intensity of 532 nm of exciting the donor. Here, we can see a surprising phenomenon: increasing the 325 nm beam intensity of exciting the acceptor-$PC_{60}BM$ can largely decrease the critical bias required to remove magneto-PC signal (Figure 2-3 (a)). Without the 325 nm beam of exciting the acceptor- $PC_{60}BM$, the

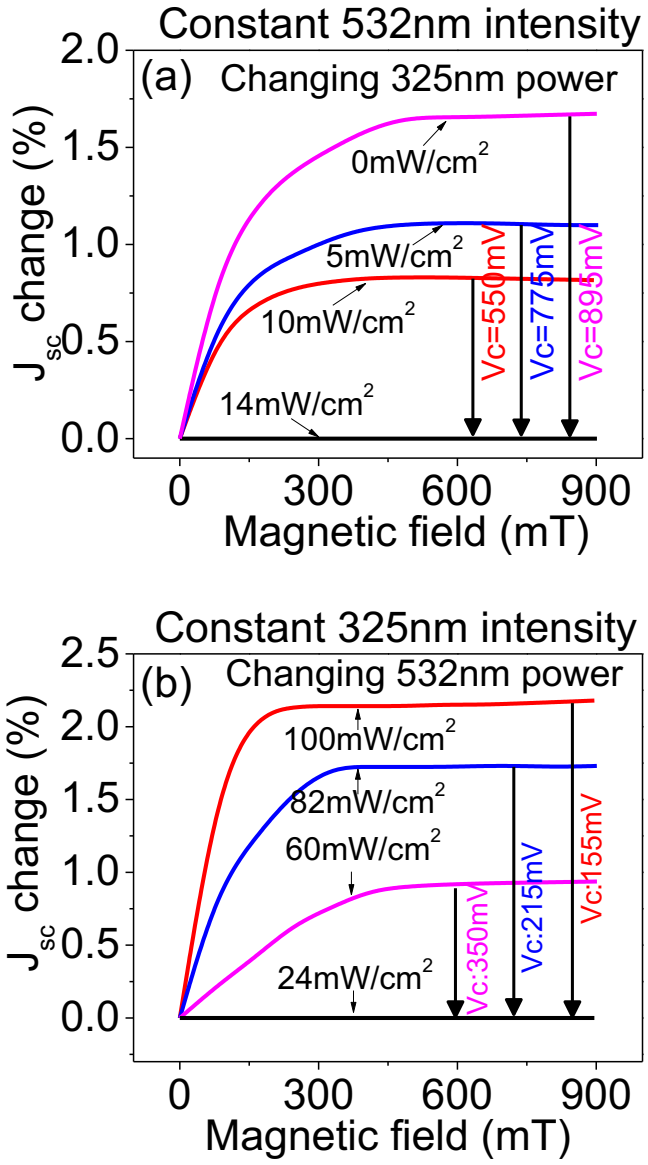

Figure 2-2. Magneto-photocurrents measured by separately exciting donor-PTB7 and acceptor- $PC_{60}BM$. (a) Changing 325 nm intensity of exciting acceptor-$PC_{60}BM$ at constant 532 nm intensity (24mW/cm^2) of exciting donor-PTB7. (b) Changing 532 nm intensity of exciting donor-PTB7 at constant 325 nm intensity (14mW/cm^2) of exciting acceptor-$PC_{60}BM$. The critical bias (*Vc*) is given by the reverse bias required to completely quench magneto-photocurrent signal at each condition.

critical bias becomes 895 mV. When the 325 nm beam intensity is increased from 5 mW/cm^2 to 10 mV/cm^2 and 14 mW/cm^2, the critical bias largely decreases from 775 mV to 550 mV and a negligible value. This means that establishing the dipole-dipole interaction by exciting both the donor-PTB7 and acceptor-$PC_{60}BM$ can largely decrease the electron-hole pairs at the D:A interfaces, leading to an enhanced charge dissociation in the PTB7:$PC_{60}BM$ solar cells. Furthermore, at the constant intensity of 325 nm of exciting the acceptor-$PC_{60}BM$, increasing the 532 nm beam intensity of exciting the donor-PTB7 beam decreases the critical bias, required to completely quench the magneto-photocurrent signal, from 350 mV to 215 mV and 155 mV while the magneto-photocurrent amplitude is increased from 0.94 % to 1.73 % and 2.17 %. This leads to an interesting situation: the charge dissociation at the D:A interfaces becomes easier as the e-h pairs are increased. Normally, increasing the e-h pairs at the D:A interfaces would require a higher critical bias to complete the charge dissociation. Obviously, this interesting situation reflects the dipole-dipole interaction effects. Specifically, increasing the 532 nm beam intensity of exciting the donor can simultaneously increase both the intra-chain dipoles in the PTB7 and the e-h pairs at the PTB7:$PC_{60}BM$ interfaces. The intra-chain dipoles in the PTB7 can form the dipole-dipole interaction with the excited $PC_{60}BM$ component in the PTB7:$PC_{60}BM$ bulk-heterojunctions. The inversion relationship between the critical bias and density of e-h pairs indicates that the dipole-dipole interaction can indeed decrease the electron-hole binding energy at the D:A interfaces. Nevertheless, by separately exciting the donor and acceptor, our magneto-photocurrent studies can confirm that the dipole-dipole interaction between the donor and acceptor components can decrease the electron-hole binding energy at the D:A interfaces, enhancing charge dissociation in the PTB7:PCBM bulk-heterojunctions.

Here we use the P3HT:$PC_{60}BM$ bulk-heterojunctions, where the dipole-dipole interaction is absent, to further understand the optically induced dipole-dipole interaction. It should be pointed out that the P3HT does not have co-existed electron-donating and electron-withdrawing units. Optically exciting the P3HT can only generate photoexcited excitons without generating intra-chain dipoles in the P3HT chains. As a consequence, the P3HT:$PC_{60}BM$ bulk-heterojunctions do exhibit dipole-dipole interaction between the donor and acceptor components when both the donor and acceptor are excited under

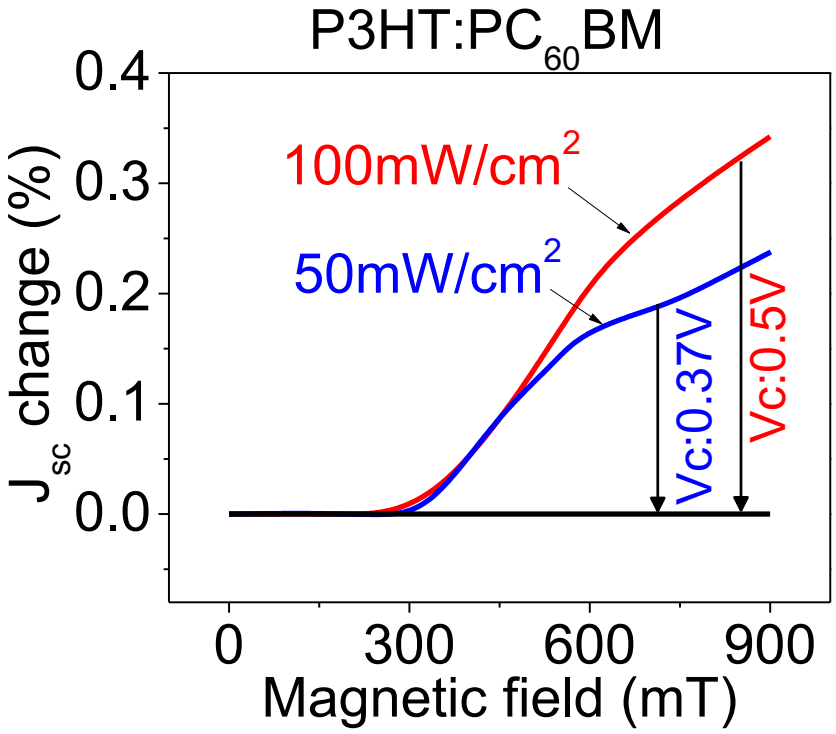

Figure 2-3. Magneto-photocurrents measured at different excitation intensities under simulated sunlight in ITO/PEDOT:PSS/P3HT:PC_{60}BM/Ca/Al device. The critical bias (*Vc*) is determined by the reverse bias required to completely quench magneto-photocurrent signal at each excitation intensity.

simulated sunlight. It is interesting to see in Figure 2-4 that the simulated sunlight generates the magneto-photocurrent signal above 200 mT in the P3HT:PC_{60}BM solar cell. This high-field magneto-PC signal results from the electron-hole pairs at the D:A interfaces [81,83, 96]. Obviously, the e-h pairs are still existed in the P3HT:PC_{60}BM bulk-heterojunctions, opposite to the PTB7:PC_{60}BM bulk-heterojunctions where the electron-hole pairs become non-detectable, under simulated sunlight. Contrarily to the PTB7:PC_{60}BM bulk-heterojunctions, in the P3HT:PC_{60}BM bulk-heterojunctions both the magneto-PC amplitude and the critical bias increases upon increasing photoexcitation. The critical bias is increased from 0.37 V to 0.5 V while the magneto-PC magnitude increases from 0.21 % to 0.34 % (the value at 800 mT) when the sunlight intensity of exciting both the donor-P3HT and acceptor-PC_{60}BM is changed from 50 mW/cm^2 to 100 mW/cm^2. This

result shows that increasing the e-h pairs requires a higher critical bias to complete the charge dissociation upon increasing the beam intensity of 532 nm exciting the donor-P3HT in the P3HT:$PC_{60}BM$ bulk-heterojunctions. On contrast, in the PTB7:$PC_{60}BM$ solar cells increasing the e-h pairs requires a lower critical bias to complete the charge dissociation with increasing the beam intensity of 532 nm of exciting the donor-PTB7. Clearly, this profound difference in the critical bias dependence between the P3HT and PTB7 based solar cells provides further evidence that the dipole-dipole interaction between the donor and acceptor components play an important role to dissociate the electron-hole pairs at the D:A interfaces towards the generation of photovoltaic actions in organic solar cells.

We should note that the electrical potential energies from the critical biases are much lower than the electron-hole binding energies in the PTB7:$PC_{60}BM$ and P3HT:$PC_{60}BM$ systems. However, it should be pointed out that organic solar cells can exist charged defects and trapped carriers in both bulk and electrode interfaces, generating local polarizations under photoexcitation [97-101]. An applied bias can interact with these local polarizations to dissociate the electron-hole pairs. As a consequence, even an external bias does not provide enough potential energies to overcome the electron-hole binding energy, it can still increase the charge dissociation through local polarizations in organic solar cells [102-105]. Nevertheless, the critical bias required to completely quench magneto-PC can be used to reflect the electron-hole binding energy at the D:A interfaces. It should be also noted that the PTB7:$PC_{60}BM$ bulk-heterojunctions form an amorphous morphology with three structures: PTB7 phase, $PC_{60}BM$ phase, and mixed PTB7:$PC_{60}BM$ phase [106,107]. The D:A interfaces can exist both between the PTB7 and $PC_{60}BM$ phases and within the mixed PTB7:$PC_{60}BM$ phase. We should also note that within amorphous structures the optically generated dipole-dipole interaction between donor and acceptor components can be isotropically formed within the active PTB7:$PC_{60}BM$ film. However, our studies indicate that the dipole-dipole interaction still exists in the amorphous PTB7:$PC_{60}BM$ bulk-heterojunctions. This means that the built-in field under device-operating condition can induce a certain orientation on the dipole-dipole interaction in amorphous bulk-heterojunctions. As a result, the dipole-dipole interaction can influence the electron-hole binding energy at the D:A interfaces in organic solar cells.

Here, we verify the effect of optically generated dipole-dipole interaction on photovoltaic actions. Specifically, the double-beam excitations are adjusted to a similar photocurrent generated by simulated sunlight. In this situation, the double-beam and simulated sunlight have the same nominal intensity. We can see in Figure 2-3 that the double-beam 325 nm and 532 nm excitations at 14 mW/cm^2 and 24 mW/cm^2 lead to un-detectable magneto-PC in the PTB7:$PC_{60}BM$ solar cells. This means that, by the 14 mW/cm^2 from 325 nm beam and 24 mW/cm^2 from 532 nm beam, the optically dipole-dipole interaction can sufficiently dissociate the electron-hole pairs at the D:A interfaces. More importantly, combining the 14 mW/cm^2 from 325 nm beam and 24 mW/cm^2 from 532 nm beam produces a similar photocurrent as compared to the simulated sunlight in the PTB7:$PC_{60}BM$ system. In this situation, the double-beam and simulated sunlight have the same nominal intensity. Under the same nominal intensity, we can see that the simulated sunlight generates larger *FF* and V_{oc} relative to the double-beam 532 nm and 325 nm excitations (Figure 2-5 (a)). In the PTB7:$PC_{60}BM$ system the *FF* and V_{oc} are determined to be 59% and 0.72V under simulated sunlight operation. However, the *FF* and V_{oc} are slightly decreased to 51% and 0.70V under the double-beam 532 nm and 325 nm excitations with the same minimal intensity. We know that simulated sunlight operation can lead to more dipole-dipole interaction due to broad-range absorption as compared to the double-beam 532nm and 325nm excitations. The deference in *FF* and V_{oc} between simulated sunlight and double-beam operations reflects that the optically generated dipole-dipole interaction can essentially enhance the charge transport and built-in field during the *FF* and V_{oc} developments. Clearly, our *I-V* characterization indicates that optically generated dipole-dipole interaction can strengthen charge dissociation, charge transport, and built-in field during photovoltaic development in organic solar cells. Therefore, optically generated dipole-dipole interaction can function as an effective method to enhance photovoltaic actions in low-dielectric organic materials.

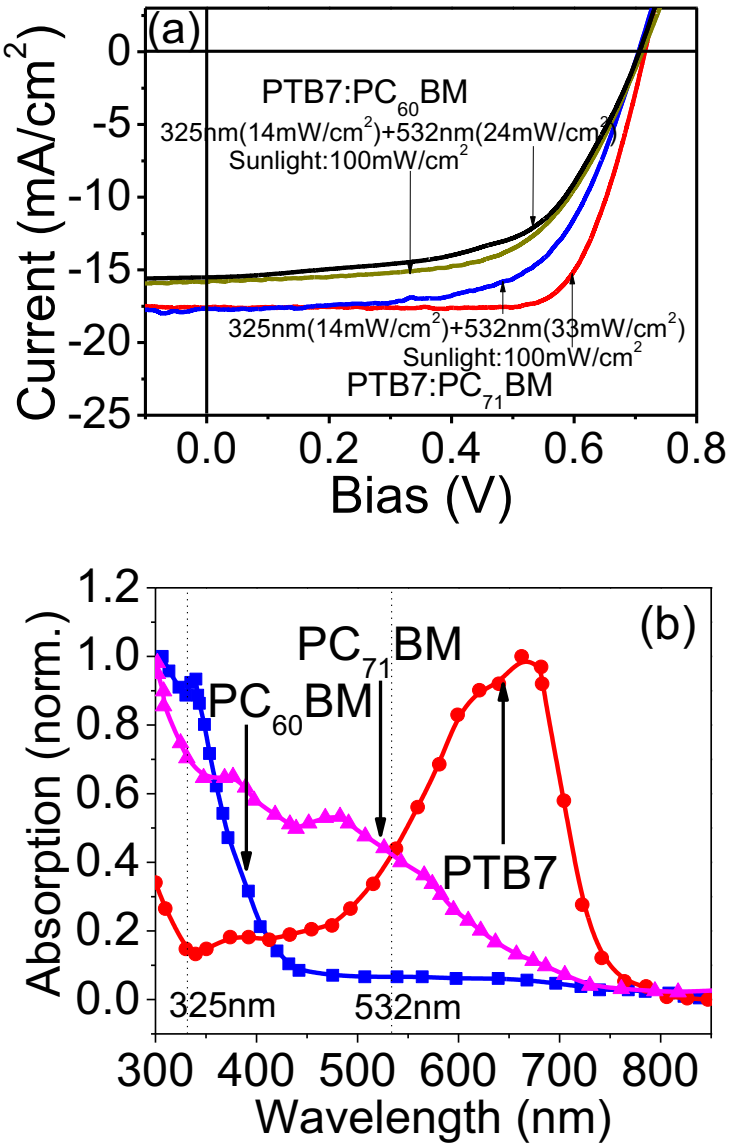

Figure 2-4. (a) The *I-V* characteristics measured by double-beam 325 nm (14mW/cm^2) and 532nm (24mW/cm^2) and simulated sunlight excitation for ITO/PFN/PTB7:$PC_{60}BM$/MoO_3/Ag device. (b) Absorption spectra for donor-PTB7 and acceptor-$PC_{60}BM$.

2.5 Conclusion

In this chapter, we use double-beam 532 nm and 325 nm excitations to separately excite the donor-PTB7 and acceptor-$PC_{60}BM$ components to establish the dipole-dipole interaction in the PTB7:PCBM solar cells. The dipole-dipole interaction essentially originates from the Coulomb interaction between optically generated PTB7-dipoles and optically polarized $PC_{60}BM$ under sunlight excitation. At the same time, we use the critical bias required to completely quench the magneto-PC to characterize the electron-hole binding energy at the D:A interfaces when the dipole-dipole interaction is optically tuned by separately controlling the 532 nm and 325 nm excitations. We observe a surprising phenomenon: increasing the electron-hole pairs at the D:A interfaces decreases the critical bias to completely dissociate the electron-hole pairs in the PTB7:$PC_{60}BM$ solar cells when both the donor-PTB7 and acceptor-$PC_{60}BM$ are excited to establish dipole-dipole interaction between donor and acceptor components. This indicates that optically generated dipole-dipole interaction can facilitate the charge dissociation at the D:A interfaces in the PTB7:$PC_{60}BM$ solar cells. Contrarily, when the optically generated dipoles are absent, increasing the electron-hole pairs at the D:A interfaces causes an increasement on the critical bias to completely dissociate the e-h pairs in the P3HT:$PC_{60}BM$ solar cells. By comparing these two opposite situations, we can see that optically generated dipole-dipole interaction plays an important role to dissociate the electron-hole pairs at the D:A interfaces in organic solar cells. Simultaneously, we can see that the dipole-dipole interaction can increase the V_{oc} and FF by comparing the I-V characteristics measured by double-beam excitations and simulated sunlight at the same nominal intensity.

Chapter 3 Magneto-Optical Studies on Electron-Hole Pairs Dissociation and Recombination in Perovskite Solar Cells

3.1 Introduction

According to chapter 1, the organo-metal halide perovskite shows an extreme low e-h binding energy under photoexcitation [36,37,108], which is from 16 meV to 98 meV. With this low binding energy that a quick e-h pairs dissociation can be happened under room temperature [19,20]. Therefore, the OMHPs provide a unique advantage to develop high-efficiency solar cells. In this chapter, magneto-photocurrent (magneto-PC) and magneto-photoluminescence (magneto-PL). It should be noted that in 1994 the magneto-absorption phenomena were reported at low temperature of 4.2K and high field (20 Tesla) for OMHP ($CH_3NH_3PbI_3$) when the optical absorption was measured as a function of magnetic field [36]. Here, a low field measurement (< 1 tesla) at room temperature will be introduced in our measurement. It's known that the dissociation of e-h pairs can lead to a generation of photocurrent, and on the other hand, the recombination of e-h pairs can cause a generation of both radiative and non-radiative recombination. In this chapter, we focus on the radiative recombination in this chapter because of that the radiative recombination has been reported as a dominant species to contribute to the photoluminescence [109,110]. Meanwhile, the radiative recombination has been thought as an important parameter to determine the photovoltaic response, especially for open circuit voltage [111]. As a result, we will apply magneto-PC to study the charge dissociation and magneto-PL to study the charge recombination within OMHP poly-crystals. Clearly, understanding the recombination and dissociation of photogenerated carriers is a critical issue to control the photovoltaic actions in OMHP solar cells. (The non-radiative recombination of e-h pairs in OMHP crystals will be discussed in chapter 5)

In this chapter, we will use our magneto-PC and magneto-PL combining with different photoexcitation intensities to study the intensity dependent change recombination and dissociation. Our purpose is to investigate whether the recombination (dissociation)

mechanism of photogenreated excited states in OMHP solar cells can be changed when we change the photoexcitation intensity.

3.2 Experiment

The device making procedure has been introduced in chapter 1. Here, we will use p-i-n device structure, which is ITO/PEDOT:PSS/$CH_3NH_3PbI_{3-x}Cl_x$/PCBM/TiOx/Al, to study the photoexcitation intensity dependent charge dissociation and recombination. Figure 3-1 shows the measurement setup of magneto-PL and magneto-PC. Both measurements are recorded by measuring the signal (PC or PL) as a function of magnetic field at room temperature. The amplitude of magneto-PL and magneto-PC is defined as $\frac{I_B - I_0}{I_0}$, where the I_B and I_0 are the photocurrents or photoluminescence with and without magnetic field at short-circuit condition. Here, the photocurrent characteristics were measured by using Keithley 2400 source meter. The photoluminescence measurements were performed by using SPEX Fluorolog 3 spectrometer.

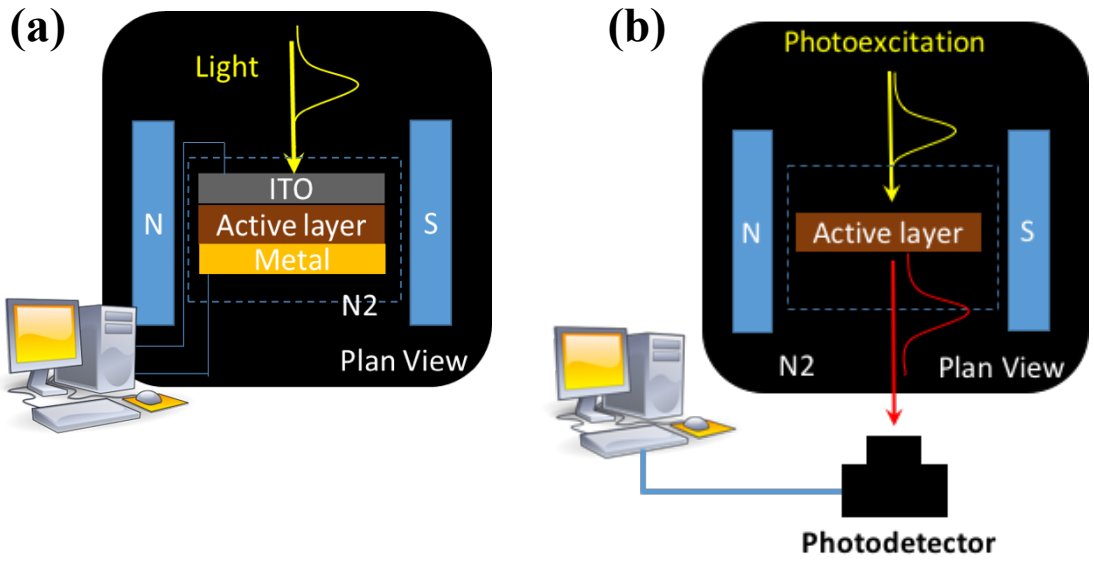

Figure 3-1. Experimental setups for (a) magneto-photocurrent and (b) magneto-photoluminescence.

3.3 Spin dependent charge dissociation and recombination process under different photoexcitation intensities

Figure 3-2 (a) shows the magneto-PCs at different excitation intensities from the continuous wave (CW) laser beam of 532nm in OMHP solar cells with the device architecture of ITO/PEDOT:PSS/$CH_3NH_3PbI_{3-x}Cl_x$/$PC_{71}BM$/TiOx/Al. We can see that, when the photoexcitation intensity is greater than 15mW/cm^2, the photocurrent becomes a function of magnetic field at room temperature and low field (< 150mT), leading to a positive magneto-PC. The magneto-PC signal gradually increases and then becomes saturated around 150mT. This magneto-PC indicates that the generation of photocurrent undergoes a spin-dependent process. Here, the magneto-PC amplitude is defined by $\frac{I_B - I_0}{I_0}$, where the I_B and I_0 are the photocurrents with and without magnetic field. Under 1 sun condition our devices can yield a power efficiency of around 14 % (*Jsc*: 22.1mA/cm^2; *Voc*: 0.91V; *FF*: 0.68) (Figure 3-2 (b)). To confirm that the magneto-PC is an intrinsic magneto-optical phenomenon, we have measured the perovskite device without charge transporting PEDOT:PSS and TiOx layers. We can see in Figure 3-2 (c) that the perovskite-only device (ITO/perovskite/Al) exhibits a clear magneto-PC at room temperature when the photoexcitation intensity exceeds 72 mW/cm^2. In addition, we should note that the PEDOT:PSS and PCBM can possibly demonstrate magneto-current phenomena when electron-hole pairs are generated [112 - 114]. We find that the control device (ITO/PEDOT:PSS/$PC_{71}BM$/TiOx/Al) without the perovskite layer does not show any detectable magneto-PC in our measurements. Therefore, we can confirm that the observed magneto-PC is an intrinsic phenomenon occurring in the OMHPs. Furthermore, we can see in Figure 3-2 (d) that the photocurrent (*Jsc*) – excitation curve can be well described by non-geminate charge recombination ($Jsc = A + B \cdot \exp(C \cdot P)$), where the P is the photoexcitation intensity, and A, B, and C are coefficients. Therefore, we can suggest that the magneto-PC phenomena are essentially generated by the non-geminate recombined electron-hole pairs in OMHPs.

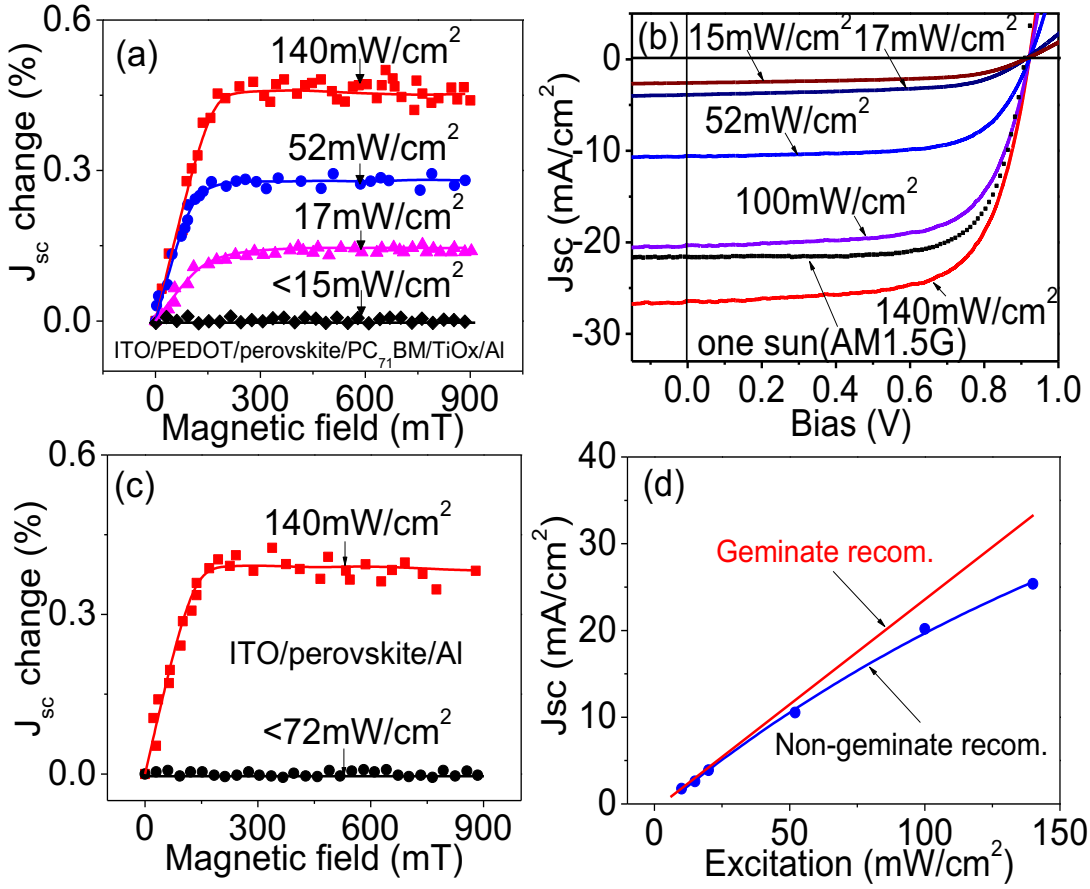

Figure 3-2. Magneto-photocurrents and current-voltage characteristics at different excitation intensities from 532nm CW laser in the ITO/PEDOT:PSS/$CH_3NH_3PbI_{3-x}Cl_x$/PC_{71}BM/TiOx/Al solar cell. (a) Positive magneto-photocurrent signals at room temperature. (b) Current-voltage characteristics. The dashed *I-V* curve is for 1 sun condition under AM1.5G solar simulated sun light. (c) Magneto-photocurrents for perovskite-only device (ITO/$CH_3NH_3PbI_{3-x}Cl_x$/Al) at different excitation intensities. (d) Short-circuit current (J_{sc}) as a function of excitation intensity (Squares: experimental data. Curve fitting by using geminate and non-geminate recombination).

We should note that OMHPs can exhibit a strong spin-orbital coupling (SOC) due to heavy elements. In general, a strong SOC can cause a significant spin mixing between different spin states, leading to negligible magnetic field effects at low field and room temperature [115,116]. Here, we should mention that our room-temperature magneto-optical phenomena can be observed only if the photoexcitation intensity exceeds certain value of 15 mW/cm^2, namely threshold intensity. Below this threshold intensity (15 mW/cm^2) the magneto-PC becomes negligible even though the photocurrent still shows appreciable values. This leads to a hypothesis that the spin-dependent recombination of photogenerated free electrons and holes is still operative to generate magnetic field effects under strong SOC. To further understand the origin of magneto-PC, we have studied the magneto-PL from the OMHPs at room temperature. A negative magneto-PL can be observed in the OMHPs ($CH_3NH_3PbI_{3-x}Cl_x$) when the photoexcitation intensity is greater than $120mW/cm^2$ (Figure 3-3 (a)). This is the first experimental observation that photoluminescence is a spin-dependent process at room temperature and low field (< 200mT) in OMHPs. The negative magneto-PL amplitude gradually increases and then becomes saturated around 200mT with increasing magnetic field. We should also note that this magneto-PL becomes negligible when the photoexcitation intensity is below $120mW/cm^2$, although a strong photoluminescence still exists (Figure 3-3 (b)). Based on the fact that the photoluminescence results from charge carrier recombination, the observed magneto-PL can show that an external magnetic field can change the spin states in electron-hole pairs and consequently modifies the ratio of radiative singlet e-h pairs and non-radiative triplet e-h pairs in OMHPs. Here, it is noted that the magneto-PC and magneto-PL show opposite signs with a common Lorentzian line-shape characteristic $[\Delta I(B)/I \propto [B^2/(B^2+B_0^2)]$ (Figure 3-4 (a)). The opposite signs between magneto-PC and magneto-PL can experimentally indicate that a magnetic field can decrease the antiparallel spin states (singlet states) but increases the parallel spin states (triplet states) in electron-hole pairs by suppressing the spin mixing through introducing in-phase spin precessions. This essentially leads to a decrease on the singlet exciton formation required for photoluminescence. However, decreasing the exciton formation rate can consequently lead

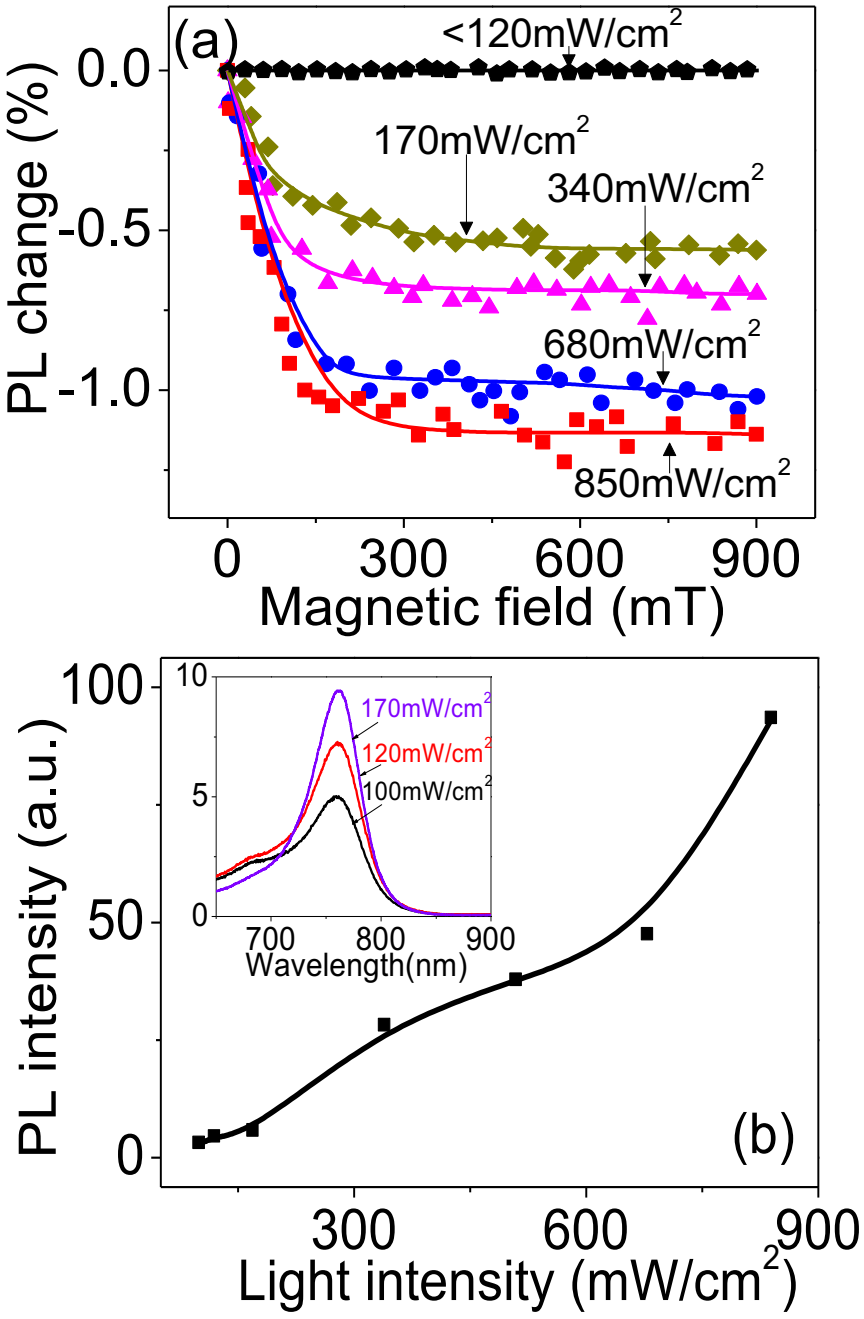

Figure 3-3. Magneto-photoluminescence at room temperature in perovskite film. The photoexcitation source is from 532nm CW laser. (a) Negative magneto-photoluminescence signals at different excitation intensities. (b) The photoluminescence intensity as a function of excitation intensity. The inset shows photoluminescence spectra at different excitation intensities below and above the threshold intensity of 120mW/cm^2.

to more the electron-hole pairs available for charge dissociation towards generating photocurrent, as shown in Figure 3-4 (b). Clearly, the observed magneto-PL and magneto-PC indicate that spin-dependent charge recombination and dissociation are operative under spin mixing between different spin states in electron-hole pairs in OMHPs. The early studies on magneto-electroluminescence (magneto-EL) in organic semiconductors have demonstrated that hyperfine coupling [117,118] and Δg mechanism [84,86] can lead to a spin mixing between antiparallel and parallel spin states. Changing spin mixing has been shown as an important mechanism to generate magnetic field-dependent phenomena in organic materials [119]. Here, our negative magneto-PL and positive magneto-PC do not suggest that the Δg mechanism plays a dominant role in spin mixing processes in perovskite poly-crystals. This leaves the internal interactions, such as hyperfine coupling, as a dominant mechanism for spin mixing in our situation. Nevertheless, by disturbing the spin mixing in electron-hole pairs and applying Pauli Exclusion Principle on excitonic states, magneto-PL and magneto-PC can be generated through spin-dependent charge recombination and dissociation in electron-hole pairs formed through non-geminate recombination processes in OMHPs.

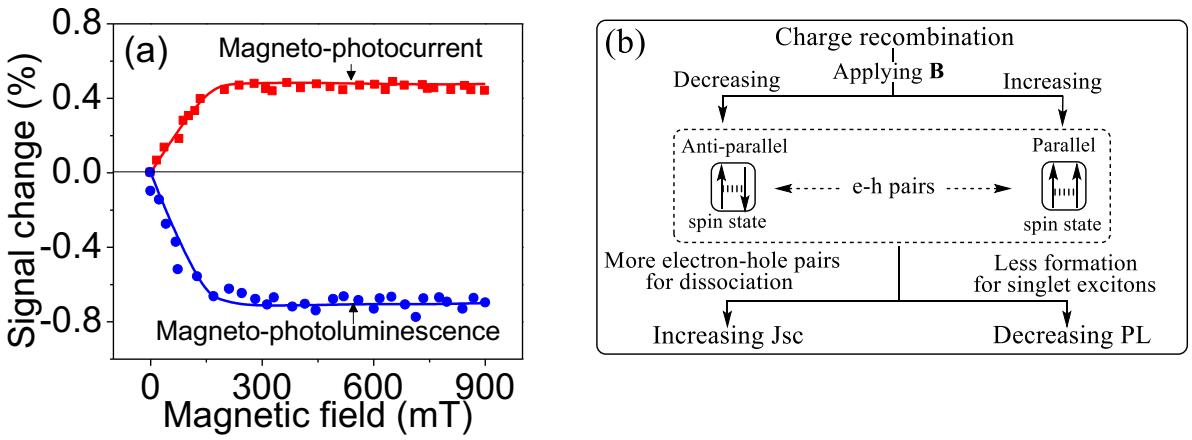

Figure 3-4. (a) Line-shape characteristics for positive magneto-photocurrent and negative magneto-photoluminescence. (b) Diagram to schematically show magnetic field-dependent antiparallel/parallel ratio in electron-hole pairs to generate positive magneto-photocurrent and negative magneto-photoluminescence in OMHPs.

3.4 The modulation of spin-exchange energy in electron-hole pairs under different photoexcitation intensities

The mutual interactions between electron-hole pairs can occur when the charge density is increased upon increasing photoexcitation intensity. The mutual interactions between electron-hole pairs are essentially dipole-dipole interactions. The early experimental studies have shown that the interactions between charge-transfer states can cause a line-shape narrowing phenomenon on the magneto-PL in organic semiconductors as the photoexcitation intensity is increased [85]. This is because the interactions between charge-transfer states can weaken the internal interactions, namely spin-exchange interactions, within charge-transfer states, leading to a larger change on the ratio of antiparallel/parallel spin pairs upon applying a magnetic field [120-122]. Here, we can see a similar phenomenon in OMHPs: the line-shape narrowing phenomenon occurs on both magneto-photocurrent and magneto-photoluminescence when the photoexcitation intensity is increased (Figure 3-5). The saturation field for magneto-PC signal is decreased from 480mT to 400mT when the photoexcitation intensity is increased from 17mW/cm^2 to 140mW/cm^2. In addition, the saturation field for magneto-PL signal is reduced from 530mT to 435mT as the photoexcitation intensity is increased from 170mW/cm^2 to 850mW/cm^2. Clearly, the line-shape narrowing phenomenon provides an evidence that the mutual interactions between electron-hole pairs are indeed existed in OMHPs. Essentially, the mutual interactions between electron-hole pairs can provide an additional mechanism to control the electron-hole binding energies towards generating photocurrent in perovskite solar cells.

3.5 Density dependent electron-hole binding energy in organo-metal halide perovskite solar cells.

Now we use the observed magneto-PC and magneto-PL to discuss the dissociation effects in electron-hole pairs in OMHPs. Because the captured electron-hole pairs can generate two opposite outcomes: generating free carriers through charge dissociation or emitting photoluminescence through radiative annihilation, controlling the recombination and dissociation in e-h pairs is a critically important for the generation of photocurrent in perovskite solar cells. Here, we study the charge recombination and dissociation at

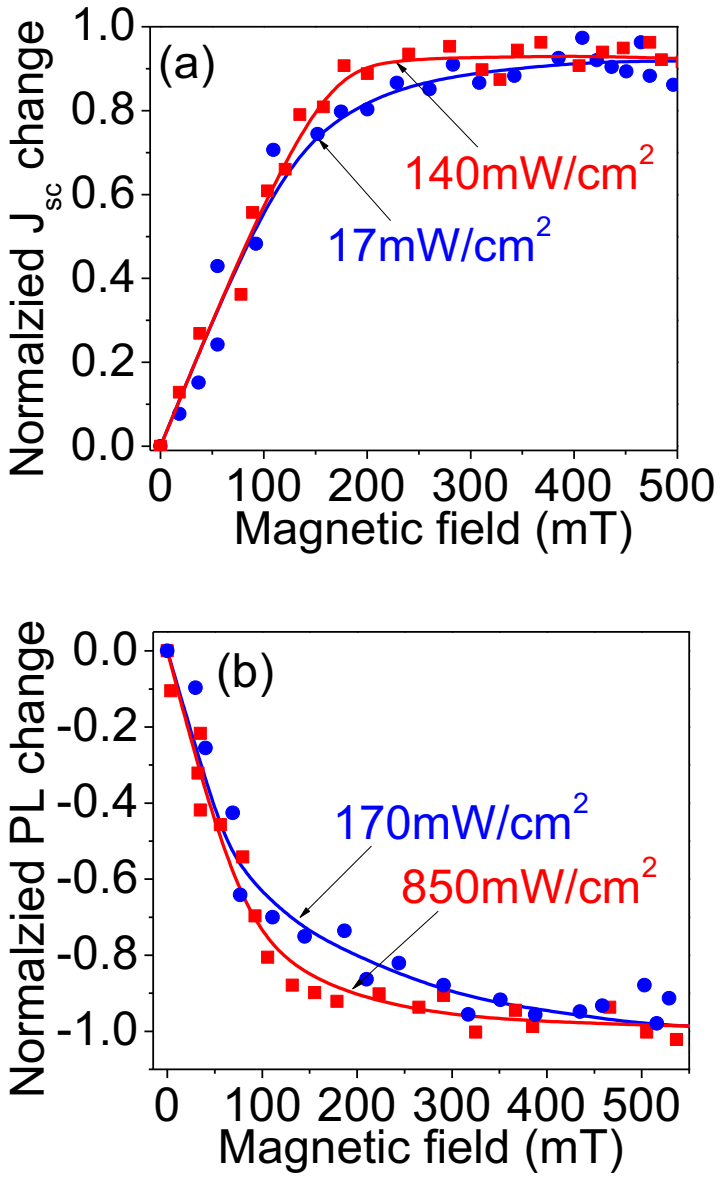

Figure 3-5. (a) Normalized magneto-photocurrent characteristics at 140mW/cm^2 and 17mW/cm^2. (b) Normalized magneto-photoluminescence characteristics at 850mW/cm^2 and 170mW/cm^2. The photoexcitation source is 532nm CW laser

different carrier densities by using magneto-PC and magneto-PL in combination with an external bias upon varying photoexcitation intensity. Combining magneto-PC and magneto-PL with an external bias can provide a convenient experimental method to explore the binding energy in electron-hole pairs based on the following two procedures (as shown in Figure 3-6). Firstly, we use magneto-PC and magneto-PL to monitor the recombination and dissociation in e-h pairs. Secondly, applying a reverse bias can lead to a decrease on the magneto-PC and magneto-PL signal amplitudes. When an external bias reaches a critical value, the magneto-PC and magneto-PL signals can be completely quenched due to the thorough dissociation of electron-hole pairs. As a result, measuring magneto-PC and magneto-PL under different biases can reveal how the charge dissociation changes with charge density in electron-hole pairs upon changing excitation intensity. Figure 3-7 shows the magneto-PC quenching caused by a reverse bias at different excitation intensities in the ITO/PEDOT:PSS/$CH_3NH_3PbI_{3-x}Cl_x$ /$PC_{71}BM$/TiOx/Al device. We can see that it requires a higher bias to completely quench the magneto-PC signal when a stronger photoexcitation is applied. At the photoexcitation intensities of 140mW/cm^2, 52mW/cm^2, and 17mW/cm^2, the critical biases required to eliminate the magneto-photocurrent signal are determined to be 105 mV, 65 mV, and 37 mV. Clearly, it requires a stronger field to complete the charge dissociation at higher carrier density towards generating photocurrent in OMHPs. We should note that the electrical potential energies from these critical biases are much lower than the electron-hole binding energies (37meV to 98meV) reported for OMHPs. However, it should be pointed out that the perovskite solar cells can exist both bulk and interfacial polarizations due to charged defects and trapped carriers under photoexcitation [97-101]. A reverse bias can facilitate these internal polarizations to dissociate the electron-hole pairs. Therefore, the internal polarizations can play an important role in charge dissociation under a reverse bias. As a consequence, even an external bias does not provide enough potential energies to overcome the electron-hole binding energies, it can still increase the charge dissociation through internal polarizations in perovskite solar cells. The similar phenomena have been also observed in organic solar cells [102-105]. Nevertheless, from the fact that increasing photoexcitation intensity leads

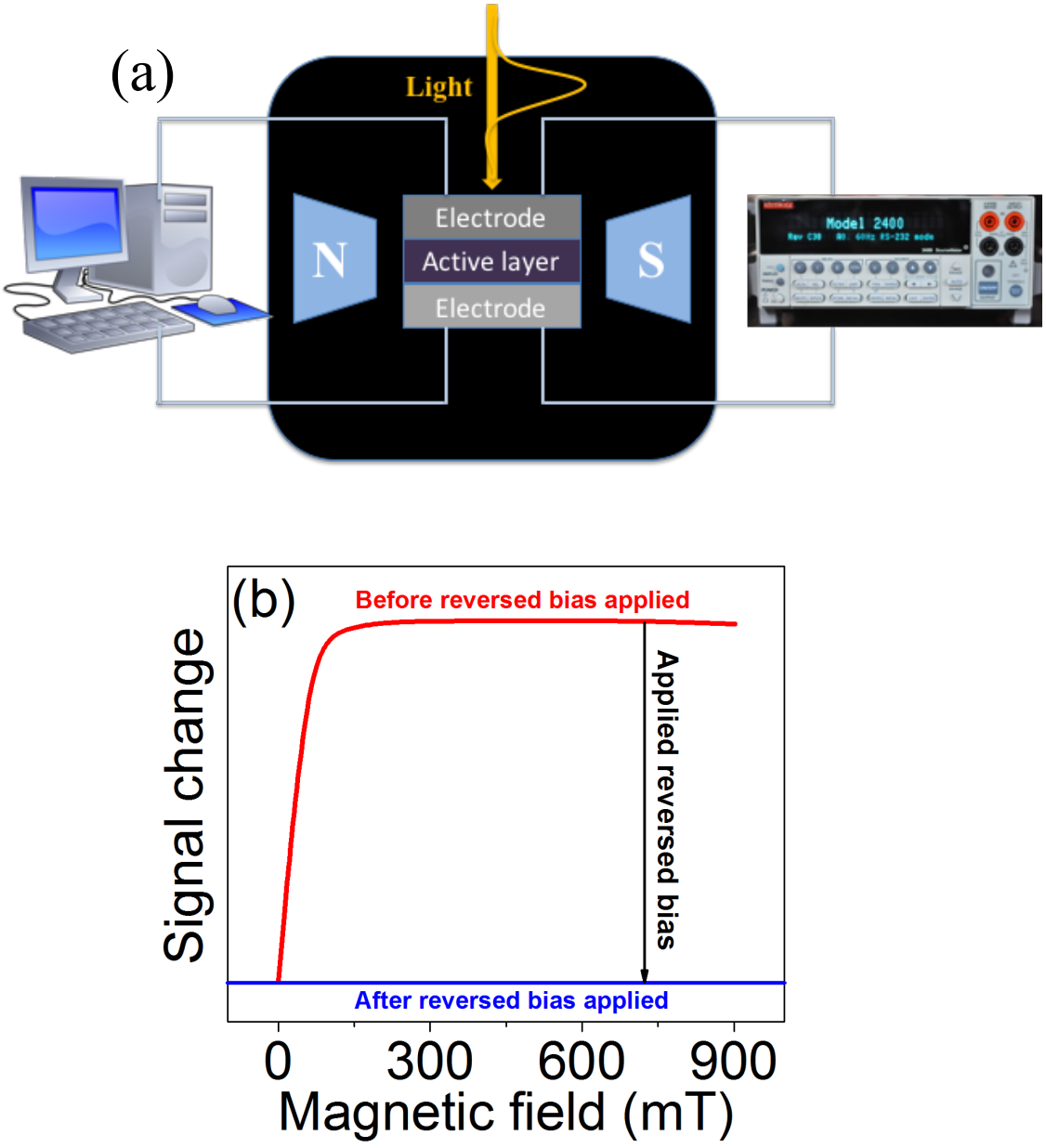

Figure 3-6. (a) Experimental setup for e-h binding energy measurement. (b) Typical curve evolution for binding energy measurement.

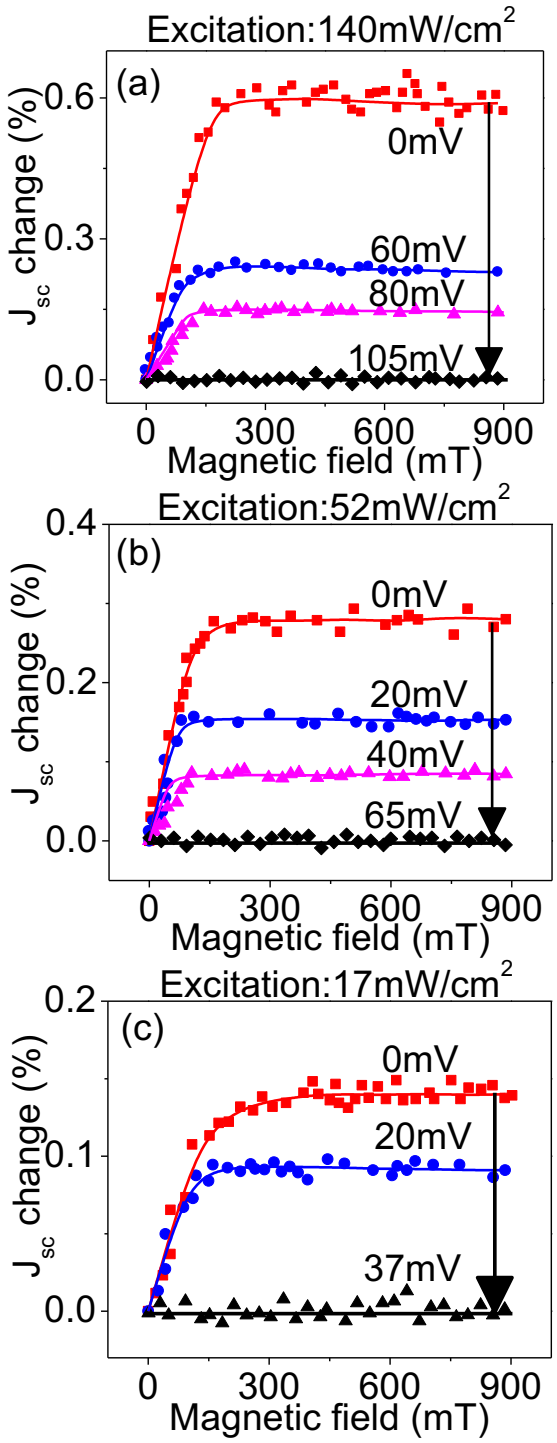

Figure 3-7. Magneto-photocurrent quenching caused by reverse bias at different excitation intensities to show dissociation effects at different charge densities in ITO/PEDOT:PSS/$CH_3NH_3PbI_{3-x}Cl_x$/$PC_{71}BM$/TiOx/Al device. The photoexcitation is from 532nm CW laser. (a) Critical bias=105mV at 140mW/cm^2. (b) Critical bias=65mV at 52mW/cm^2. (c) Critical bias=37mV at 17mW/cm^2.

to an increase on the critical bias required to completely quench the magneto-PC signal, we can see that the charge dissociation becomes a function of the density of electron-hole pairs. A higher density of electron-hole pairs requires a stronger field to complete the charge dissociation. Our photoluminescence results provide further evidence to support this argument. Figure 3-8 shows electric field-induced photoluminescence quenching at different excitation intensities for the ITO/PMMA/$CH_3NH_3PbI_{3-x}Cl_x$/PMMA/Al device. Here the perovskite film is sandwiched between two insulating PMMA layers to avoid injection current in measuring electric field effects of magneto-PL. We can see a similar phenomenon: a higher electric field is required to completely quench the photoluminescence signal at a higher excitation intensity. Increasing excitation intensity from 17mW/cm^2 to 52mW/cm^2 and 140mW/cm^2 causes an increase on the required bias from 1.2V to 3.3V and 7.4V to quench the photoluminescence by 80%. It is noted that quenching the photoluminescence in the ITO/PMMA/perovskite/PMMA/Al device needs a much larger bias than quenching the photocurrent in the ITO/PEDOT:PSS/$CH_3NH_3PbI_{3-x}Cl_x$/$PC_{71}BM$/TiOx/Al device. This is because the former and latter devices possess weaker and stronger internal polarizations, respectively. Nevertheless, the electric field-induced photoluminescence quenching at different excitation intensities confirms that the charge dissociation is a function of carrier density in OMHPs. A higher density of electron-hole pairs corresponds to a stronger e-h pairs binding energy, which lead to a requirement of stronger electrical field to complete the charge dissociation towards the generation of photocurrent in perovskite solar cells.

3.6 Conclusion

In summary, the positive magneto-PC and negative magneto-PL are observed at room temperature and low field (< 200mT) in OMHPs when the photoexcitation exceeds the threshold intensities. Our results indicate that the photogenerated charge carriers undergo a spin-dependent recombination to form non-geminate electron-hole pairs, functioning as intermediate states, to generate two opposite outcomes: radiative annihilation towards light emission and charge dissociation towards photocurrent. The negative magneto-PL and positive magneto-PC show that an external magnetic field can

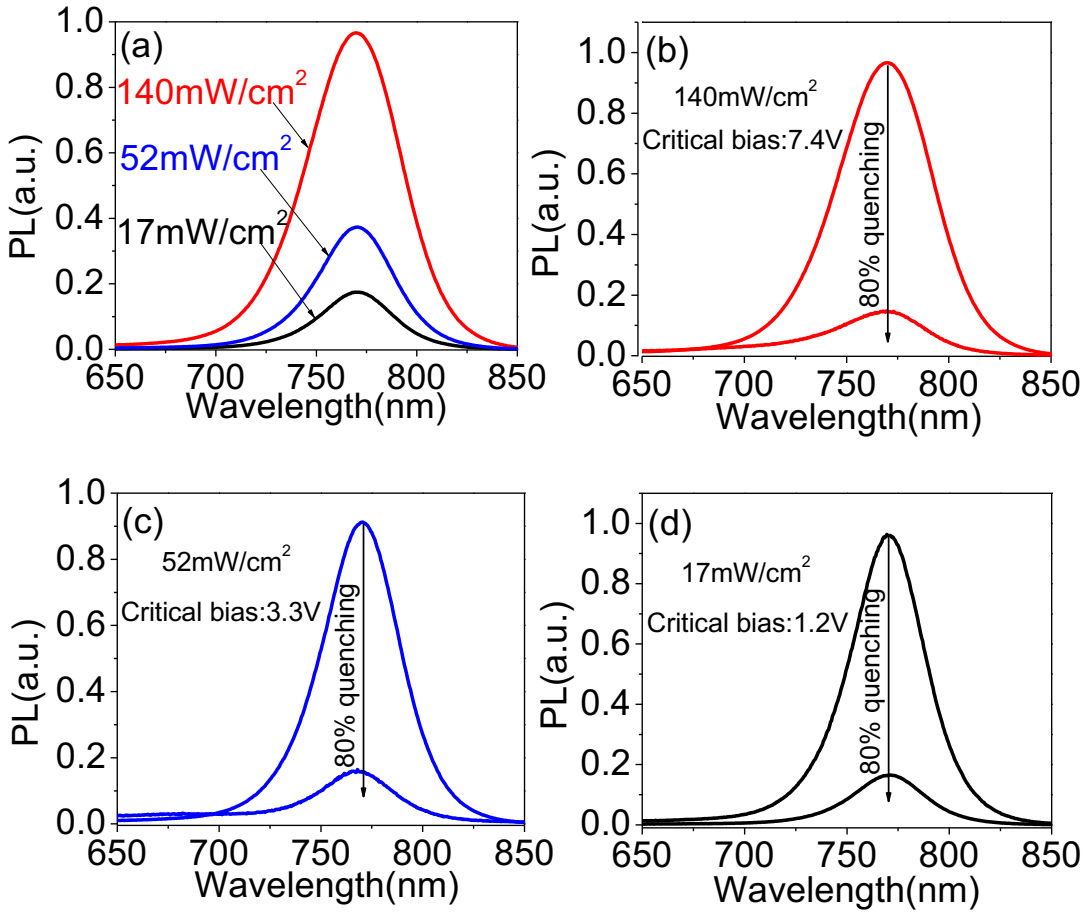

Figure 3-8. Electric field-induced photoluminescence quenching at different excitation intensities (532nm laser). The excitation intensities of 17mW/cm^2, 52mW/cm^2, and 140mW/cm^2 require the critical biases of 1.2V, 3.3V, and 7.4V, respectively, to quench the photoluminescence by the same percent (80 %).

suppress the spin mixing between antiparallel and parallel spin states by introducing in-phase spin precessions, decreasing the branching ratio of antiparallel/parallel spin states (singlet/triplet) in electron-hole pairs. Because of the Pauli Exclusion Principle applied onto excitonic states, decreasing the branching ratio of antiparallel/parallel spin states in electron-hole pairs can essentially decrease the photoluminescence by reducing the formation of light-emitting excitons. However, this can lead to more electron-hole pairs available for charge dissociation, generating an increase on the photocurrent. Clearly, the charge recombination and dissociation in electron-hole pairs are a spin-dependent process, leading to magnetic field effects at room temperature and low field (< 200mT) in OMHPs. Furthermore, we find that increasing photoexcitation intensity can largely increase the critical bias required to completely quench the magneto-PC and magneto-PL signals. This indicates that a higher density of electron-hole pairs necessitates a stronger field to complete charge dissociation towards generating photocurrent. In addition, we observe that a line-shape narrowing phenomenon occurs on magneto-PC and magneto-PL signals upon increasing photoexcitation intensity. This implies that the electron-hole pairs experience mutual dipole-dipole interactions, which can weaken the spin-exchange energies within electron-hole pairs, as the charge density increases. The mutual interactions can provide an additional mechanism to manipulate the electron-hole binding energies for changing the charge dissociation towards generating photocurrent. Therefore, our magneto-optical studies provide a new understanding on spin-dependent charge recombination and dissociation to further improve photovoltaic actions in OMHPs.

Chapter 4 The Dipole Effect of Interfacial Layer on Photovoltaic Responses in Organo-Metal Halide Perovskite Photovoltaic Cells

4.1 Introduction

The fundamental opto-electronic properties of OMHPs, such as low binding energy, long charge diffusion length, and high dielectric constant, made it uniquely suited for photovoltaic application. Along with the growing interest in OMHP solar cells, materials selection, device structure, and in-depth understanding of the physics associated with the performance of a given design comes as a vital issue. Especially, the interfacial engineering has been thought as an important approach to further improve the efficiency of OMHPs [7,123,124]. Although the intrinsic properties, such as crystallinity and morphology, of perovskite as the active layer are the most decisive parameters in the overall performance, but other factors, such as the energy level matching with electron transport layer (ETL) or hole transport layer (HTL), are also very crucial to further enhance the efficiency of OMHP photovoltaic cells.

In general, an ideal ETL or HTL should have a matched charge mobility with active layer along with the energy band structure and chemical compatibility with the photovoltaic active layer. In addition, morphology and crystallinity of charge transport layers play an important role. In this chapter two different organic HTLs will be used in OMHP perovskite solar cells, one is PTB7 (Poly[[4,8-bis[(2-ethylhexyl)oxy]benzo[1,2-b:4,5-b']dithiophene-2,6-diyl][3-fluoro-2-[(2-ethylhexyl)carbonyl]thieno[3,4-b]thiophenediyl]]), the other one is P3HT (Poly(3-hexylthiophene-2,5-diyl)). As shown in chapter 2 that the PTB7 can generate an intra-molecular electrical dipole within molecular structures under photoexcitation [69-71]. On the other hand, we choose P3HT (Poly(3-hexylthiophene-2,5-diyl)) hole transport material as our reference experiment, which can not generate an intra-molecular electrical dipole under photoexcitation. Therefore, we will study the interfacial dipole effect on the device performance of OMHP solar cells by using respective PTB7 and P3HT as HTL. Previous study has shown that the interfacial polarizations can couple with the bulk-polarization, leading to a manipulation of photovoltaic response through charge dissociation, recombination and charge transport

[125]. An incorporation of a dipole interlayer not only enhances built-in field (V_{bi}), but also exerts a strong electrical field cross the active layer/cathode interface that may strongly influence charge transport and extraction. If the direction of this dipole moment from the transport layer is aligned with the built-in potential originated due to the asymmetric contact at the electrodes; the actual built-in potential across the device will be strengthened. It's known that the dipole aligned with built-in field can improve charge-transport properties, eliminates the buildup of space charge, and reduces recombination loss due to the increase in built-in field and charge carrier mobility [126].

In this chapter, we will systematically investigate the effect of interfacial dipole in rational design of perovskite based solar cells by using these two different organic HTLs. Furthermore, by using the observed magneto-PC combining with reversed biases, we investigated the dissociation effects in electron–hole pair states at different photoexcitation intensities to further understand charge recombination and dissociation at different densities at device-operating condition.

4.2 Experimental section

The device making procedure has been introduced in the chapter 1. The concentration of the spin-coated PTB7 and P3HT solution are both 15 mg/ml with a spin speed of 300 rpm for 60 seconds. Here, the current-voltage (*I-V*) characteristics are recorded by Keithley 2400 under a simulated sunlight (Thermal Oriel 96000 300 W from Newport). The photoluminescence spectra are recorded by SPEX Fluorolog III spectrometer with a photoexcitation of 532 nm monochromatic light. The impedance measurements are performed by using a dielectric spectrometer (Agilent E4980A; 20 *Hz* ~ 2M *Hz*) under different photoexcxitation intensities. The magneto-PC are measured by measuring the short circuit current as a function of external magnetic field.

4.3 The comparison of intrinsic properties between PTB7 and P3HT

It has previously shown that PTB7 has a relatively high hole mobility which is about $5.8*10^{-4}$ $cm^2V^{-1}s^{-1}$ measured from the space charge limited current (SCLC) and shows a strong absorption from 550-750 nm with an absorption onset of 780 nm which is also close to the absorption onset of the methyl ammonium lead iodide perovskite. Although charge carrier mobilities are comparable between PTB7 and P3HT, however,

PTB7 has shown relatively low crystallinity and an analogously amorphous film. Nevertheless, the OPV fabricated from this polymer and PCBM achieved the highest efficiency of around 10% [127]. Importantly, the biggest difference between PTB7 and P3Ht is the presence of intra-molecular dipole. As mentioned in the introduction section that the PTB7 contains both the electron-donating Benzodith-iophene (BDT) and the electron-withdrawing thienothiophene (TT) moieties (as shown in Figure 4-1). As a consequence, a photoexcitation can generate local electric dipoles between electron-donating and electron-withdrawing moieties, namely intra-molecular dipoles, in the PTB7 chains [69,87]. However, P3HT does not show this kind of characteristic under photoexcitation. Evidently it is important to emphasize the parameters, such as crytallinity and mobility, are important and influence on the performance, but the dipolar effect of PTB7 seems to be the determined parameter to show higher device performance, as a HTL, in OMHP solar cells than P3HT HTL.

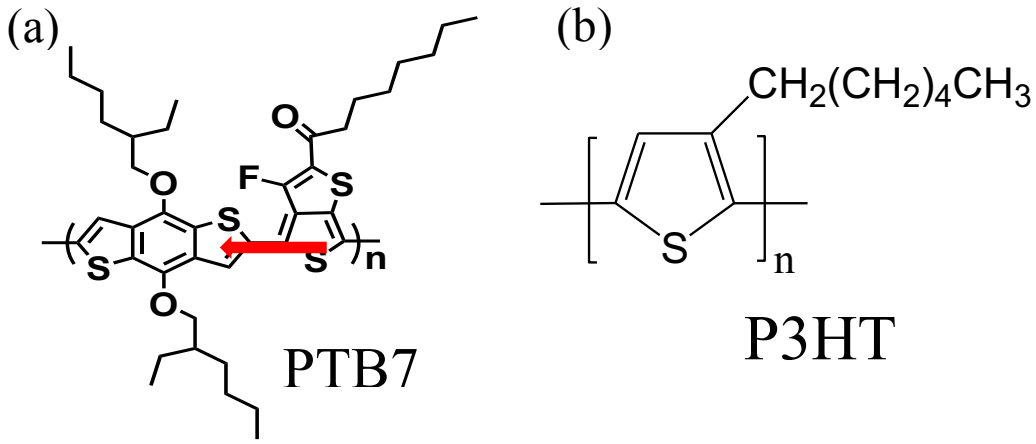

Figure 4-1. The molecular structure for (a) PTB7 and (b) P3HT. The red arrow in PTB7 is to indicate the photoexcited dipole direction.

4.4 Dipole effect of charge transport layer on interfacial and bulk properties in organo-metal halide perovskite solar cells

To explore the effects of interfacial dipole layer on device performance, we fabricated perovskite solar cells with a structure of ITO/TiO_x/$CH_3NH_3PbI_{3-x}Cl_x$/P3HT/Au. Figure 4-2 (b) illustrates the device architecture of the planar perovskite solar cells and the band energy structures of P3HT and PTB7 with respect to the other component of this design. The current–voltage (*I–V*) characteristics of the devices under AM 1.5 G irradiation with an irradiation intensity of 100 mW/cm^2 are shown in Figure 4-2 (a). As shown in Figure 4-2 (a), the device with a PTB7 film exhibits a PCE of 15.9% with a short-circuit current (*Jsc*) of 22.94 mA/ cm^2, an open circuit voltage (*Voc*) of 0.98 V, and a fill factor (*FF*) of 70%. The performances are comparable to those of perovskite solar cells using Spiro-OMeTAD [128]. On one hand, the device with P3HT as HTL shows a lower device performance (*Voc*: 0.94 V; *Jsc*: 20.5 mA/cm^2; *FF*: 56%; *PCE*: 10.8%). As mentioned above, PTB7 showed to have a relatively large local internal dipole through BDT to TT moieties. Previously Carsten et. al. has compared that the ground state and excite state dipole moment (D) of PTB7 and P3HT are 3.76, 7.13 and 0.19 and 0.43 respectively [70,73]. We observed an improvement in the performance of perovskite solar cells using PTB7 as the HTL and we attribute the higher performance to the presence of aligned dipoles in this layer. First we will demonstrate the existence of aligned dipoles in hole transport layer and then the role and responsibility of this layer on the performance.

To investigate the role of optically generated dipoles in the hole transport layer and its influence on the enhancement of charge dissociation in the perovskite layer we performed a systematic study. In order to examine the possibility that the dynamics of electrical dipole may contribute to the observed properties and behavior of perovskite solar cells and to find out the dipole alignment in the HTL we have performed a photoluminescence study on the $CH_3NH_3PbI_{3-x}Cl_x$/PTB7 and $CH_3NH_3PbI_{3-x}Cl_x$/P3HT double layers' samples under an illumination of a 532 nm continuous wavelength (CW) laser beam with a light intensity of 500 mW/cm^2. It is observed in Figure 4-3 (a) that the PL intensity of the Perovskite/PTB7 films is quenched with the increase in the electric field. This change is very negligible for Perovskite/P3HT film (shown in Figure 4-3 (b)).

It is demonstrated that the dipoles will tend to align in the external electric field. One thing need to mention that the external electrical fields we apply are all before the critical point of injection current. The purpose of these low magnitude of external electrical fields is to minimize the effect from injection current. Therefore, the PL quenching phenomenon we observed is purely from the interfacial dipole effect without any disturbance of injection current. After excluding the effect from injection current, a possible explanation for the PL quenching with application of electric field is the enhancement of charge recombination in devices using PTB7 due to a highly aligned dipoles in PTB7. The dipole alignment provides an additional channel for dissociated charge carriers' dissociation to be collected and transported towards the respective electrode. More efficient charge collection would be expected when dipoles are completely aligned under the built in potential. This measurement demonstrated that PTB7 can form dipoles which can be generated under photoexcitation in an operating situation and are aligned to some extent. Our results show that the internal dipole in the HTL may be critical and responsible for the charge transfer and enhanced performance of perovskite solar cells using PTB7.

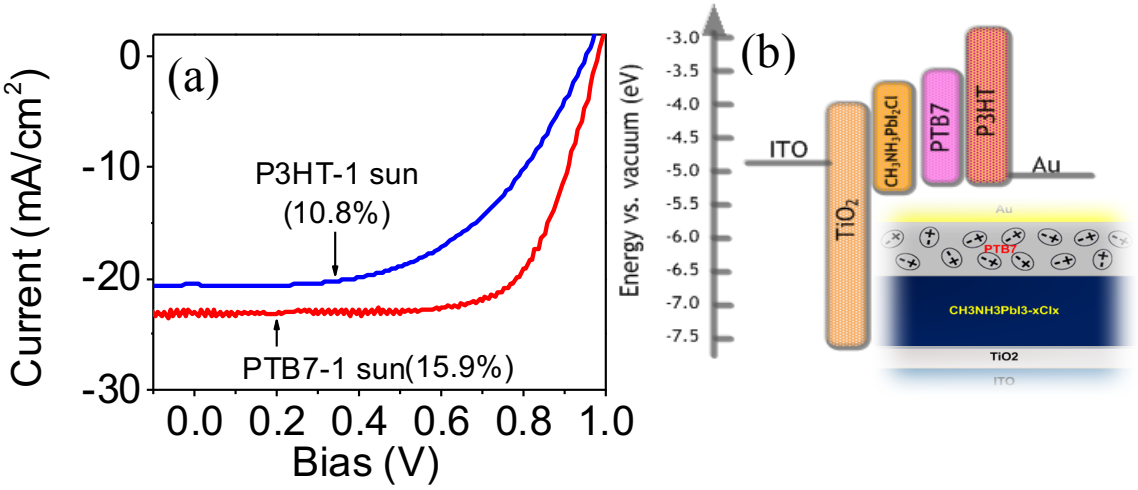

Figure 4-2. (a) *I-V* characteristics of mixed lead halide perovskite solar cell with respective PTB7 (red line) and P3HT (blue line) as hole transport layer under one sun illumination. (b) Energy level diagram and device structure of mixed halide perovskite solar cells.

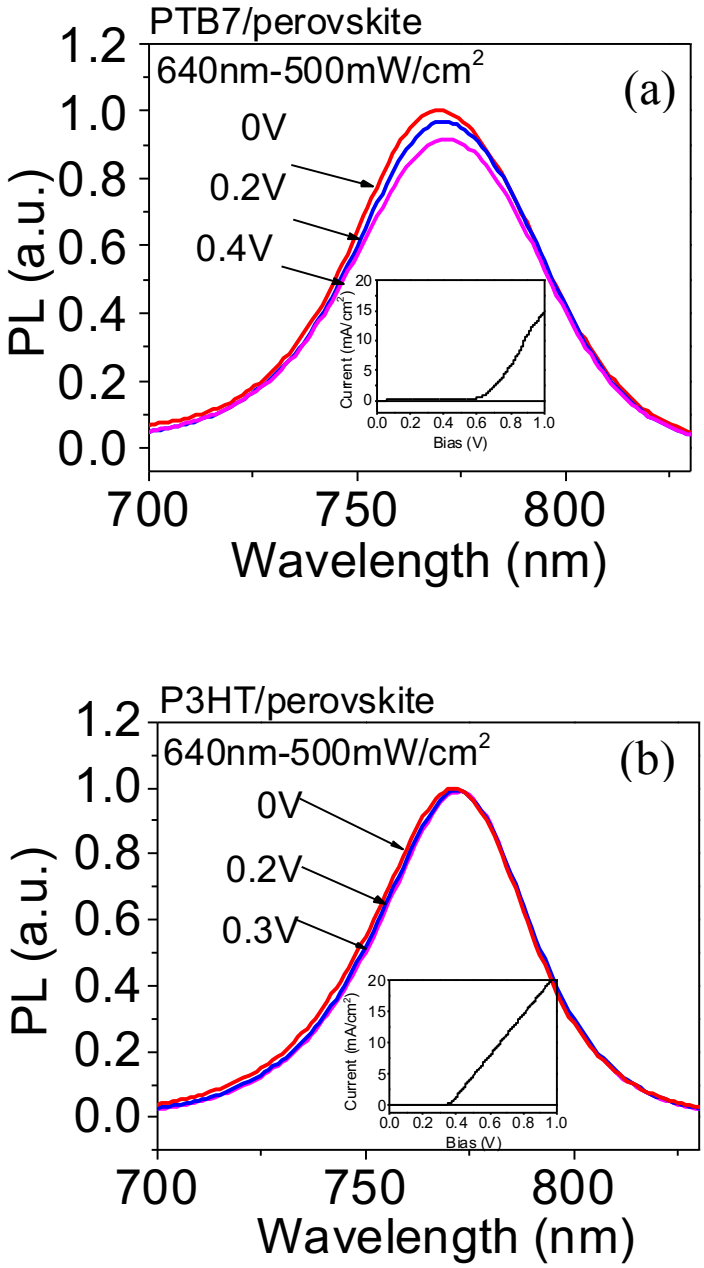

Figure 4-3. Electric field induced Photoluminescence spectroscopy of (a) perovskite/PTB7 structur and (b) perovskite/P3HT structure under illumination of continuous laser beam at 632 nm with light intensity of 500 mW/cm^2 and electrical biases. The insets show the I-V curve of the related structure and indicates that applied electric filed are before the threshold point for current injection

In order to study the effect of dipole layer in PTB7, we have deposited PTB7 and P3HT on a sandwich layer between ITO and Au and measured the capacitance versus frequency of these two different hole transport layers with increasing photoexcitation of simulated sunlight with different intensities. As it can be seen in Figure 4-5 (a) for ITO/P3HT/Au film only at low frequencies there is a small capacitance with respect to different photoexcitation intensities. This is previously shown by us to be due to the effect of interfacial charge accumulation with higher photoexcitation intensities [93,129]. For the ITO/PTB7/Au film (as shown in Figure 4-5 (b)) our capacitance-frequency (*C-f*) measurement shows two different behaviors at low and high frequencies, respectively. Low frequency region can be attributed to the polarizations at the electrode interfaces. Light illumination can increase the surface accumulation at electrode interfaces due to the higher generation of free change carriers. Similarly, in P3HT sandwich layer at low frequencies capacitance increases with higher photoexcitation intensities which is attributed to the interfacial charge accumulations. This trends shows opposite direction at higher frequencies which is capacitance reduction with increasing photoexcitation intensities. Low frequencies show interfacial charge accumulation with high excitation intensities due to higher density of charge carriers. In addition, light illumination will generate more dipoles in PTB7 (optical generated dipoles). Furthermore, the more dipole-dipole interaction in PTB7 with increasing light intensity help more charge dissociation within the bulk OMHP crystals. This results indicate that the aligned interfacial dipole from photoexcited PTB7 can provide an extra driving force to facilitate the charge dissociation within OMHP poly-crystals, and resulting in reducing the capacitance at higher frequencies with increasing photoexcitation. In general, *C-f* measurement shows that both devices demonstrate interfacial charge accumulation when the photoexcitation intensity has been increased at low frequencies. However, the bulk-polarization in OMHP active layer shows no detectable change by using P3HT as HTL when the photoexcitation increased. On the other hand, PTB7 shows the ability to manipulate the bulk-polarization within OMHP poly-crystals, and showing a detectable change of capacitance at high frequency region under photoexcitation.

(a)

(b)

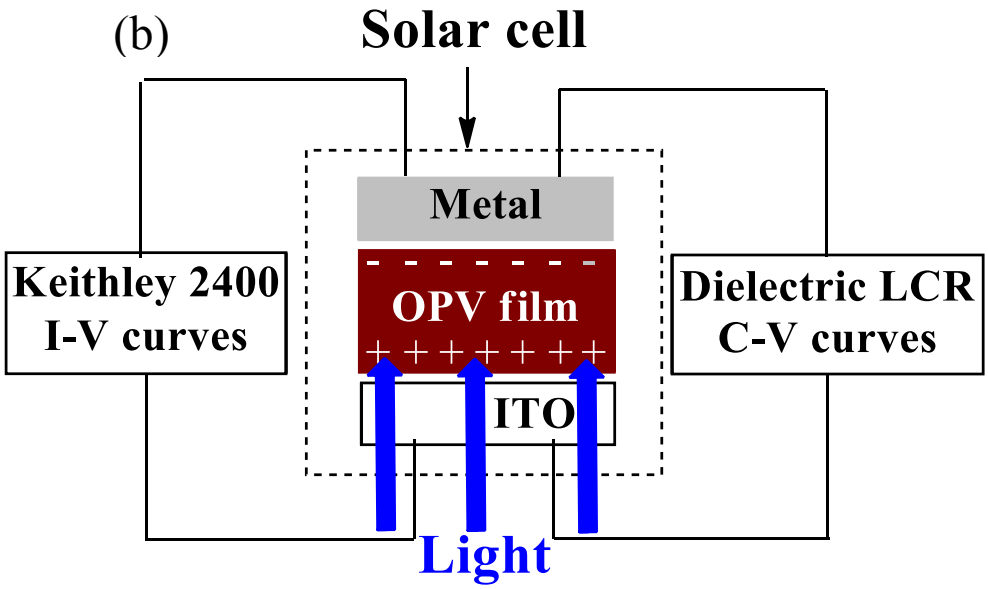

Figure 4-4. (a) The picture for the LCR meter (Agilent E4980A) and (b) capacitance measurement setup

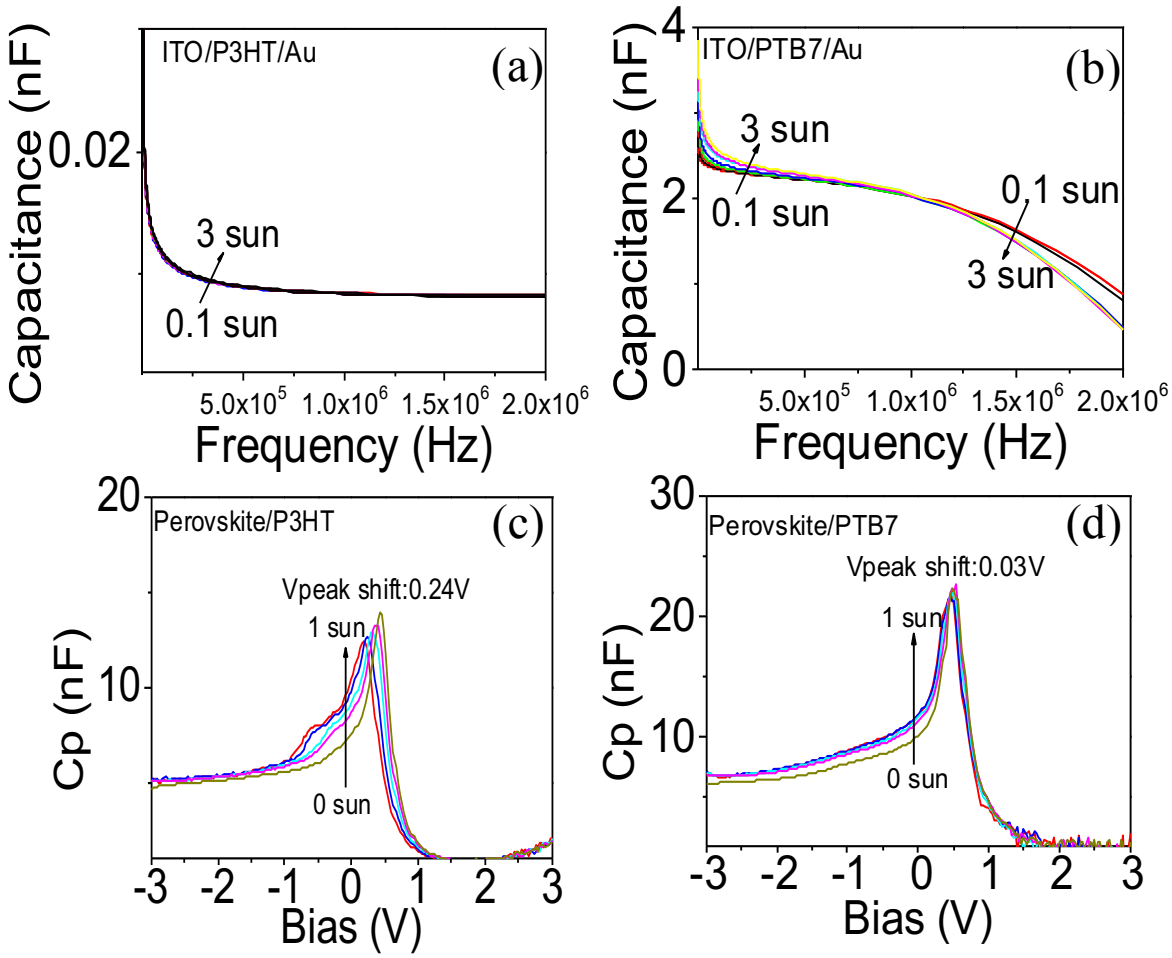

Figure 4-5. (a) and (b) Capacitance-frequency (*C-f*) measurement for P3HT and PTB7 single layer devices. (c) and (d) Capacitance-Voltage (*C-V*) measurement for double layers' devices of perovskite/P3HT and perovskite/PTB7, respectively.

For further investigation the dipole effect on the charge accumulation at interface, capacitance-voltage (*C-V*) measurements have been applied for respective Perovskite/P3HT and Perovskite/PTB7 films. This measurement usually used to reflect the interface parameters and explains the role of charge accumulations with a low frequency regime. Here, the device capacitance increases as the applied bias changed from negative to positive under different photoexcitation intensities in this two samples. It can be seen in Figure 4-5 (c) that perovskite/P3HT sample shows a larger peak shift (V_{peak} shift) as compare to the Perovskite/PTB7. One thing need to be mention here, the V_{peak} value can reflect the amount of charge accumulation at interfaces. The larger and smaller V_{peak} values correspond to less and more interfacial accumulation of photogenerated charge carriers at electrode interfaces, respectively [129]. As it is expected with higher density of photoexcitation, there will be a higher density of charge carriers, and leading to a more charge accumulation at the interfaces. Nevertheless, perovskite/PTB7 shows a clearly smaller V_{peak} shift, relatively compared to perovskite/P3HTT sample, which is related to s less charge accumulations and more charge dissociation at the interfaces due to dipole alignment in Perovskite/PTB7 film facilitating charge transport. The peak shift in Figure 4-5 (c) shows higher magnitude of charge accumulation at the interface between perovskite and P3HT in agreement with *C-f* measurements (Figure 4-5 (a)). In contrast to the perovskite/P3HT sample, this peak shift is negligible in perovskite/PTB7 which can be accredited to the less charge accumulation at the interfaces and the interfacial dipoles assisting more charge extraction in the perovskite films with PTB7. It is also observed a higher capacitance in perovskite/PTB7 sample which indicates a higher surface polarization in this sample. Therefore, the results suggest that the V_{peak} shift shown in Figure 4-5 indicates when increasing the surface polarization of a dielectric layer can lead to a decrease on the surface accumulation of photogenerated carriers towards the effective charge collection in perovskite solar cells.

In addition to the reduced charge accumulation by interfacial dipole. Here, dynamics coupling between the interfacial dipole (from PTB7) and photogenerated e-h pairs (in OMHP active layer) will be discussed. Under the influence of intrinsic electric polarization within OMHPs, the e-h pairs can be effectively dissociated into free carriers

due to their strong ionic properties and low binding energies. Previous study has shown that binding energy can be modified by local polarizations induced by built-in fields [130]. Experimental study has demonstrated that the deposition of an interfacial dipole layer can reduce the binding energies in bulk-heterojunction photovoltaic interface in OPVs [125]. In addition, it has been discussed in chapter 2 that increasing photoexcitation intensity leads to an increase on the critical bias required to completely quench the magneto-photocurrent signal in OMHP solar cells. A higher density of e-h pairs, which requires a stronger electrical field to complete the charge dissociation. Figure 4-6 shows magneto-PC under different photoexcitation intensities of 532 nm CW laser beam in a perovskite solar cells with PTB7 and P3HT films as the HTLs, respectively. In all cases with different photoexcitation intensities, the device using PTB7 as HTL has been shown to require a smaller electric field to complete the charge dissociation than the device with P3HT as HTL (as shown in Figure 4-6 (a) to (c)). Considering the fact that at higher photoexcitation intensities of laser 532 nm more e-h pairs will be generated in the OMHP active layer, therefore, a higher electric field needed to dissociate charge carriers. However, it is important to mention that under higher photoexcitation intensity that the PTB7 can generate stronger interfacial dipole as well. As a result, the required electric field observed to have a larger difference with increasing light intensities and large density of e-h pairs for the OMHP solar cells with respective PTB7 and P3HT as HTLs. Interestingly, at lower photoexcitation intensities as can be seen in Figure 4-6 (d) a negligible difference in electric field is required to dissociate charge carriers for both PTB7 and P3HT and also the overall electric field is reduced. Nevertheless, the electric field induced dipole alignment at different excitation intensities confirms that the charge dissociation is a function of carrier density in perovskites. A higher density of e-h pairs corresponds to a stronger field to complete the charge dissociation towards the generation of photocurrent in perovskite solar cells. However, in devices with perovskite/PTB7 structure this electric field reduces significantly due to the partially aligned photogenerated electrical dipoles in the hole transport layer facilitating charge dissociation and transport. Our results indicate that the interfacial dipole can reduce the electrical field required to completely initiate the signal of magneto-PC, which implies that the interfacial photogenerated dipole from PTB7 HTL can

not only reduce the charge accumulation at interface, but also reduce the binding energy of e-h pairs within OMHP solar cells. We should also note that the mutual interactions between e-h pairs as well as dipole-dipole interactions from OMHP active layer can occur when the charge density is increased upon increasing photoexcitation intensity. The mutual interactions between e-h pairs are essentially dipole–dipole interactions [120]. These mutual interactions can provide an additional mechanism to decrease the e-h binding energies for charge dissociation improvement towards generating photocurrent. Here, it could be seen that the perovskite/P3HT based solar cells shows a narrower curve of magneto-PC than the perovskite/PTB7 solar cell (shown in the inset of Figure 4-6 (a)). This is due to the interfacial dipole provided from PTB7 HTL, which can reduce the binding energy of e-h pairs, and leading to a few density of e-h pairs within perovskite active layer under device operating condition. Under this situation, the strength of the mutual interaction between e-h pairs in perovskite/PTB7 can be weaker than in perovskite/P3HT solar cell. However, at low photoexcitation intensities when the optically induced dipole in PTB7 is not sufficient, the densities of e-h pairs in respective Perovskites/PTB7 and Perovskites/P3HT solar cells are comparable (as shown in the inset of Figure 4-6 (d)). It should be noted that a photoexcitation can generate both free carriers and also partially align intermolecular dipoles in PTB7. At this point, the interaction is purely within perovskites and the role of PTB7 is to reduce the density of e-h pairs in the perovskites. Therefore, it is concluded that magneto-PC is from perovskites, not PTB7 nor P3HT. In addition, Perovskite/PTB7 solar cells show lower e-h binding energy than Perovskites/P3HT solar cell at high photoexcitaion intensities which is due to the partially aligned dipoles within PTB7. At low photoexcitation intensity, both materials needed similar reversed biases to quench the magneto-PC signal. This mean that the photogenerated interfacial dipole within PTB7 us not sufficient to undergo the coupling between interfacial dipole and e-h pairs. Moreover, the reduction in the critical bias required to quench the magneto-PC indicates that perovskite/PTB7 interface leads to a stronger built in electric field to dissociate e-h pairs compare to the perovskite/P3HT interface. This measurement provides an approach to use the optically generated dipoles in HTL to enhance charge dissociation and transport in bulk perovskite solar cells.

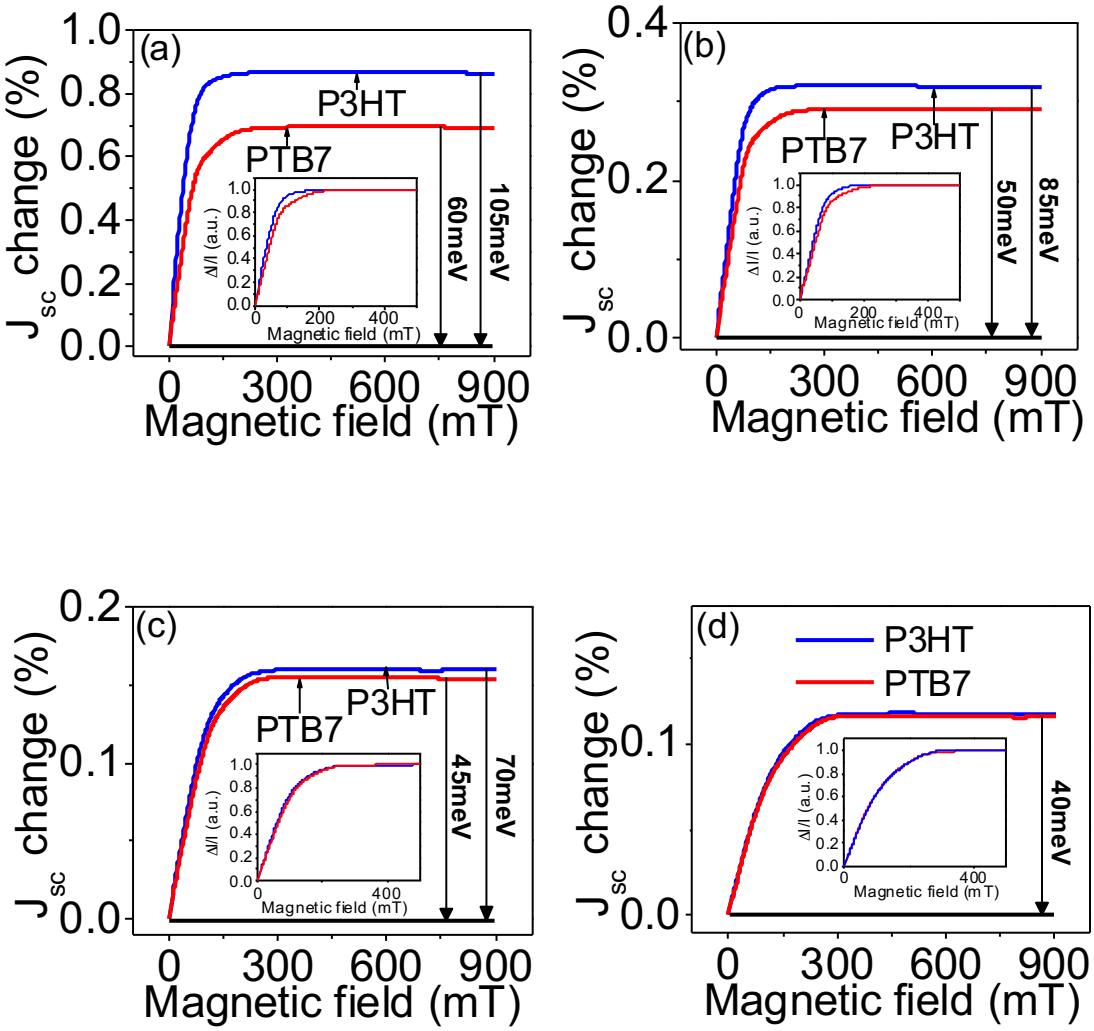

Figure 4-6. Magnetic field effect on photocurrent and electric field measurement under different photoexcitation intensities of 532nm laser beam based on mixed lead halide perovskite solar cells with respective PTB7 (red line) and P3HT (blue line) as the hole transport layer. (a) 100mW/cm^2, (b) 80mW/cm^2, (c) 30mW/cm^2, and (d) 2mW/cm^2. The insets are the normalized MFE- Photocurrent curves.

4.5 Conclusion

In this chapter, the effects of optically generated dipoles on photovoltaic actions in perovskite solar cells has been experimentally studied by using two different HTLs, PTB7 and P3HT, where optically generated dipoles are appreciable and negligible under device-operating condition. The PL quenching studies confirm that the photo-induced dipoles exist and are partly aligned in PTB7 in the direction of built-in field. The partially aligned dipoles in the transport layer can facilitate the charge dissociation and transport in OMHP solar cells and consequently enhances the performance. Meanwhile, by combining magneto-PC measurement with an external bias under different photoexcitation intensities we found that optically generated dipoles in the PTB7 transport layer can decrease the e-h binding energies in bulk perovskite layer under device operating condition. Reduced e-h binding energy can enhance the charge dissociation toward to generate higher photocurrent in perovskite solar cells. Furthermore, our capacitance measurement shows that optically generated dipoles can decrease the charge accumulation at interfaces. Therefore, our studies provide a new understanding on the effects of optically generated dipoles in transport layer on the photovoltaic processes in bulk perovskite layer, and suggest a new approach towards using optically induced dipoles for further improvement in the performance in OMHP solar cells.

Chapter 5 Revealing Free Charge Recombination Mechanism in Organo-Metal Halide Perovskite

5.1 Introduction

In 1990's the experimental studies have shown that halide perovskite compounds can exhibit EL actions in heterojunction devices at low temperatures [131,132]. The recent studies have found that OMHPs, as solution processable multifunctional materials, can demonstrate remarkable EL actions with large spectral tuning properties towards the developments of unique thin-film light-emitting devices [15,16,17133,134]. Here, we use magneto-EL as an experimental tool to explore the mono-molecular and bimolecular recombination processes in low and high-efficiency EL regimes based on the perovskite light-emitting devices with inverted structure of $Ag/MoO_3/CH_3NH_3PbI_3/TiO_x/ITO$. Furthermore, we discuss how spin-mixing affects EL efficiency in perovskite light-emitting devices. In general, OMHPs can exhibit low and high-efficiency EL at low and high injection currents [15,16 ,135]. The PL studies have shown that the low and high-efficiency light emission are generated by geminate and non-geminate recombination of the photogenerated carriers through monomolecular and bimolecular processes in OMHPs [109,110,136-138]. Obviously, increasing injection current can shift the EL from low to high-efficiency regime in OMHPs. On the other hand, field-dependent PL and EL have been observed, leading to magneto-PL and magneto-EL at room temperature and low field (< 200 mT) [40,41]. Essentially, magneto-PL and magneto-EL provide an experimental tool to probe whether spin-mixing is operative during the generation of light emission. Specifically, the observed magnetic field effects indicate that spin-mixing occurs between different spin states. In particular, an applied magnetic field can modify spin-mixing process and consequently shifts spin populations between different states, leading to a field-dependent light emission. Therefore, magnetic field effects can also elucidate spin-mixing between different spin states during light emission.

The PL studies have shown that the recombination between electrons and holes undergoes monomolecular and bimolecular processes at low and high intensities [136-138]. In particular, monomolecular and bimolecular recombination are often associated with low and high emission efficiencies, leading to a non-linear relationship between light

emission and excitation intensities [19,109,110]. Essentially, monomolecular and bimolecular recombination at low and high excitation intensities occur with un-balanced and balanced electron and hole densities, respectively. With un-balanced electron and hole densities, monomolecular recombination is driven by minority carriers through Coulomb capture. On contrast, with balanced electron and hole densities, bimolecular recombination is governed by both electron and hole densities when they meet within Coulomb capture radius. Based on spin statistics the electron-hole recombination yields 25% antiparallel spin pairs and 75% parallel spin pairs, leading to the 1:3 branching ratio of antiparallel/parallel spin pairs in both monomolecular and bimolecular processes. This branching ratio forms theoretical limit for quantum efficiencies in EL when only antiparallel spin pairs are allowed to generate an EL due to Pauli Exclusion Principle. It should be noted that spin-mixing can function as a useful mechanism to vary the 1:3 branching ratio of antiparallel/parallel spin pairs, generating a possibility to enhance EL efficiencies. In this chapter, we combine EL with magneto-EL to elucidate the free charge recombination processes within OMHP, and meanwhile to revealing the spin-mixing in low and high-efficiency regimes associated with monomolecular and bimolecular recombination in perovskite light-emitting devices.

5.2 Experimental section

The detail for the OMHP light emitting diode making procedure has been in traduced in chapter 1. The surface topography is measured by Veeco Instruments atomic force scanning probe microscope (AFM). The AFM tips are standard Veeco 0.01–0.025 Ωcm Antimony (n) doped Si tip. The current-voltage (*I-V*) characteristics were measured by using Keithley 2400 source meter. The EL and PL were recorded by SPEX Fluorolog 3 spectrometer. The EL brightness was estimated by comparing with calibrated inorganic light-emitting diodes. The photoexcitation source for PL is 532nm continuous wave laser. Magnetic field effects (MFE) refer to the phenomena in which electrical or optical signal changes as a function of an external magnetic field. The amplitude for magneto-EL and magneto-PL is given by the relative change in percentage: $MFE = \frac{I_B - I_0}{I_0}$, where I_B and I_0 are the signal intensities with and without an applied magnetic field. All materials

processing and experimental measurements were performed under nitrogen atmosphere at room temperature.

5.3 High and low electroluminescence regimes from respective bimolecular recombination and mono-molecular recombination processes

Figure 5-1 (a) shows the EL characteristics in the inverted $Ag/MoO_3/CH_3NH_3PbI_3/TiO_x/ITO$ device at forward bias (Ag-positive and ITO-negative) while no detectable EL actions can be observed at reverse bias. The EL spectrum is consistent with photoluminescence (PL) spectrum, indicating an intrinsic EL action from OMHP ($CH_3NH_3PbI_3$) (Figure 5-1 (b)). The EL brightness was estimated to be 700 cd/m^2 at the forward current density of 450 mA/cm^2. Figure 5-1 (c) and (d) show the experimental results from x-ray diffraction (XRD) and the atomic force microscope (AFM) measurements. The XRD result shows high crystallinity in the polycrystalline domains in our perovskite samples. The AFM image indicates high-quality perovskite films.

Figure 5-2 (a) shows EL intensity as a function of injection current. The EL is nonlinearly increasing with injection current, leading to low and high-efficiency EL regimes below and above the critical current of 220 mA/cm^2. It should be noted that a nonlinear relationship between PL and excitation intensities can be also observed in OMHP ($CH_3NH_3PbI_3$) (as shown in Figure 5-2 (b)). Similarly, the PL can be divided into low and high-efficiency regimes below and above the critical photoexcitation of 210 mW/cm^2. The PL studies have shown that a photoexcitation generates a large amount free electrons and holes within the time scale of picoseconds due to low electron-hole binding energies [19]. Consequently, the PL is essentially generated by the recombination of photogenerated electrons and holes in OMHP. This leads to a scenario that the EL and PL share the same underlying mechanism to generate electron-hole recombination towards light emission. The early publications have shown that the recombination of photogenerated electrons and holes undergoes monomolecular and bimolecular processes at low and high-efficiency regimes [109,110]. Based on the fact that the EL and PL exhibit similar nonlinear relationship with excitation intensity, we can suggest that the respective low and high-

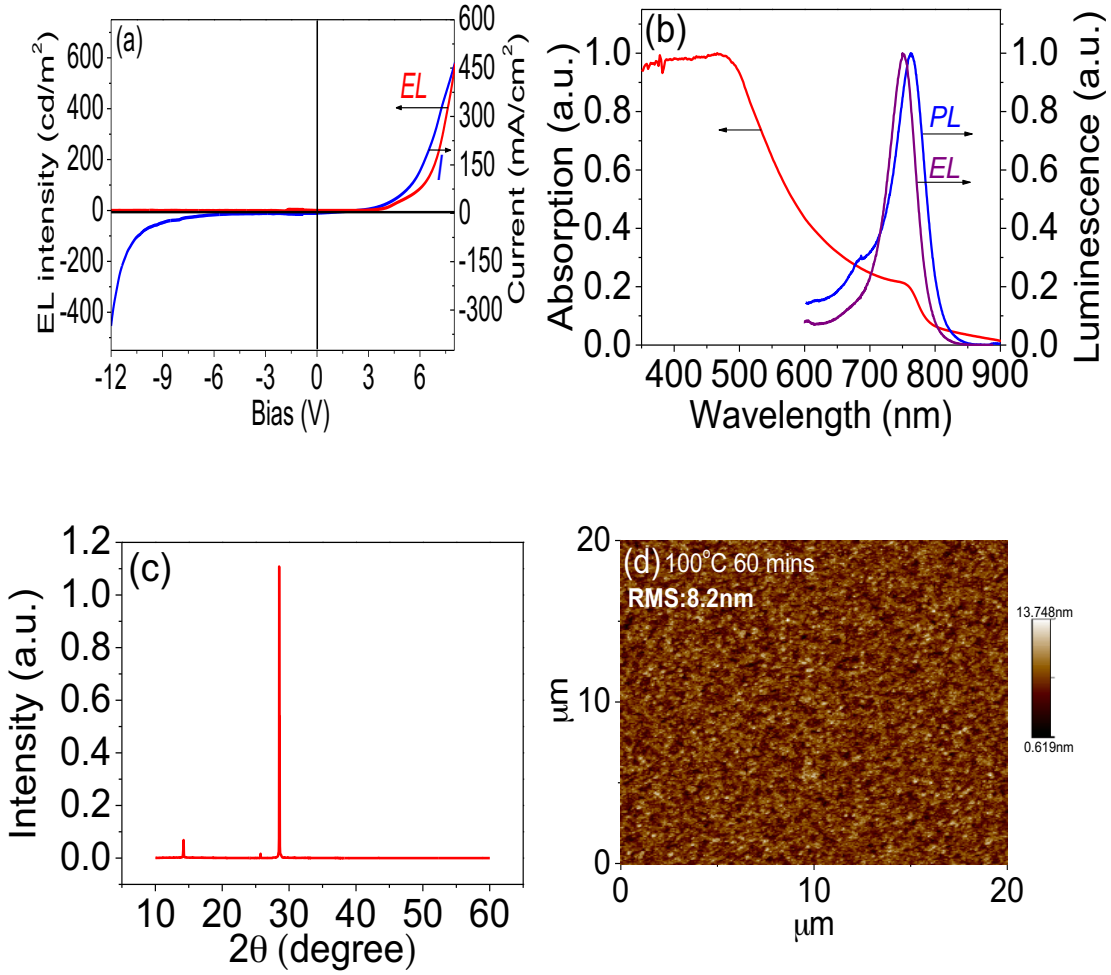

Figure 5-1. Forward bias: Ag-positive and ITO-negative. Reverse bias: Ag-negative and ITO-positive. (a) Current-voltage-EL characteristics at both forward and reverse biases in $Ag/MoO_3/CH_3NH_3PbI_3/TiO_x/ITO$ device. (b) Absorption, photoluminescence, and electroluminescence spectra for organo-metal halide halide perovskite thin film. (c) X-ray diffraction (XRD) spectra for organo-metal halide perovskite thin film. (d) Atomic force microscope (AFM) image to show the morphology for organo-metal halide halide perovskite thin film.

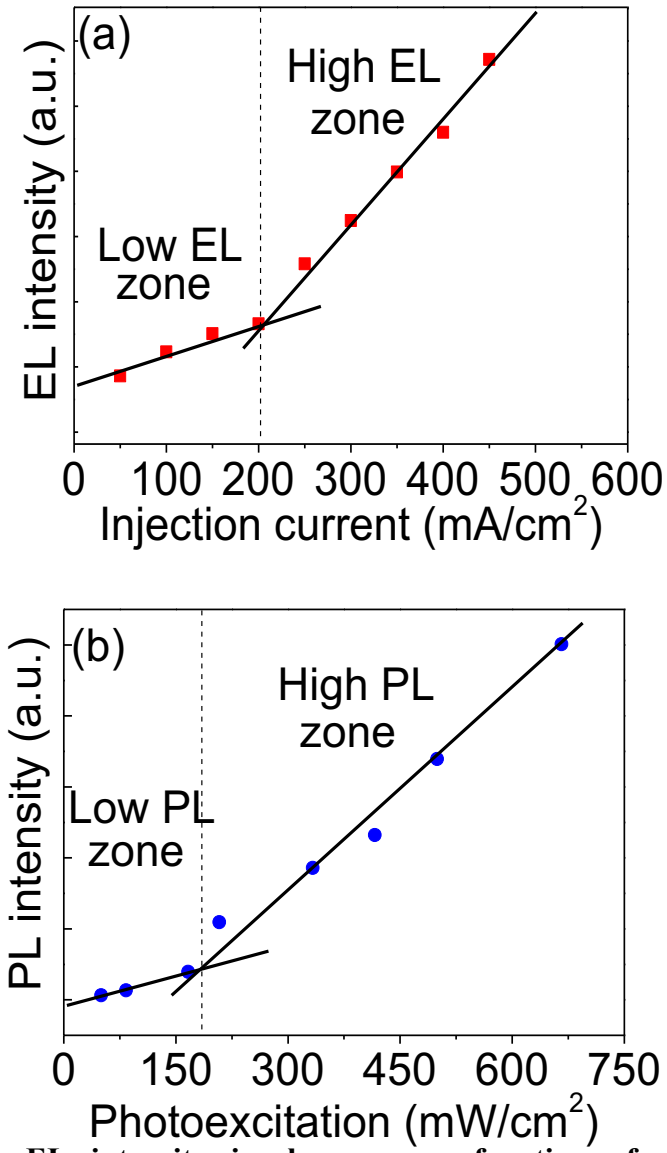

Figure 5-2. (a) EL intensity is shown as a function of current density in Ag/MoO_3/$CH_3NH_3PbI_3$/TiO_x/ITO device at forward bias (Ag-positive and ITO-negative). (b) PL intensity is shown as a function of photoexcitation intensity in $CH_3NH_3PbI_3$ thin film under 532 nm CW laser illumination.

efficiency EL regimes are from monomolecular and bimolecular recombination in the perovskite light-emitting devices [Ag/MoO_3/$CH_3NH_3PbI_3$/TiO_x/ITO].

In general, the monomolecular and bimolecular recombination can be related to un-balanced and balanced electron and hole densities in carrier capture, respectively. Specifically, when the electron and hole densities are un-balanced, the recombination probability is governed by the capture of minority carriers, leading to a monomolecular process. When the electron and hole densities are balanced, the recombination probability is dominated both electrons and holes through bimolecular capture, generating a bimolecular behavior. In general, polycrystalline perovskites possess ions and defects which form traps for electrons and holes. The experimental measurements on Seebeck effect indicate that the OMHP: $CH_3NH_3PbI_3$ is a p-type semiconductor [139]. The PL studies have suggested that at low photoexcitation intensity the photogenerated carriers can gradually occupy traps and consequently leads to a low-efficiency light emission [109,110]. This low-efficiency PL regime essentially results from monomolecular recombination. On contrast, at high photoexcitation intensity the traps become fully occupied, the photogenerated electrons and holes undergo a bimolecular recombination with high-efficiency PL [109,110]. In EL, we can expect a similar situation, monomolecular and bimolecular recombination at low and high injection, respectively. This gives rise to low and high-efficiency EL regimes as injection current is increased.

5.4 Exploring spin mixing at low and high-efficiency EL regimes by using magneto-EL measurements.

Previous studies have shown that an external magnetic field can change the branching ratio between antiparallel and parallel spins by disturbing the spin mixing generated by spin-orbital coupling, leading to magneto-PL and magneto-EL. This has been found to be primary mechanisms to generate magnetic field effects on light emission in organic semiconductors [140,141]. Therefore, magneto-EL can be used as an experimental tool to explore spin mixing in monomolecular and bimolecular recombination in OMHP light-emitting devices. We can see in Figure 5-3 (a) that the EL measured below and above forward injection current of 190 mA/cm^2 yield negligible and appreciable magneto-EL signals. Interestingly, the low and high-efficiency EL regimes show negligible and

appreciable magneto-EL, respectively. Because the low and high efficiency EL occur in monomolecular and bimolecular recombination, we can see that the monomolecular and bimolecular recombination give rise to negligible and appreciable magneto-EL. Essentially, the negligible and appreciable magneto-EL suggest that the spin mixing becomes in-operative and operative in monomolecular and bimolecular recombination. The monomolecular recombination occurs through the charge capture in traps. The in-operative spin mixing means that the monomolecular recombination is a short-distance capture within traps. A short-distance capture forms a strong exchange interaction, dis-allowing the spin mixing between antiparallel and parallel spin pairs. In statistics the charge capture yields 25 % antiparallel spin pairs and 75 % parallel spin pairs. In this situation, the light-emitting states are essentially formed with the upper limit of 25% branching ratio at monomolecular recombination through charge capture occurring in traps due to in-operative spin mixing. This gives rise to a low-efficiency EL in monomolecular recombination. On contrast, the operative spin mixing suggests that the bimolecular recombination is a long-distance capture at high injection current after the traps are filled. A long-distance capture corresponds to a weaker exchange interaction, allowing spin mixing between antiparallel and parallel spin pairs. In this situation, the light-emitting states can be formed with more than 25 % branching ratio due to operative spin mixing, leading to a high-efficiency EL in bimolecular recombination. Therefore, spin mixing forms a useful mechanism to enhance the EL in OMHP light-emitting devices by switching the charge capture from monomolecular to bimolecular recombination.

Here, we use magneto-PL as an effective tool to further confirm the in-operative and operative spin mixing at monomolecular and bimolecular recombination. The PL consists of two subsequent processes: (i) a photoexcitation generates a large amount of free electrons and holes in OMHPs due to low binding energies and fast dissociation [19,36 ,142] and (ii) the photogenerated free electrons and holes recombine into light-emitting states. Therefore, magneto-PL provides an analogous opportunity to explore spin mixing in different recombination regimes in the OMHPs as photoexcitation intensity is increased. We can see in Figure 5-3 (b) that the PL shows negligible and appreciable magnetic field effects below and above the critical excitation intensity of 150 mW/cm^2, very similar to

the phenomena observed in magneto-EL. Above this critical excitation intensity a negative magneto-PL can be observed. Below this critical intensity no magneto-PL can be detected although a strong PL still exists. By comparing with PL-excitation dependence in Figure 5-2 (b), we can see that the low and high-efficiency PL correspond to negligible and appreciable magneto-PL through monomolecular and bimolecular recombination of photogenerated carriers, an analogue phenomenon to EL. In addition, the magneto-PL and magneto-EL (Figure 5-3 (b)) and (Figure 5-3 (a)) have common Lorentzian line-shape characteristics ($\Delta I(B)/I \propto [B^2/(B^2+B_0^2)]$). As a result, the magneto-PL results can confirm the conclusion made from magneto-EL: the monomolecular and bimolecular recombination show in-operative and operative spin mixing, respectively, in the OMHPs. For further confirm the relationship between spin exchange interaction and spin mixing under a high injection density, we verify the free charge recombination process after the dismissed shallow trap states and, especially, under a high injection current. It could be seen in Figure 5-4 that the magnitude of magneto-EL demonstrates an initial increasing before the critical injection current density of 750 mA/cm^2. However, when the injection current density is keeping increased that we can see a decrement of magneto-EL response from OMHP light emitting diode. Based on the fact that the higher density of free charge carriers can lead to form a e-h pair with strong spin exchange interaction. Under this situation, the e-h pair with strong spin exchange interaction will lead to a weak operative spin-mixing under external magnetic field.

In general, the spin mixing can lead to a change of the ratio of spin states, which can be caused by hyperfine coupling [117,118] and Δg mechanism [84,86]. From our negative magneto-EL and magneto-PL, it suggests that the spin mixing direction within our OMHP light emitting diode is from spin parallel state to spin anti-parallel state. Therefore, under an external magnetic field that the spin mixing processes will be suppressed, and leading to a more population of spin-parallel state, which is the origin of negative magneto-PL and magneto-EL. Therefore, under the device operation condition without external magnetic filed that the spin mixing is expeted to be happened, which can convert more parallel spin pairs to antiparallel spin pairs, leading to a higher population of spin-parallel e-h pairs to break spin-parallel states:spin-antiparallel states=25%:75% branching ratio.

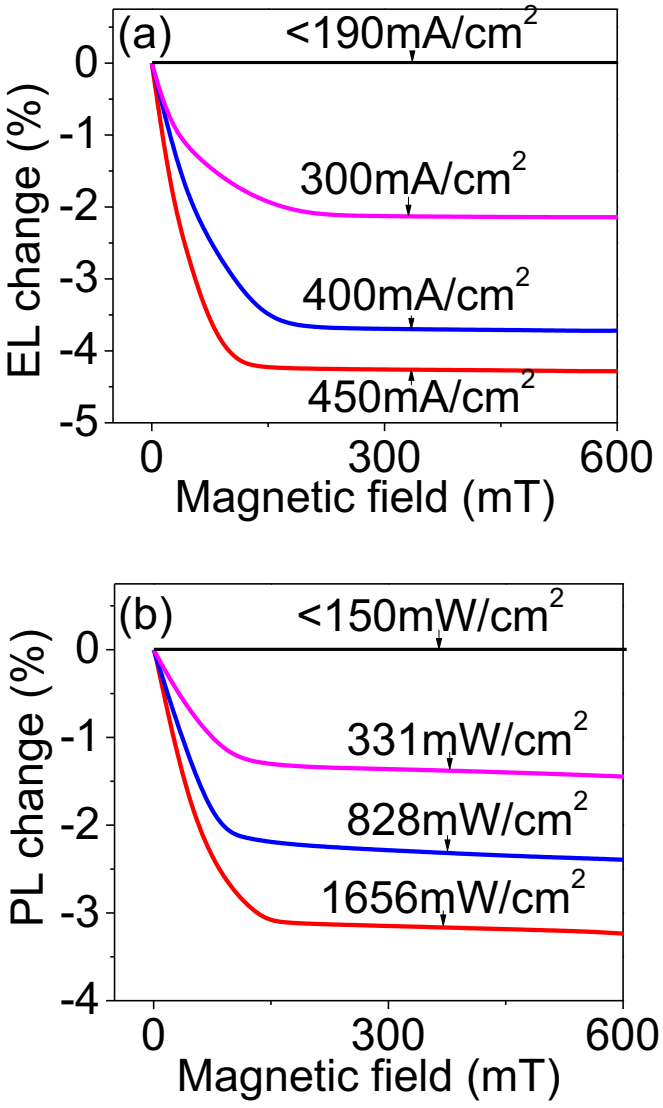

Figure 5-3. (a) Magneto-EL measured at different injection currents from Ag/MoO_3/$CH_3NH_3PbI_3$/TiO_x/ITO device at forward bias (Ag-positive and ITO-negative). (b) Magneto-PL measured at different excitation intensities.

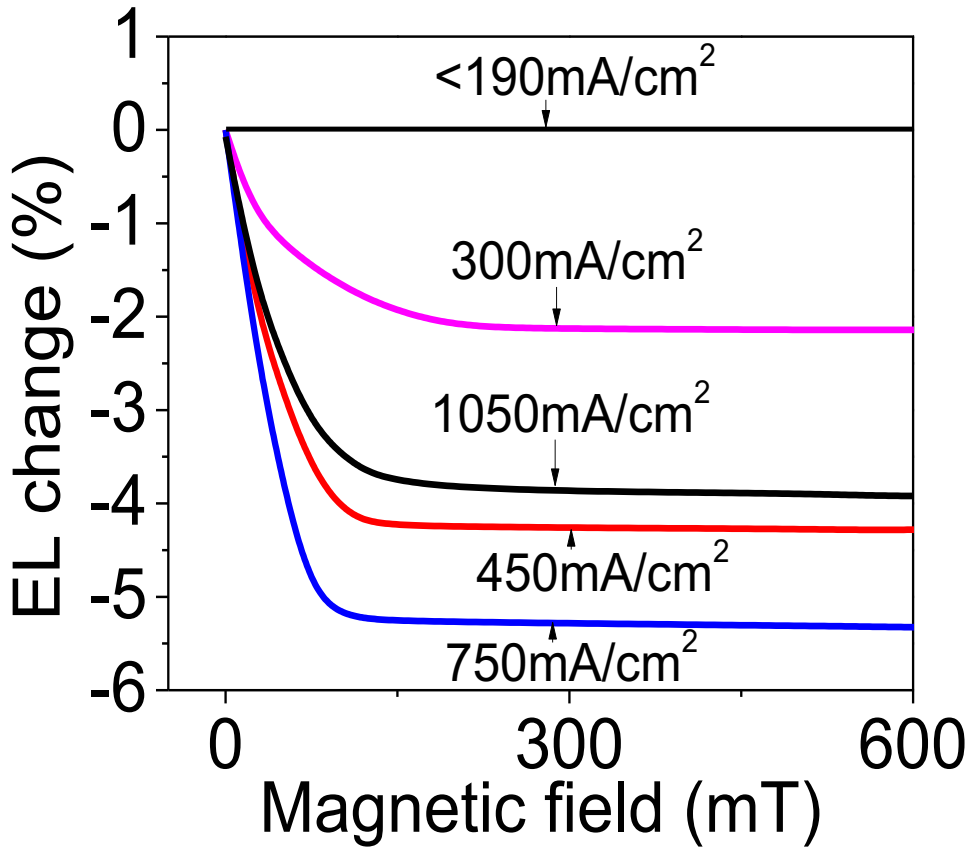

Figure 5-4. Magneto-EL measured under high injection current (above 750 Ma/cm^2) from Ag/MoO_3/$CH_3NH_3PbI_3$/TiO_x/ITO device at forward bias (Ag-positive and ITO-negative).

Under high luminescence regime, a magnetic field can change the populations of different spin states in electron-hole pairs by suppressing the internal spin mixing through inducing coherent spin precessions. Specifically, the spin mixing can shift the population between spin-antiparallel and spin-parallel states with the direction from high energy to low energy. Essentially, spin mixing requires both spin and energy conservations between different spin states. The spin conservation can be satisfied by spin-orbital coupling (SOC) in OMHPs. On one hand, the energy conservation can be conveniently realized by thermal energy. In particular, the spin conservation determines whether the spin-mixing can occur while the energy conservation controls the spin-mixing direction. When the spin-parallel pairs are higher than spin-antiparallel pairs in the situation of negative exchange energy, the spin mixing shifts the electron-hole pairs from spin-parallel states to spin-antiparallel states, namely parallel-to-antiparallel spin mixing. However, when the spin-antiparallel pairs are higher than spin-parallel pairs in the situation of positive exchange energy, the spin mixing shifts the electron-hole pairs from spin-antiparallel states to spin-parallel states, namely antiparallel-to-parallel spin mixing. These two situations can lead to negative and positive magnetic field effects when an applied magnetic field suppresses the spin-mixing behavior by introducing coherent spin precessions. The early studies have shown that the spin-parallel states normally have higher energies than spin-antiparallel states in electron-hole pairs due to negative exchange energy [143,144]. Therefore, suppressing spin-mixing can generate a negative magneto-EL under charge injection. On the other hand, we should note that an applied magnetic field can also introduce in-coherent spin precessions through Δg and field-gradient effects where the electron and hole experience different field strengths at different locations within an e-h pair [145]. In this situation, we can expect magnetic field effects generated by enhancing spin-mixing behavior between different spin states. Considering the fact that spin-parallel states can normally have higher energy than the spin-antiparallel states in electron-hole pairs with the parallel-to-antiparallel spin mixing, enhancing spin-mixing can then lead to a positive magneto-EL. Our results indicate that suppressing spin-mixing is a dominant mechanism to generate magneto-EL in the OMHP light emitting Ag/MoO_3/$CH_3NH_3PbI_3$/TiOx/ITO device (as shown in Figure 5-3).

However, under low luminescence regime that no detectable magnetic field effects can be observed. Here arises an open question: Does the negligible magnetic field effects in OMHP come from either strong exchange energy or extremely strong spin-mixing between e-h pairs? In general, both mechanisms can theoretically contribute to negligible magnetic field effects. Figure 5-2 shows both EL and PL intensities as a function of current density and photoexcitation intensity. We can see that both EL and PL shows a non-linearly increasing behavior. Clearly, the EL and PL actions can be divided into low and high efficiency zones below and above the injection current of 217 mA/cm^2 and photoexcitation of 210 mW/cm^2, respectively. The EL-current and PL-photoexcitation characteristics can essentially reflect the quantum efficiencies: smaller and larger slopes give rise to low and high carrier recombination efficiencies. On the other hand, it should be noted from magneto-EL and magneto-PL results that the EL and PL can be divided into monomolecular and bimolecular recombination regimes below and above the critical excitation intensity of 190 mA/cm^2 for magneto-EL and 150 mW/cm^2 for magneto-PL. As discussed above, due to the existence of trap states in low luminescence regimes that the monomolecular recombined e-h pairs can show a strong binding energy and short separation distance. Under this situation, the spin exchange energy between e-h pairs can be very strong, and leading to a scenario of strong spin-conserving between spin anti-parallel state (singlet) and spin parallel state (triplet). As a result, the ratio between singlet e-h pairs and triplet e-h pairs is limited to 25%:75% in OMHP crystals. As a consequence, based on the experimental results we suggest that the origin of the negligible magnetic field effects demonstrated in low luminescence regime is due to the absence of spin-mixing, which is caused by the strong spin exchange energy of e-h pairs (ash shown in Figure 5-5).

5.5 Conclusion

In this chapter, perovskite LEDs have been fabricated based on the inverted design: $Ag/MoO_3/CH_3NH_3PbI_3/TiO_x/ITO$. The results have shown that the EL shows magnetic field-independent and magnetic field-dependent recombination regimes at low and high charge densities below and above 190 mA/cm^2, respectively. In the field-independent recombination regime at low charge densities, the charge recombination happens through

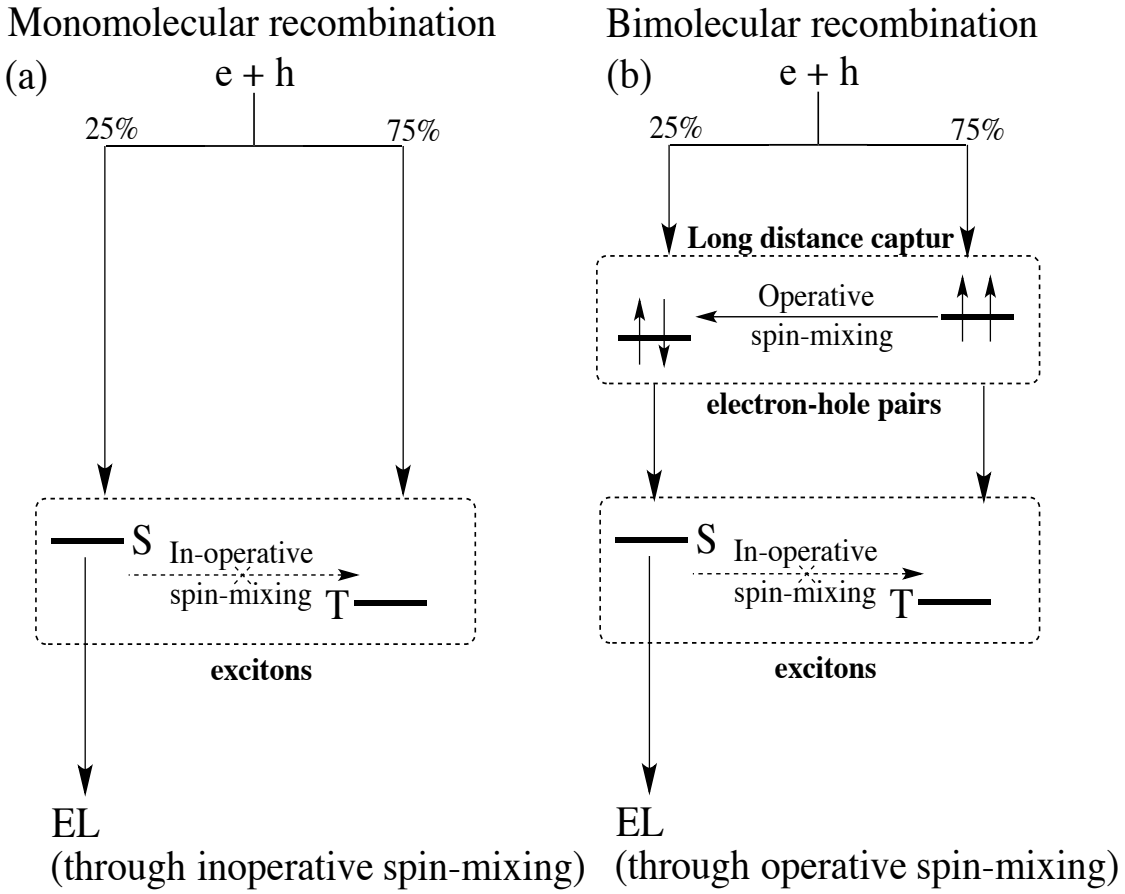

Figure 5-5. The in-operative spin-mixing does not provide a mechanism to operate the parallel-to-antiparallel transition in short distance light emitting states formed through field-independent pairing process (a). The operative spin-mixing facilitates the parallel-to-antiparallel transition in electron-hole pairs formed through field-dependent pairing process and consequently increases light-emitting states: higher EL efficiency (b).

monomolecular recombination process due to the existence of shallow trap states within OMHP crystals. Consequently, the monomolecular recombined e-h pairs show a strong spin exchange energy, leading to an absence of spin-mixing. In this situation, an external magnetic field can not change the spin antiparallel to spin parallel ratio due to negligible spin-mixing of monomolecular recombined e-h pairs. On the other hand, in the field-dependent recombination regime at high charge densities, due to the filled shallow trap state by high density of free charge carriers within OMHP crystals that the dominant charge recombination process can be transferred from monomolecular recombination regime to bimolecular recombination regime. In this situation, the bimolecular recombined e-h pairs show a weak spin exchange interaction, leading to an appreciable spin-mixing from bimolecular recombined e-h pairs. Consequently, an external magnetic field can change the spin antiparallel to spin parallel ratio by disturbing the spin-mixing process of bimolecular recombined e-h pairs. Our results indicate that an applied magnetic field can suppress the parallel-to-antiparallel spin-mixing generated by SOC, leading to a negative magneto-EL. Nevertheless, our studies show that the carrier recombination can be divided into field-independent and field-dependent regimes in EL operation with negligible and appreciable magneto-EL. Furthermore, we observe that the EL shows low and high increasing rates with increasing injection current below and above 217 mA/cm^2 in the $Ag/MoO_3/CH_3NH_3PbI_3/TiO_x/ITO$ device. This indicates that the light-emitting e-h pairs are formed with low and high rates in monomolecular recombination paring and bimolecular recombination paring regimes to generate EL actions in OMHPs.

Chapter 6 Spectral Narrowing Phenomenon in Perovskite Light Emitting Devices Induced by Linearly Polarized Photoexcitation

6.1 Introduction

Recently, the light emitting property from OMHPs has attracted a lot of attention due to its color tunable and high efficiency characteristics [134]. Especially, lasing action from OMHP materials is an important discovery to broader the application of OMHP materials. First lasing action from OMHP has been discovered by F. Deschler *et al.* from Cavendish Laboratory. They found that the OMHP materials can generate a strong lasing under a strong photoexcitation intensity and with a cavity structure [19]. Recently, the phonon bottle effect has been found in OMHPs, which may be the primary mechanism leads to the lasing action in OMHPs [146]. Up to date, the lasing action from OMHPs can only be generated from an extremely high power of photoexcitation. No experimental result shows the lasing action from electrical excitation. The key reason for the difficulty of generating the lasing action by pure electrical excitation is due to that a significant heat produced from high current injection, which can cause a device decay in OMHPs light emitting devices. In general, the EL actions result from three consecutive processes, (i) electrically injecting electrons and holes with balanced densities, (ii) spatially confining electrons and holes for forming light-emitting excitons, and (iii) radiative emission of light-emitting excitons in perovskite light-emitting diodes. Recently, the EL efficiency has been largely increased by simultaneously improving the charge injection and confinement [138]. The remarkable EL actions not only provide the promising potential for developing highly-efficient thin-film light-emitting devices, but also present the possible platform to explore the underlying mechanism for amplifying EL actions. An interesting PL phenomenon is noted: the quantum efficiency shows low values at low fluences but very high values at high fluences. The PL quantum yield can be as high as 70 % in the perovskite films at room temperature [138]. This rapidly increasing quantum efficiency with excitation intensity provides the precondition to realize lasing actions in OMHPs. As an exemplified progress, the optically pumped lasing actions have been successfully demonstrated with wavelength-tuning ability through amplified spontaneous emission (ASE) or stimulated emission (SE).

The optically pumped lasing actions together with remarkable EL actions presents high promises for developing electrically pumped lasing actions in perovskite thin-film devices. In this chapter, a possible mechanism has been explored to optically amplify the EL in perovskite light-emitting diodes [Ag/MoO_3/$CH_3NH_3PbBr_3$/PEIE/TiO_x/ITO] by combining electrical and optical excitations. We observe that the light emission from the Ag/MoO_3/$CH_3NH_3PbBr_3$/PEIE/TiO_x/ITO device shows a large spectral narrowing phenomenon induced by a linearly polarized incident light. The experimental studies suggest that optically induced amplification and alignment of electrically generated light-emitting excitons function as the underlying mechanism responsible for spectral narrowing phenomenon with linear polarization characteristics in the perovskite light-emitting diodes.

6.2 Experimental Section

The detail for the OMHP light emitting diode making procedure has been in traduced in chapter 1. First, a electron transport layer, PEIE (polyethylenimine), has been spin casted on top of ITO/TiOx layer. Secondly, the bromine OMHP active layer was prepared by mixing Methylammonium bromide (MABr) and lead bromide ($PbBr_2$) in anhydrous dimethylformamide (DMF, Aldrich) with a mole ration of 1:1. The overall solution concentration was 30 wt%. The bromine perovskite precursor was then stirred for 2 hours at 60℃ and followed by filtration with a 0.45μm PVDF filter. The bromine OMHP ($CH_3NH_3PbBr_3$) solution was spin-cast with the film thickness of 50 nm on the ITO/TiOx/PEIE substrates, followed by thermal annealing at 90℃ for 10 minutes. The current-voltage (*I-V*) characteristics were measured by using Keithley. The photoexcitation source for PL is linearly polarized 405 nm continuous wave (CW) laser. The impedance measurements (*C-f*) are performed by using a dielectric spectrometer (Agilent E4980A; 20 *Hz* ~ 2M *Hz*) under different magnitudes of excitation intensity to measure the polarization within our bromide perovskite light emitting diode under different regimes (low frequency regime: interfacial polarization; high frequency regime: bulk polarization regime). Polarization emission measurement set up by putting a polarizer after the bromine perovskite sample under a photoexcitation of linear polarized 405 nm CW laser (as shown in Figure 6-1 (a)).

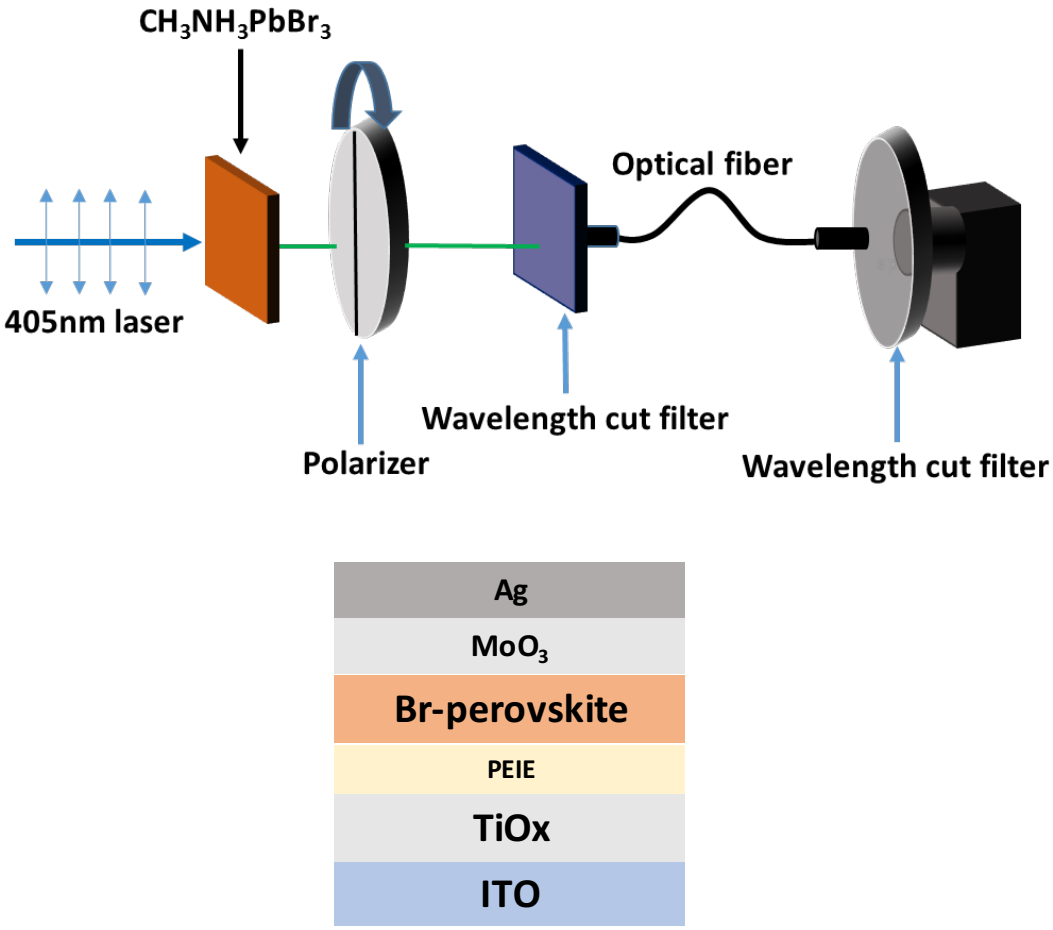

Figure 6-1. (a) Experimental setup and (b) device structure for the linear polarized light detection for bromine based light emitting diode.

6.3 Results and discussion

Figure 6-2 (a) and Figure 6-2 (b) shows the luminescence spectra and magnitudes of $CH_3NH_3PbBr_3$ samples from different photoexcitation intensities under a simultaneously applied electrical excitation and photoexcitation. It worth to note that the narrowest full width and half maximum (FWHM) of the luminescence spectrum is around only 9.5 nm under a high current density of 1375 mA/cm^2. More importantly, the FWHM of light emission is reduced from 36 nm to 9.5 nm, by a factor of 3.8, operated at the constant bias of 9 V concurrently when the power of the linearly polarized 405 nm CW beam changes from 450 mW/cm^2 to 950 mW/cm^2. In order to clarify the effect from the density of excited states in the spectrum narrowing phenomenon, here we measure the magnitude change of linear polarization of emissive light from $CH_3NH_3PbBr_3$ samples under the simultaneously applied electrical excitation and photoexcitation with different excitation intensities (the experimental setup is shown in Figure 6-1 (a)). It could be seen in Figure 6-2 (c) that when the excitation intensity of simultaneously applied electrical excitation and photoexcitation is increased from 279 mA/cm^2 to 1081 mA/cm^2, the magnitude change of polarized light emission is also changed from 5% (red curve) to 20% (dark yellow curve). Here, the results shown in Figure 1 hint that the high density of excited states generated by excitation plays an important role in the demonstration of luminescence spectrum narrowing phenomenon.

In order to study the role of simultaneously applied electrical excitation and photoexcitation in the luminescence spectrum narrowing phenomenon, here we measure the current density-bias (*J-V*) curve. Figure 6-3 (a) shows *J-V* curves from respective pure electrical injection under dark condition, pure photo-current under illumination intensity of 950 mW/cm^2 from a 405 nm CW laser, and simultaneously applied electrical injection and photoexcitation. Here, it could be seen clearly that the simultaneously applied electrical injection and photoexcitation shows a higher magnitude of current density (~1350 mA/cm^2) than the dark injection current (~275 mA/cm^2) and photocurrent (~65 mA/cm^2). Furthermore, even the sum-up of dark injection current and photocurrent (~340 mA/cm^2) which is still much smaller than the current density from simultaneously applied electrical

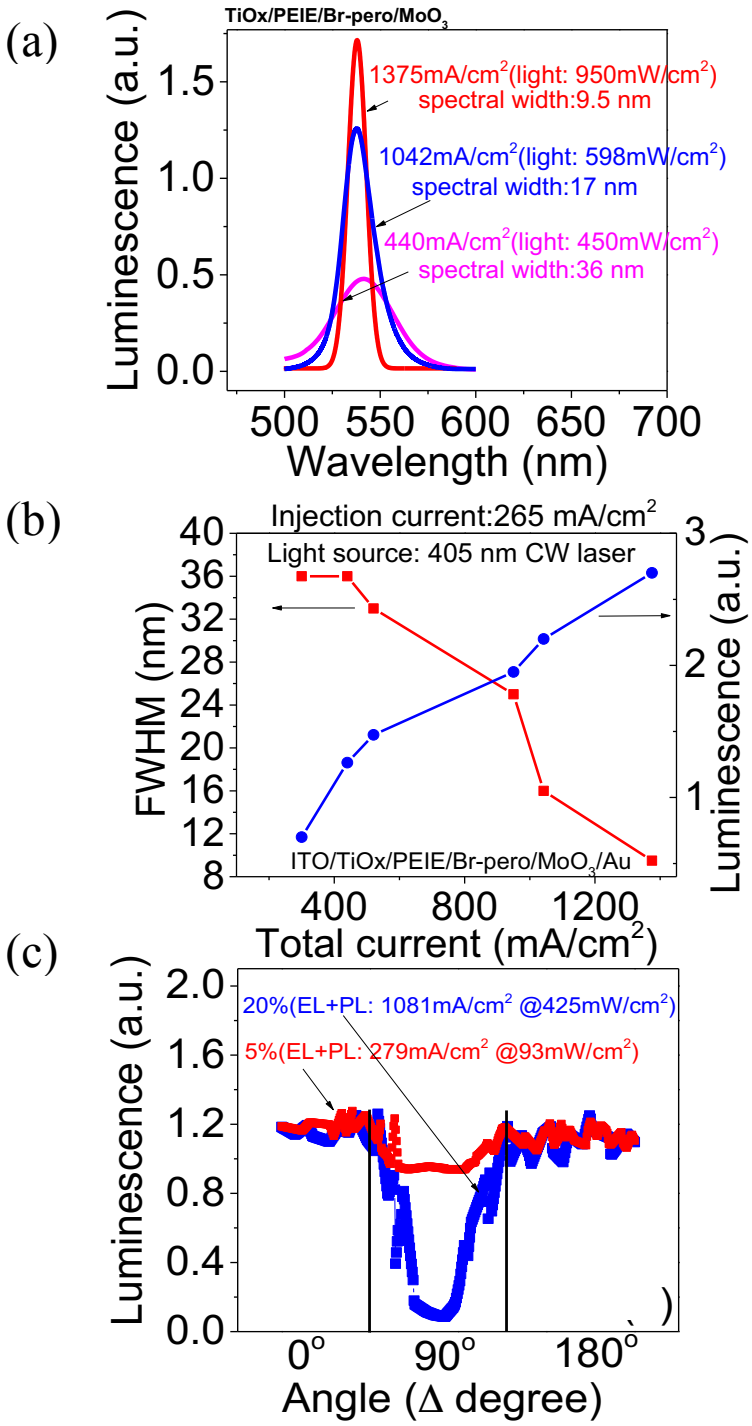

Figure 6-2. (a) Curve narrowing phenomenon from the bromine perovskite LED under dual excitations. (b) The relationship between FWHM and excitation intensity. (c) The detection of the linearly electrical polarization from emission light of bromine perovskite LEDs.

injection and photoexcitation. On the other hand, Figure 6-3 (b) shows the change of luminescence magnitudes as a function of excitation intensity under electrical excitation, photoexcitation, and the simultaneously applied electrical excitation and photoexcitation, respectively. It is worthy to note that under high excitation intensities the luminescence of PL+EL shows a higher magnitude than the sum-up of single PL and single EL. Similar to current amplification phenomenon, this result indicates that the simultaneously applied electrical excitation and photoexcitation can also provide a pathway to produce higher quantum yield of light emission in $CH_3NH_3PbBr_3$ samples. Clearly, these experimental results indicate that the excited states amplification phenomenon can be demonstrated under the simultaneously applied electrical injection and photoexcitation. As discussed, the high density of excited states is a crucial prerequisite to generate luminescence spectrum narrowing phenomenon. As a consequence, here the excited states amplification phenomenon generated from the simultaneously applied electrical excitation and photoexcitation could provide an important channel to generate high density of excited states, leading to satisfy the prerequisite for generating the luminescence spectrum narrowing phenomenon.

Now, we measure the single EL and single PL with a high intensity of electrical excitation and photoexcitation, respectively. Figure 6-4 (a) shows that luminescence spectrum of respective single EL and single PL exhibits no luminescence spectrum narrowing phenomenon even under a high intensity of electrical excitation or photoexcitation. In contrast to the single EL and single PL spectra, it could be seen clearly in Figure 6-4 (a) that the luminescence spectrum from simultaneously applied electrical excitation and photoexcitation (EL+PL) shows a detectable luminescence spectrum narrowing phenomenon with a similar magnitude of luminescence intensity as compared to single EL and single PL. Based on the experimental results, here we propose the second prerequisite, in addition to high density of excited state, for generating luminescence spectrum narrowing phenomenon: excited states induced alignment of electrical bulk-polarizations in $CH_3NH_3PbBr_3$ poly-crystals. In order to clarify the effect from the polarization of photoexcitation, here we apply a linear polarized photoexcitation and circular polarized photoexcitation into the $CH_3NH_3PbBr_3$ samples, in which the linearly polarized 405 nm

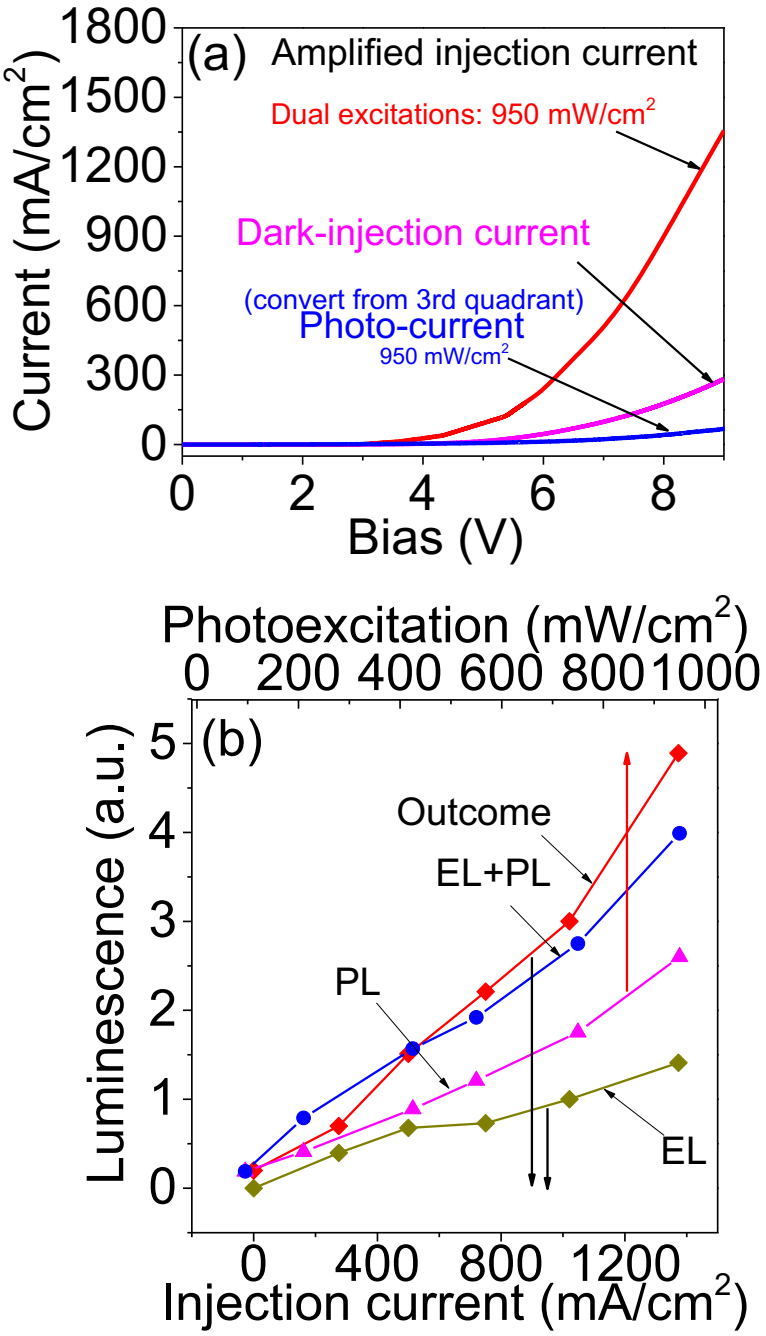

Figure 6-3. (a) Current density-voltage (*J-V*) curves measured from respective simultaneously applied electrical excitation and photoexcitation, solely electrical excitation, and photocurrent. (b) Luminescence intensity as a function of excitation inteisity under different types of excitation source.

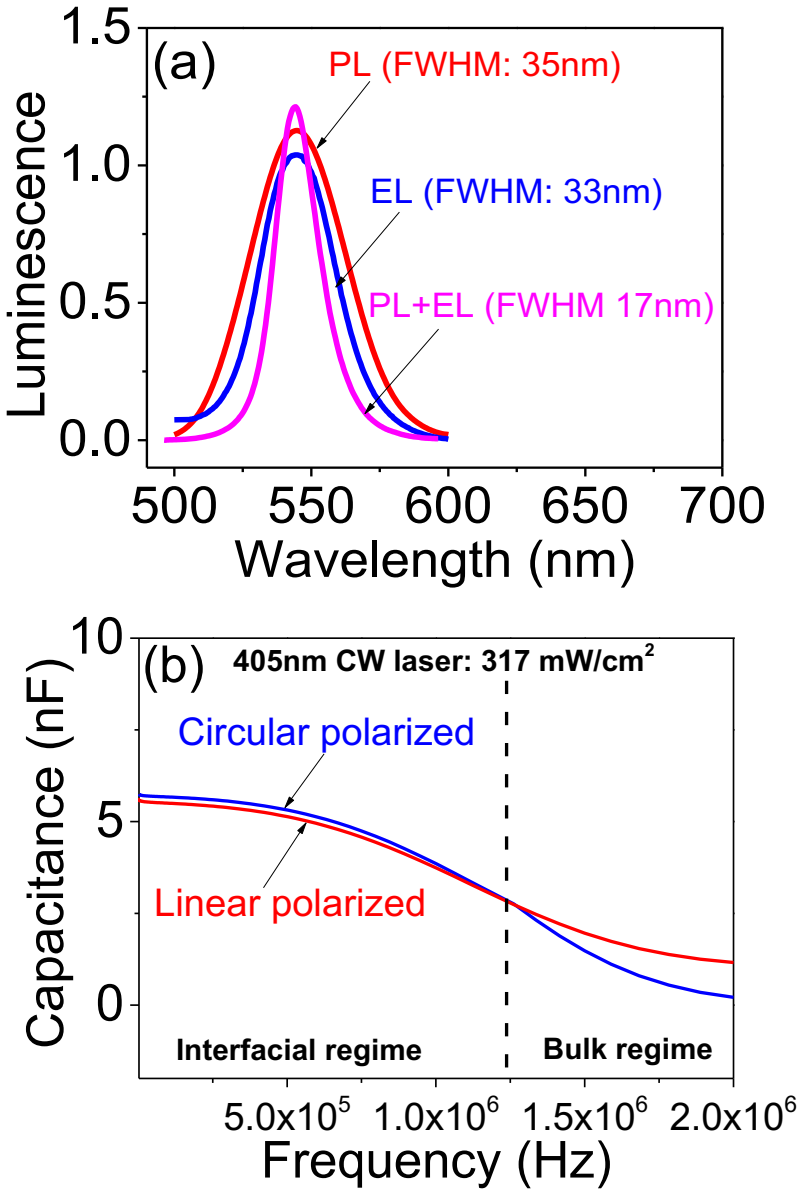

Figure 6-4. (a) Spectral comparison between photoluminescence, electroluminescence, and luminescence generated by simultaneously applied electrical excitation and photoexcitation. (b) *C-f* measurement under circularly polarized photoexcitation and linearly polarized photoexcitation.

laser beam with 2 mm dimeter was combined with a ¼ wave plate to generate switchable linearly and circularly polarized photoexcitations with identical intensity when the ¼ wave plate was rotated with 0° and 45° relative to the polarization direction of linearly polarized laser beam. Figure 6-4 (b) shows that the linear polarized photoexcitation can generate higher magnitude of polarization in high frequency regime than the circular polarized light in capacitance-frequency (*C-f*) measurement. Previous study has shown that the high frequency regime in the *C-f* measurement can be used to reflect the electrical bulk-polarization in organo-metal halide perovskite (OMHP) poly-crystals, and on the other hand, the low-frequency regime is corresponding to the interfacial polarization (interfacial charge accumulation) regime. Previous study has shown that the fluorescence polarization induced by polarized photoexcitation could be described by a relationship between excitation probability $P_{k'k}(t)$ and polarization direction of photoexcitation:

$$P_{k'k}(t) = \frac{\pi t}{4^{\ 2}} \left| \mu \ E \right|^2 \delta(\omega_{k'k} - \omega) \propto \left| \mu \ E \right|^2 = \mu^2 E^2 \cos^2 \theta \qquad (1)$$

where μ is the electrical dipole moment within light absorber, E is the electric field vector of photoexcitation, and θ is the angle between the polarization direction of photoexcitation and bulk-polarization direction of the light absorber domain. According to the equation (1), the polarized photoexcitation can induce a bulk-polarization in the domain of light absorber with a certain polarization direction. As a result, we can make an argument that the linear polarized photoexciation can induce a higher magnitude of electrical bulk-polarization within $CH_3NH_3PbBr_3$ poly-crystals than the situation of illuminating under circular polarized photoexcitation. At the mean time, we can see in low frequency regime (interfacial regime) that the circular polarized photoexcitation can lead to a higher magnitude of interfacial charge accumulation than the device under the illumination of linearly polarized photoexcitation. This result clearly indicates that the linearly polarized light illumination can reduce the free charge accumulation at the interface between perovskite poly-crystals and electrode due to an existence of aligned electrical dipole induced by linear polarized photoexcitation. Here, the *C-f* measurement has shown that the excited states amplification phenomenon could be attributed to the strong electrical bulk-polarization induced by linear polarized photoexcitation in $CH_3NH_3PbBr_3$ poly-crystals.

Under the existence of strong electrical bulk-polarization that the injected free charge carriers would experience a strong confinement filed in crystals domain of $CH_3NH_3PbBr_3$ poly-crystals, and therefore, leading to a significant free charge recombination.

Now, we verify the effect of electrical bulk-polarization in $CH_3NH_3PbBr_3$ poly-crystals on luminescence narrowing phenomenon. Here, we have directly measured the PL spectra under different magnitudes of external electrical field. The purpose of external electrical field is to provide a driving force to induce the electrical bulk-polarization in $CH_3NH_3PbBr_3$ poly-crystals. For excluding the effect from injected free charge carriers that the $CH_3NH_3PbBr_3$ layer is sandwiched by two insulating PMMA layers. Figure 6-5 (a) demonstrates the results of luminescence spectrum narrowing phenomenon of PL. It could be seen that the PL spectrum with a 35 V external electrical bias shows a narrower luminescence spectrum (20 nm) than that of the PL spectra under the external electrical biases of 5 V (31 nm) and 15 V (27 nm), respectively. Analogously, this PL spectrum narrowing phenomenon is similar to the luminescence spectrum narrowing phenomenon demonstrated in Figure 6-2 (a), which confirms that the mechanism of current amplification and enhanced light emission quantum yield effects are originated from the external field induced strong electrical bulk-polarization in $CH_3NH_3PbBr_3$ poly-crystals. On the other hand, it could be observed in Figure 6-5 (b) that the PL under a 35 V external electrical field shows a magnitude change of about 10.4% when we rotate the linear polarizer behind the $CH_3NH_3PbBr_3$ samples, which is higher than the measurements under the external electrical fields of respective 5 V (2.1%) and 15 V (2.2%). It is worthy to note that the trend of experimental result shown in Figure 6-5 (b) is also similar to Figure 6-2 (c) which is under the simultaneously applied electrical excitation and photoexcitation. These results suggest that under a presence of strong directionally external field, the emissive light of $CH_3NH_3PbBr_3$ samples can be more linearly polarized. Here, the linearly polarized emissive light from $CH_3NH_3PbBr_3$ samples could be attributed to a strong coherent interaction between field induced electrical bulk-polarization and excited states in $CH_3NH_3PbBr_3$ poly-crystals. In general, the light emission in semiconductors at room temperature is usually an in-homogeneous processes from different energy levels due to the presence of shallow trap states and phonon effect in semiconductors, which usually

leads to a broad FWHM in luminescence spectrum. However, we have found that with a strong electrical bulk-polarization in OMHP poly-crystals induced by an external field, the recombination processes could be transferred from in-homogeneous recombination to homogeneous recombination due to the strong coherent interaction between electrical bulk-polarization and excited states. Under this situation, the recombination of charge carriers could be confined within few specific energy levels. As a result, this homogeneous recombination processes can provide a pathway for a significant single band to band recombination, and leading to a purer color of light emission (luminescence spectrum narrowing phenomenon). Here, our study in the coherent interaction between electrical bulk-polarization and excited states in OMHP poly-crystals provides a deep understanding in the mechanism of homogeneous charge recombination processes, leading to benefit the development of electrical pumping laser by using OMHPs.

6.4 Conclusion

In this chapter, we have investigated the luminescence spectral narrowing phenomenon by introducing a simultaneously applied electrical excitation and photoexcitation. Here, it has been found that the optically induced amplification and alignment of electrically generated light-emitting excitons generate a co-operative interaction between light-emitting excitons, functioning as the underlying mechanism responsible for the spectral narrowing phenomenon with linear polarization characteristics in perovskite light-emitting diodes. The optically induced amplification of electrical generated light-emitting quantum yield is verified by the significant enhancement of electrical injection current caused by the linearly polarized incident light. Specifically, the injection current is increased from 340 mA/cm^2 to 1350 mA/cm^2 at the constant voltage mode (9 V) under the 405 nm CW laser beam of 950 mW/cm^2, leading to an optical amplification of injection current. The alignment of light-emitting excitons is confirmed by similar spectral narrowing phenomenon with linear polarization on photoluminescence (PL) induced by an external electrical field without electrical injection in the perovskite [$CH_3NH_3PbBr_3$] film. In particular, the PL spectral width is decreased from 31 nm to 20 nm with linear polarization characteristics when an external electrical field is applied on the perovskite [$CH_3NH_3PbBr_3$] without injecting electrical current. As a result, optically

induced amplification and alignment of electrically generated light-emitting excitons presents as an important methodology to develop co-operative interaction in EL actions in perovskite light-emitting didoes.

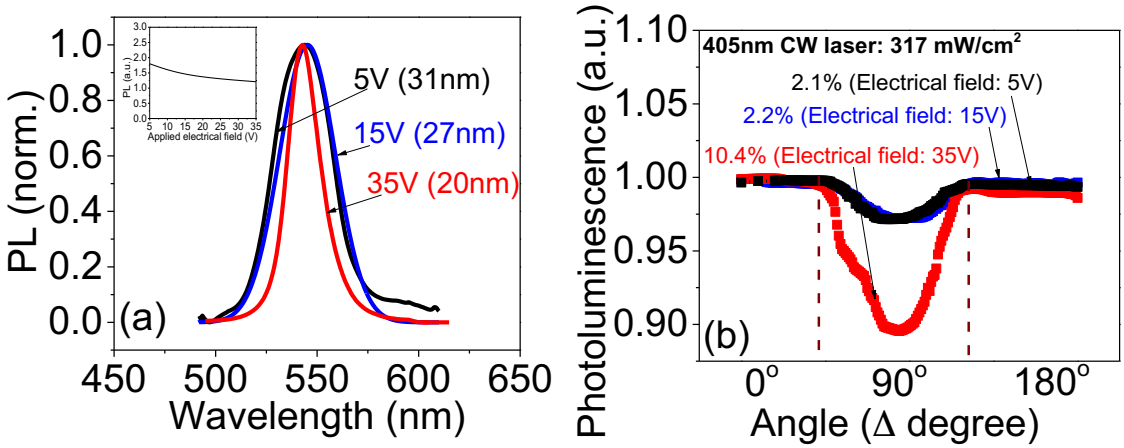

Figure 6-5. (a) Photoluminescence spectra narrowing phenomenon under different magnitudes of external electrical field without any injection current. (b) the detection of the linearly polarized photoluminescence under different magnitudes of external electrical field.

Chapter 7 Conclusion

The magnetic, optical, and electrical properties of the e-h pairs in polymer and organo-metal halide perovskite materials have been studies in this research. The overall research can be separated into three primary parts.

First, the e-h pairs within OMHP materials show a spin-dependent recombination/dissociation processes. We have found that the interaction between e-h pairs can cause a modulation of spin-exchange energy, leading to a different charge recombination and dissociation rates under different photoexcitation intensities. Furthermore, the e-h binding energy in OPV/OMHP solar cells can be estimate under device operating condition by using magneto-electrical measurement. We found that the intra-molecular dipole within polymer chain (PTB7) can provide an extra driving force, in addition to the built-in field, to benefit the charge dissociation, leading to a lower interfacial charge dissociation and lower e-h binding energy. As a result, the device efficiency with PTB7 as interfacial layer or active layer shows a higher device performance than the device using P3HT (without intra-molecular dipole) as interfacial layer or active layer. This concept provides a new direction for the device fabricator and material synthesizer to make higher efficiency photovoltaic devices and materials.

Second, the charge recombination mechanism within OMHP poly-crystals could be separated into two regimes: monomolecular recombination (trap assisted recombination) and bimolecular recombination. The monomolecular recombination occurs under low excitation intensity, which is due to the presence of shallow trap states. Under this situation, the trap assisted recombination will show a low efficiency of luminescence from OMHP thin film. However, under high excitation intensity that most of the shallow trap states are filled, and therefore, the recombination mechanism could be transferred from monomolecular recombination into bimolecular recombination. Under the situation of bimolecular recombination, the free mobile electrons and free mobile holes can undergo a strong recombination, leading to a higher luminescence efficiency. Moreover, we found that the monomolecular recombination regime shows an undetectable MFE response, which is contrast to the bimolecular regime. This result indicates that the spin-exchange

interaction under monomolecular recombination process is really strong, which is due to the short distance capture e-h pairs from shallow trap states. Nevertheless, the bimolecular recombined e-h pairs can show a detectable MFE response, which is due to the long distance capture radius for e-h pairs that can show lower spin-exchange interaction.

Third, the polarization enhanced e-h pairs interaction has been introduced. We found that a luminescence spectral narrowing phenomenon happens under a simultaneously applied electrical excitation and photoexcitation. Here, the purpose of two excitation sources is to provide sufficient population of excited states within OMHP active layer, and on the other hand, the linear polarized CW laser can induce a strong electrical polarization within OMHP poly-crystals. Under a strong electrical polarization in OMHP poly-crystals that a strong coherent interaction between photoexcited electron-hole pairs could be happened. Under this strong coherent interaction between electron-hole pairs that the charge recombination would be confined in specific energy levels, lead to a purer light emission (spectral narrowing phenomenon) than scenario of in-homogeneous recombination. This result has revealed the role of polarization effect on the recombination of light emitting action in OMHP light emitting diodes, leading to benefit the development of electrical pumping laser by using OMHPs.

.

List of Reference

1. D. M. Chapin, C. S. Fuller, and G. L. Pearson. *Journal of Applied Physics*, 1954, **25**, 676–677.
2. National Center For Photovoltaics. “Best Research-Cell Efficiencies.” 08 Jun. 2015.
3. W Shockley and H. J. Queisser. *Journal of Applied Physics*, 1961, **32**, 510.
4. T. A. Skotheim, J. Reynolds, Conjugated Polymers: Processing and Applications, CRC Press, **2007**.
5. N. S. Sariciftci, L. Smilowitz, A. J. Heeger, F. Wudl, *Science,* 1992, **258**, 1474.
6. B. Kraabel, C. H. Lee, D. McBranch, D. Moses, N. S. Sariciftci, A. J. Heeger, *Chem. Phys. Lett.* 1993, **213**, 389.
7. H. Zhou, Q. Chen, G. Li, S. Luo, T. b. Song, H. S. Duan, Z. Hong, J. You, Y. Liu and Y. Yang, *Science*, 2014, **345**, 542.
8. N. J. Jeon, J. H. Noh, Y. C. Kim, W. S. Yang, S. Ryu and S. I. Seok, *Nature materials*, 2014, **13**, 897.
9. Z. Xiao, C. Bi, Y. Shao, Q. Dong, Q. Wang, Y. Yuan, C. Wang, Y. Gao and J. Huang, *Energy & Environmental Science*, 2014, **7**, 2619.
10. J. Seo, S. Park, Y. Chan Kim, N. J. Jeon, J. H. Noh, S. C. Yoon and S. I. Seok, *Energy & Environmental Science*, 2014, **7**, 2642.
11. J. You, Y. Yang, Z. Hong, T.-B. Song, L. Meng, Y. Liu, C. Jiang, H. Zhou, W.-H. Chang, G. Li and Y. Yang, *Applied Physics Letters*, 2014, **105**, 183902.
12. G. E. Eperon, S. D. Stranks, C. Menelaou, M. B. Johnston, L. M. Herz and H. J. Snaith, *Energy & Environmental Science*, 2014, **7**, 982.
13. T. M. Koh, K. Fu, Y. Fang, S. Chen, T. C. Sum, N. Mathews, S. G. Mhaisalkar, P. P. Boix and T. Baikie, *The Journal of Physical Chemistry C*, 2014, **118**, 16458.
14. N. Pellet, P. Gao, G. Gregori, T. Y. Yang, M. K. Nazeeruddin, J. Maier and M. Gratzel, *Angewandte Chemie*, 2014, **53**, 3151.
15. Z. K. Tan, R. S. Moghaddam, M. L. Lai, P. Docampo, R. Higler, F. Deschler, M. Price, A. Sadhanala, L. M. Pazos, D. Credgington, F. Hanusch, T. Bein, H. J. Snaith and R. H. Friend, *Nature nanotechnology*, 2014, **9**, 687

16. Y. H. Kim, H. Cho, J. H. Heo, T. S. Kim, N. Myoung, C. L. Lee, S. H. Im and T. W. Lee, *Advanced materials*, 2014, **27**, 1248.
17. D. Di, K. P. Musselman, G. Li, A. Sadhanala, Y. Ievskaya, Q. Song, Z.-K. Tan, M. L. Lai, J. L. MacManus-Driscoll, N. C. Greenham and R. H. Friend, *The Journal of Physical Chemistry Letters*, 2015, **6**, 446.
18. R. L. Hoye, M. R. Chua, K. P. Musselman, G. Li, M. L. Lai, Z. K. Tan, N. C. Greenham, J. L. MacManus-Driscoll, R. H. Friend and D. Credgington, *Advanced materials*, 2015, **27**, 1414.
19. F. Deschler, M. Price, S. Pathak, L. E. Klintberg, D.-D. Jarausch, R. Higler, S. Hüttner, T. Leijtens, S. D. Stranks, H. J. Snaith, M. Atatüre, R. T. Phillips and R. H. Friend, *The Journal of Physical Chemistry Letters*, 2014, **5**, 1421.
20. G. Xing, N. Mathews, S. S. Lim, N. Yantara, X. Liu, D. Sabba, M. Gratzel, S. Mhaisalkar and T. C. Sum, *Nature materials*, 2014, **13**, 476.
21. Q. Zhang, S. T. Ha, X. Liu, T. C. Sum and Q. Xiong, *Nano letters*, 2014, **14**, 5995.
22. D. Giovanni, H. Ma, J. Chua, M. Grätzel, R. Ramesh, S. Mhaisalkar, N. Mathews and T. C. Sum, *Nano letters*, 2015, **15**, 1553.
23. K. Liang, D. B. Mitzi and M. T. Prikas, *Chemistry of Materials*, 1998, **10**, 403.
24. C. C. Stoumpos, C. D. Malliakas and M. G. Kanatzidis, *Inorg Chem*, 2013, **52**, 9019.
25. F. Hao, C. C. Stoumpos, D. H. Cao, R. P. H. Chang and M. G. Kanatzidis, *Nature Photonics*, 2014, **8**, 489.
26. N. K. Noel, S. D. Stranks, A. Abate, C. Wehrenfennig, S. Guarnera, A. A. Haghighirad, A. Sadhanala, G. E. Eperon, S. K. Pathak, M. B. Johnston, A. Petrozza, L. M. Herz and H. J. Snaith, *Energy & Environmental Science*, 2014, **7**, 3061.
27. Y. Ogomi, A. Morita, S. Tsukamoto, T. Saitho, N. Fujikawa, Q. Shen, T. Toyoda, K. Yoshino, S. S. Pandey, T. Ma and S. Hayase, *The Journal of Physical Chemistry Letters*, 2014, **5**, 1004.
28. F. Zuo, S. T. Williams, P. W. Liang, C. C. Chueh, C. Y. Liao and A. K. Jen, *Advanced materials*, 2014, **26**, 6454.
29. A. Kojima, K. Teshima, Y. Shirai and T. Miyasaka, *Journal of the American Chemical Society*, 2009, **131**, 6050.

30. J.-H. Im, C.-R. Lee, J.-W. Lee, S.-W. Park and N.-G. Park, *Nanoscale*, 2011, **3**, 4088.
31. M. M. Lee, J. Teuscher, T. Miyasaka, T. N. Murakami and H. J. Snaith, *Science*, 2012, **338**, 643.
32. M. A. Green, K. Emery, Y. Hishikawa, W. Warta and E. D. Dunlop, *Progress in Photovoltaics: Research and Applications*, 2015, **23**, 1.
33. J. H. Heo, S. H. Im, J. H. Noh, T. N. Mandal, C.-S. Lim, J. A. Chang, Y. H. Lee, H.-j. Kim, A. Sarkar, M. K. Nazeeruddin, M. Grätzel and S. I. Seok, *Nature Photonics*, 2013, **7**, 486.
34. M. Hu, C. Bi, Y. Yuan, Z. Xiao, Q. Dong, Y. Shao and J. Huang, *Small*, 2015, **11**, 2164.
35. E. J. Juarez-Perez, R. S. Sanchez, L. Badia, G. Garcia-Belmonte, Y. S. Kang, I. Mora-Sero and J. Bisquert, *The Journal of Physical Chemistry Letters*, 2014, **5**, 2390.
36. M. Hirasawa, T. Ishihara, T. Goto, K. Uchida and N. Miura, *Physica B: Condensed Matter*, 1994, **201**, 427-430.
37. W. Zhang, M. Saliba, S. D. Stranks, Y. Sun, X. Shi, U. Wiesner and H. J. Snaith, *Nano letters*, 2013, **13**, 4505.
38. J. M. Frost, K. T. Butler, F. Brivio, C. H. Hendon, M. van Schilfgaarde and A. Walsh, *Nano letters*, 2014, **14**, 2584.
39. J. M. Frost, K. T. Butler and A. Walsh, *Apl Materials*, 2014, **2**, 081506.
40 C. Zhang, D. Sun, C.-X. Sheng, Y. X. Zhai and Z. V. Vardeny, *Nat. Phys.*, 2015, **11**, 427-434.
41. Y.-C. Hsiao, T. Wu, M. Li and B. Hu, *Advanced Materials*, 2015, **27**, 2899-2906.
42. S. D. Stranks, G. E. Eperon, G. Grancini, C. Menelaou, M. J. Alcocer, T. Leijtens, L. M. Herz, A. Petrozza and H. J. Snaith, *Science*, 2013, **342**, 341.
43. G. Xing, N. Mathews, S. Sun, S. S. Lim, Y. M. Lam, M. Grätzel, S. Mhaisalkar and T. C. Sum, *Science*, 2013, **342**, 344.
44. Q. Lin, A. Armin, R. C. R. Nagiri, P. L. Burn and P. Meredith, *Nat Photon*, 2015, **9**, 106.

45. O. Noblanc, P. Gaucher and G. Calvarin, *Journal of Applied Physics*, 1996, **79**, 4291.
46. S. Liu, F. Zheng, N. Z. Koocher, H. Takenaka, F. Wang and A. M. Rappe, *The Journal of Physical Chemistry Letters,* 2015, **6**, 693.
47. G. Walters, B. R. Sutherland, S. Hoogland, D. Shi, R. Comin, D. P. Sellan, O. M. Bakr, E. H. Sargent, *ACS nano* 2015, **9**, 9340.
48. M. Antonietta Loi, J. C. Hummelen, *Nature materials* 2013, **12,** 1087.
49. M. A. Baldo, S. Lamansky, P. E. Burrows, M. E. Thompson, S. R. Forrest, *Appl. Phys. Lett*, 1999, **75**, 4.
50. M. A. Baldo, S. R. Forrest, *Phys. Rev. B* 2000, **62**, 10958.
51. E. L. Frankevich, A. A. Lymarev, I. Sokolik, F. E. Karasz, S. Blumstengel, R. H. Baughman, H. H. Hörhold, *Phys. Rev. B*, **46**, 9320 (1992).
52. Yu. V. Romanovskii, A. Gerhard, B. Schweitzer, U. Scherf, R. I. Personov, H. Bässler, *Phys. Rev. Lett*. 2000, **84**, 1027.
53. A. P. Monkman, H. D. Burrows, L. J. Hartwell, L. E. Horsburgh, I. Hamblett, S. Navaratnam, *Phys. Rev. Lett*. **86**, 2001, 1358.
54. E. L. Frankevich, A. A. Lymarev, I. Sokolik, F. E. Karasz, S. Blumstengel, R. H. Baughman, H. H. Hörhold, *Phys. Rev. B*, 1992, **46**, 9320.
55. H. Ohkita, S. Cook, Y. Astuti, W. Duffy, S. Tierney, W. Zhang, M. Heeney, I. McCulloch, J. Nelson, D. D. C. Bradley, J. R. Durrant, *J. Am. Chem. Soc*. 2008, **130**, 3030.
56. V. Dyakonov and E. Frankevich, *Chemical Physics*, 1998, **227**, 203–217.
57. H. Zang (2012), Magnetic, Optical and Dielectric E ects on Photovoltaic Processes in Organic Solar Cells (Doctoral dissertation). Retrieved from http://trace.tennessee.edu/utk_graddiss/1436.
58. Y. Liang, Z. Xu, J. Xia, S. T. Tsai, Y. Wu, G. Li, C. Ray, L. Yu, *Adv. Mater*. 2010, **22**, E135.
59. S. J. Lou, J. M. Szarko, T. Xu, L. Yu, T. J. Marks, L. X. Chen, *J. Am. Chem. Soc*. 2011, **133**, 20661.
60. G. Li, V. Shrotriya, Y. Yao, J. Huang, Y. Yang, *J. Mater. Chem.* 2007, **17**, 3126.

61. Z. He, C. Zhong, S. Su, M. Xu, H. Wu, Y. Cao, *Nat Photon*. 2012, **6**, 591.
62. L. Dou, J. You, J. Yang, C.-C. Chen, Y. He, S. Murase, T. Moriarty, K. Emery, G. Li, Y. Yang, *Nat Photon*. 2012, **6**, 180.
63. Y. Zhong, M. T. Trinh, R. Chen, W. Wang, P. P. Khlyabich, B. Kumar, Q. Xu, C.-Y. Nam, M. Y. Sfeir, C. Black, *J. Am. Chem. Soc*. 2014, **136**, 15215.
64. J.-M. Jiang, M.-C. Yuan, K. Dinakaran, A. Hariharan, K.-H. Wei, *J. Mater. Chem. A* 2013, **1,** 4415.
65. S. C. Price, A. C. Stuart, L. Yang, H. Zhou, W. You, *J. Am. Chem. Soc*. 2011, **133**, 4625.
66. X. Zhang, T. T. Steckler, R. R. Dasari, S. Ohira, W. J. Potscavage, S. P. Tiwari, S. Coppee, S. Ellinger, S. Barlow, J.-L. Bredas, B. Kippelen, J. R. Reynolds, S. R. Marder, *J. Mater. Chem*. 2010, **20**, 123.
67. M. Wang, X. Hu, P. Liu, W. Li, X. Gong, F. Huang, Y. Cao, *J. Am. Chem. Soc*. 2011, **133**, 9638.
68. H. Zhou, L. Yang, W. You, *Macromolecules* 2012, **45**, 607.
69. H. Zang, Y. Liang, L. Yu, B. Hu, *Adv. Energy Mater*. 2011, **1**, 923.
70. B. Carsten, J. M. Szarko, H. J. Son, W. Wang, L. Lu, F. He, B. S. Rolczynski, S. J. Lou, L. X. Chen, L. Yu, *J. Am. Chem. Soc*. 2011, **133**, 20468.
71. T. Xu, L. Lu, T. Zheng, J. M. Szarko, A. Schneider, L. X. Chen and L. Yu, *Adv. Funct. Mate*r. 2014, **24**, 3432.
72. B. S. Rolczynski, J. M. Szarko, H. J. Son, L. Yu, L. X. Chen, *J. Phys. Chem. Lett*. 2014, **5**, 1856.
73. B. Carsten, J. M. Szarko, L. Lu, H. J. Son, F. He, Y. Y. Botros, L. X. Chen, L. Yu, *Macromolecules* 2012, **45**, 6390.
74. B. S. Rolczynski, J. M. Szarko, H. J. Son, Y. Liang, L. Yu, L. X. Chen, *J. Am. Chem. Soc*. 2012, **134**, 4142.
75. D. S. Sabirov, *RSC Adv*. 2014, **4**, 44996.
76. K. Akhtari, K. Hassanzadeh, B. Fakhraei, H. Hassanzadeh, G. Akhtari, S. A. Zarei, *Computational and Theoretical Chemistry* 2014, **1038**, 1.

77. K. Akaike, K. Kanai, H. Yoshida, J. y. Tsutsumi, T. Nishi, N. Sato, Y. Ouchi, K. Seki, *J. Appl. Phys*. 2008, **104**, 023710.
78. B. Brocklehurst, R. Dixon, E. Gardy, V. Lopata, M. Quinn, A. Singh, F. Sargent, *Chem. Phys. Lett*. 1974, **28**, 361.
79. K. Schulten, H. Staerk, A. Weller, H.-J. Werner, B. Nickel, *Zeitschrift für Physikalische Chemie* 1976, **101**, 371.
80. K. Okamoto, N. Oda, A. Itaya, S. Kusabayashi, *Chem. Phys. Lett*. 1975, **35**, 483.
81. Z. H. Xu, B. Hu, *Adv. Funct. Mater*. 2008, **18**, 2611.
82. Y. Zhang, T. P. Basel, B. R. Gautam, X. Yang, D. J. Mascaro, F. Liu, Z. V. Vardeny, *Nat. commun*. 2012, **3**, 1043.
83. B. Hu, L. Yan, M. Shao, *Adv. Mater*. 2009, **21**, 1500.
84. F. Wang, H. Bässler, Z. V. Vardeny, *Phys. Rev. Lett*. 2008, **101**, 236805.
85. L. He, M. Li, A. Urbas, B. Hu, *Phys. Rev. B* 2014, **89**, 155304.
86. A. Schellekens, W. Wagemans, S. Kersten, P. Bobbert, B. Koopmans, *Phys. Rev. B* 2011, **84**, 075204.
87. W. Wagemans, W. Engelen, F. Bloom, B. Koopmans, *Synt. Met*. 2010, **160**, 266.
88. Y. Kim, S. A. Choulis, J. Nelson, D. D. C. Bradley, S. Cook, J. R. Durrant, *J. Mater. Sci*. 2005, **40**, 1371.
89. Y. Kim, S. Cook, S. M. Tuladhar, S. A. Choulis, J. Nelson, J. R. Durrant, D. D. C. Bradley, M. Giles, I. McCulloch, C.-S. Ha, M. Ree, *Nat. Mater*. 2006, **5**, 197.
90. S. De, T. Pascher, M. Maiti, K. G. Jespersen, T. Kesti, F. Zhang, O. Inganäs, A. Yartsev, V. Sundström, *J. Am. Chem. Soc.* 2007, **129**, 8466.
91. R. C. I. MacKenzie, T. Kirchartz, G. F. A. Dibb, J. Nelson, *J. Phys. Chem. C* 2011, **115**, 9806.
92. M. Clarke, A. M. Ballantyne, J. Nelson, D. D. C. Bradley, J. R. Durrant, *Adv. Funct. Mater.* 2008, **18**, 4029.
93. C. Zhao, B. Chen, X. Qiao, L. Luan, K. Lu, B. Hu, *Adv. Energy Mater* 2015,. **5**, doi:10.1002/aenm.20157007.
94. S. Foster, F. Deledalle, A. Mitani, T. Kimura, K.-B. Kim, T. Okachi, T. Kirchartz, J.

Oguma, K. Miyake, J. R. Durrant, S. Doi, J. Nelson,*Adv. Energy Mater.* 2014, **4**, 1400311.

95. L. Lu, T. Xu, W. Chen, J. M. Lee, Z. Luo, I. H. Jung, H. I. Park, S. O. Kim, L. Yu, *Nano lett.* 2013, **13**, 2365.
96. H. Zang, Z. Xu, B. Hu, *J. Phys. Chem. B* 2010, **114**, 5704.
97. T. Leijtens, S. D. Stranks, G. E. Eperon, R. Lindblad, E. M. J. Johansson, I. J. McPherson, H. Rensmo, J. M. Ball, M. M. Lee, H. J. Snaith, *ACS Nano* 2014, **8**, 7147.
98. A. Abate, M. Saliba, D. J. Hollman, S. D. Stranks, K. Wojciechowski, R. Avolio, G. Grancini, A. Petrozza, H. J. Snaith, *Nano lett.*. 2014, **14**, 3247.
99. H.-S. Kim, I. Mora-Sero, V. Gonzalez-Pedro, F. Fabregat-Santiago, E. J. Juarez-Perez, N.-G. Park, J. Bisquert, *Nat. Commun.* 2013, **4**, 2242.
100. V. Roiati, E. Mosconi, A. Listorti, S. Colella, G. Gigli, F. De Angelis, *Nano lett.* 2014, **14**, 2168.
101. P. Schulz, E. Edri, S. Kirmayer, G. Hodes, D. Cahen, A. Kahn, *Energy Environ. Sci.* 2014, **7**, 1377.
102. J. Szmytkowski, W. Stampor, J. Kalinowski, Z. H. Kafafi, *Appl. Phys. Lett.* 2002, **80**, 1465.
103. C. L. Braun, *J. Chem. Phys.*1984, **80**, 4157.
104. D. Veldman, Ö. İpek, S. C. J. Meskers, J. Sweelssen, M. M. Koetse, S. C. Veenstra, J. M. Kroon, S. S. v. Bavel, J. Loos, R. A. J. Janssen, *J. Am. Chem. Soc.* 2008, **130**, 7721.
105. V. D. Mihailetchi, L. J. A. Koster, J. C. Hummelen, P. W. M. Blom, *Phys. Rev. Lett*. 2004, **93**, 216601.
106. N. C. Miller, R. Gysel, C. E. Miller, E. Verploegen, Z. Beiley, M. Heeney, I. McCulloch, Z. Bao, M. F. Toney, M. D. McGehee, J. Polym. *Sci. B Polym. Phys.* 2013, **49**, 499.
107. T. M. Burke, M. D. McGehee, *Adv. Mater.* 2013, **26**, 1923.
108. A. Miyata, A. Mitioglu, P. Plochocka, O. Portugall, J. T.-W. Wang, S. D. Stranks, H. J. Snaith, R. J. Nicholas, *Nat. Physics* 2015, **11**, 582.

109. Y. Yamada, T. Nakamura, M. Endo, A. Wakamiya, Y. Kanemitsu, *J. Am. Chem. Soc.* 2014, **136**, 11610.
110. S. D. Stranks, V. M. Burlakov, T. Leijtens, J. M. Ball, A. Goriely, H. J. Snaith, *Phys. Rev. Applied,* 2014, **2**, 034007.
111. W. Tress, N. Marinova, O. Inganäs, M. K. Nazeeruddin, S. M. Zakeeruddin, M. Graetzel, *Adv. Energy Mater*. 2015, **5**.
112. A. N. Aleshin, S. R. Williams, A. J. Heeger, *Synth. Met*. 1998, **94**, 930.
113. T. D. Nguyen, Y. Sheng, M. Wohlgenannt, T. D. Anthopoulos, *Synth. Met*. 2007, **157**, 930.
114. C. S. S. Sangeeth, M. Jaiswal, R. Menon, *J. Phys.: Condens. Matter.* 2009*,* **21**, 072101.
115. T. D. Nguyen, Y. Sheng, J. Rybicki, G. Veeraraghavan, M. Wohlgenannt, *J. Mater. Chem*. 2007, **17**, 1995.
116. V. Prigodin, J. Bergeson, D. Lincoln and A. Epstein, *Synth. Met*. 2006, **156**, 757.
117. S. P. Kersten, A. J. Schellekens, B. Koopmans, P. A. Bobbert, *Phys. Rev. Lett.* 2011, **106**, 197402.
118. T. D. Nguyen, G. Hukic-Markosian, F. Wang, L. Wojcik, X.-G. Li, E. Ehrenfreund, Z. V. Vardeny, *Nat. Mater.* 2010, **9**, 345.
119. P.A. Bobbert, T. D. Nguyen, F. W. A. van Oost, B. Koopmans, M. Wohlgenannt, *Phys. Rev. Lett.* 2007, **99**, 216801.
120. L. He, M. Li, A. Urbas, B. Hu, *Adv. Mater.* 2014*,* **26**, 3956.
121. M. Li, H. Wang, L. He, H. Zang, H. Xu, B. Hu, *Appl. Phys. Lett*. 2014, **105**, 023302.
122. H. Zang, L. Yan, M. Li, L. He, Z. Gai, I. Ivanov, M. Wang, L. Chiang, A. Urbas, B. Hu, *Sci. Rep*. 2013*,* **3**, 2812.
123. B. R. Sutherland, A. K. Johnston, A. H. Ip, J. Xu, V. Adinolfi, P. Kanjanaboos, E. H. Sargent, *ACS Photonics* 2015, **2**, 1117.
124. H. P. Dong, Y. Li, S. F. Wang, W. Z. Li, N. Li, X. D. Guo, L. D. Wang, *J. Mater. Chem. A* 2015, **3**, 9999.
125. T. Wu, Y.-C. Hsiao, M. Li, N.-G. Kang, J. W. Mays, B. Hu, *J. Phys. Chem. C* 2015, **119**, 2727.

126. I. Grinberg, D. V. West, M. Torres, G. Gou, D. M. Stein, L. Wu, G. Chen, E. M. Gallo, A. R. Akbashev, P. K. Davies, J. E. Spanier, A. M. Rappe, *Nature* 2013, **503**, 509.
127. Z. He, B. Xiao, F. Liu, H. Wu, Y. Yang, S. Xiao, C. Wang, T. P. Russell, Y. Cao, *Nat. Photon*. 2015, **9**, 174.
128. B. Yang, O. Dyck, J. Poplawsky, J. Keum, A. Puretzky, S. Das, I. N. Ivanov, C. M. Rouleau, G. Duscher, D. B. Geohegan, K. Xiao, *J. Am. Chem. Soc.*2015, **137**, 9210.
129. Y.-C. Hsiao, H. Zang, I. Ivanov, T. Xu, L. Lu, L. Yu, B. Hu, *J. Appl. Phys*. 2014, **115**, 154506.
130. Y.-C. Hsiao, T. Wu, M. Li, Q. Liu, W. Qin, B. Hu, *J. Mater. Chem. A* 2015, **3**, 15372.
131. T. Hattori, T. Taira, M. Era, T. Tsutsui, S. Saito, *Chem. Phys. Lett.* 1996, **254**, 103.
132. K. Chondroudis, D. B. Mitzi, *Chem. Mater*. 1999, **11**, 3028.
133. Cheng, X. Dai, S. Bai, H. He, Z. Ye, M. L. Lai, R. H. Friend, W. Huang, *Adv. Mater.* 2015, **27**, 2311.
134. H. Cho, S.-H. Jeong, M.-H. Park, Y.-H. Kim, C. Wolf, C.-L. Lee, J. H. Heo, A. Sadhanala, N. Myoung, S. Yoo, S. H. Im, R. H. Friend, T.-W. Lee, *Science* 2015, **350**, 1222.
135. A. Sadhanala, A. Kumar, S. Pathak, A. Rao, U. Steiner, N. C. Greenham, H. J. Snaith, R. H. Friend, *Adv. Electro. Mater.* **1**, (2015).
136. T. Leijtens, A. R. Srimath Kandada, G. E. Eperon, G. Grancini, V. D'Innocenzo, J. M. Ball, S. D. Stranks, H. J. Snaith, A. Petrozza, *J. Am. Chem. Soc.* 2015, doi:10.1021/jacs.5b09085.
137. M. Saba, M. Cadelano, D. Marongiu, F. Chen, V. Sarritzu, N. Sestu, C. Figus, M. Aresti, R. Piras, A. Geddo Lehmann, C. Cannas, A. Musinu, F. Quochi, A. Mura, G. Bongiovanni, *Nat. commun.* 2014, **5**, 5049.
138. J. S. Manser, P. V. Kamat, *Nat. Photon.* 2014, **8**, 737.
139. X. Mettan, R. Pisoni, P. Matus, A. Pisoni, J. Jaćimović, B. Náfrádi, M. Spina, D. Pavuna, L. Forró, E. Horváth, *J. Phys. Chem. C* 2015, **119**, 11506.

140. F. Liu, M. R. Kelley, S. A. Crooker, W. Nie, A. D. Mohite, P. P. Ruden, D. L. Smith, *Phys. Rev. B* 2014, **90**, 235314.
141. S. A. Crooker, F. Liu, M. R. Kelley, N. J. D. Martinez, W. Nie, A. Mohite, I. H. Nayyar, S. Tretiak, D. L. Smith, P. P. Ruden, *Appl. Phys. Lett.* 2014, **105**, 153304.
142. K. Tanaka, T. Takahashi, T. Ban, T. Kondo, K. Uchida, N. Miura, *Solid State Commun*, 2003, **127**, 619.
143. B. Hu, Y.Wu, *Nat. Mater.* 2007, **6**, 985.
144. M. Feneberg, M. Fátima Romero, B. Neuschl, K. Thonke, M. Röppischer, C. Cobet, N. Esser, M. Bickermann, R. Goldhahn, *Appl. Phys. Lett.*2013, **102**, 052112.
145. M. Cox, S. P. Kersten, J. M. Veerhoek, P. Bobbert, B. Koopmans, *Phys. Rev. B* 2015, **91**, 165205.
146. Y. Yang, D. P. Ostrowski, R. M. France, K. Zhu, J. van de Lagemaat, J. M. Luther, M. C. Beard, *Nat. Photon*. 2015, **10**, 53.
138. H. Cho, S.-H. Jeong, M.-H. Park, Y.-H. Kim, C. Wolf, C.-L. Lee, J. H. Heo, A. Sadhanala, N. Myoung, S. Yoo, S. H. Im, R. H. Friend, T.-W. Lee, *Science* 2015, **350**, 1222.

VITA

Yu-Che Hsiao received his M.S. degree in electro-optical science and engineering in 2009 from National Cheng Kung University, Taiwan, and has been at the University of Tennessee since 2011. He conducts research on the device engineering of high efficiency solar cells and light emitting diodes by using polymer and organo-metal halide perovskite materials as active layer. He is also conducting research on the intrinsically electrical, magnetic, and optical properties in polymer and organo-metal halide perovskite materials under device operating condition.